Flow field modifications and wave development in a plane Poiseuille flow

by

Fei Li

B.Sc. Honours, The Victoria University of Manchester, (1983)
S.M., Massachusetts Institute of Technology, (1986)

Submitted to the Department of
Aeronautics and Astronautics
in partial fulfillment of the
requirements for the degree of

Doctor of Science

at the

Massachusetts Institute of Technology

June, 1991

Signature of Author _____
February 26, 1991

Certified by _____
Prof. Sheila E. Widnall
Thesis Supervisor

Certified by _____
Prof. Mårten T. Landahl
Thesis Committee Member

Certified by _____
Prof. Joseph H. Haritonidis
Thesis Committee Member

Accepted by _____
Prof. Harold Y. Wachman
Chairman, Department Graduate Committee

Flow field modifications and wave development in a plane Poiseuille flow

by

Fei Li

Submitted to the Department of
Aeronautics and Astronautics
in partial fulfillment of the
requirements of the Degree of

Doctor of Science

Abstract

Laminar-Turbulent Transition in a plane Poiseuille flow can occur at $Re \approx 1000$, with the appearance of turbulent spots. This Reynolds number is much lower than the critical Reynolds number for linear instability ($Re_{critcal} = 5772.22$). The turbulent spot in a plane Poiseuille flow is modelled as a region of increased Reynolds stress, which travels with a prescribed speed through the surrounding laminar flow. The Reynolds averaged Navier-Stokes equations are solved at subcritical Reynolds numbers by using a spectral method. The travelling Reynolds stress acts as a forcing term in the equations.

The modelled turbulent spot modifies the large scale velocity field in the surrounding laminar flow. There exit regions outside the turbulent spot with highly inflexional velocity profiles. The properties of these large scale perturbations can be related to the eigenmodes of the normal vorticity equation. Small scale wave perturbations can be introduced. These waves, then, grow in the areas destabilized by the large scale perturbations. The computational results agree well with existing experiment and numerical simulations.

Thesis Supervisor: Sheila E. Widnall

Title: Abby Rockefeller Mauze Professor of
Aeronautics and Astronautics

Acknowledgement

I would like to express my sincerest thanks to my research supervisor, Professor Sheila E. Widnall, for giving me the opportunity to work on this interesting problem under her guidance. Her support, advice and patience have been most invaluable and are greatly appreciated.

I would like to thank Professor Mårten T. Landahl for everything I have learned from him. Very helpful to me in my reseach were the bi-weekly group discussions organized by him, from which I learned how to learn.

I would like to thank Professor Joseph H. Haritonidis for his interest, help and advice in my research. His insistence on paying attention to details have been invaluable. His criticism have only made the present work better than it would have been otherwise.

I would like to thank Professor Dan S. Henningson for his expert help. Many discussions over the "turbulent lunch" have given me a lot of ideas concerning my research work. The contour plot routine I obtained from him has been a very helpful tool in presenting my results.

I would like to thank Professor Kenneth S. Breuer for carefully reading the present thesis and for very helpful discussions which range from grammar to technical details

of the present research.

I would like to thank Mr. Peter J. Schmid for providing me with the computer program which enabled me to accurately calculate the eigenvalues and eigenfunctions.

I would like to thank my fellow students and friends at M.I.T for sharing with me their knowledge and experiences in all aspects of life – Dr. Ponnampalam Balakumar, Dr. Norman Lee, Dr. Sean Tavares, Dr. Andrew Wo, Messrs. Sasi Digavalli, Pieter Grooth, Alex Gioulekus, Kevin Huh, Douglus Ling, Stephane Mondoloni and Jorgen Olsson.

I would like to thank my friends from China whose support, encouragement and friendship have made my life away from home much easier, especially at difficult times – Dr. & Mrs. Longqing Chen, Dr. & Mrs. Zhiyou Du, Dr. Kun Hsia & Dr. Qiong Huang (and of course, their infant son, Tim), Mr. & Mrs. Dawei Qi, Mr. Yuanjing Qiu, Dr. & Mrs. Jirong Xiao, Dr. Guozhong Xie and Dr. Changyuan Ye.

Finally, I would like to express my deepest appreciation half way around the world to my parents and my brother for their support, care and encouragement which made this all possible.

Contents

1 Introduction **16**

1.1 Two dimensional instability 17

1.2 Three-dimensional instabilities 20

1.3 Localized disturbances and turbulent spots 22

1.4 Motivation for the present study 28

1.5 Organization of this thesis 33

2 Formulation **35**

2.1 The geometry and the orientation of axis system 35

2.2 Governing equations 37

2.3 Modelling the Reynolds stress 39

2.3.1 Fully turbulent flow in a channel and the turbulent characteristics within a turbulent spot 39

2.3.2 Assumptions 40

2.3.3 Modelling the turbulence within a turbulent spot 41

2.4 Symmetry 44

3 Numerical Methods **45**

3.1 Chebyshev polynomial approximations 45

3.2 Fourier series approximations 47

3.3 Spectral representation of flow variables 48

3.4 The time splitting scheme 49

4 Modifications of the Flow Field **52**

4.1 General patterns of flow around the disturbance 52

4.2 Flow fields forced at different speeds 54

5 Origins of the modified flow field **68**

5.1 Eigenvalue problem of the normal vorticity equation 68

5.2 Eigenmodes contributing to flow field modifications 75

5.3 Energy in the spanwise modes 80

6 Linear Waves in Plane Poiseuille Flow **92**

6.1 Linear waves in unmodified flow field 92

6.2 Importance of oblique waves at subcritical Reynolds numbers 95

6.2.1 Eigenvalues of the Orr-Sommerfeld Equation at $Re = 1000$ . . . 95

6.2.2 Longitudinal linear perturbations 96

6.2.3 Perturbations of finite extent 102

6.2.4 More on 3-dimensionality at low Reynolds numbers 104

6.3 Linear waves in modified flow field 106

6.4 Wave growth at higher Reynolds numbers 110

7 Finite Amplitude Waves **128**

7.1 Finite amplitude waves in unmodified flow field 128

7.2 Finite amplitude waves in modified flow field 129

7.3 Breakdown of finite amplitude waves 134

8 Conclusions and Further Discussions **148**

8.1 Linear free waves in plane Poiseuille flow 148

8.2 Mean flow modifications 150

8.3 Growth of oblique waves riding on the large scale modifications to the mean flow 151

8.4 Advantages and disadvantages of using the modelled spot 153

A Approximations to the integrals **155**

List of Figures

1.1 Schematic diagram of the turbulent spot growth cycle 33

2.1 The geometry of the channel and the axis system 36

4.1 Contours u-perturbation velocity. $Re = 1000$, $c_s = 0.8$, $c_1 = 1 \times 10^{-5}$, $t = 10$. Contour values start from -5×10^{-6}, increment 2×10^{-6}. —— positive, - - - - negative. (a) $z = 0$ and (b) $z = 0.556$ 60

4.2 Contours of u-perturbation. $Re = 1000$, $c_s = 0.8$, $c_1 = 1 \times 10^{-5}$, $t = 30$. Contour values start from -5×10^{-6}, increment=2×10^{-6}. (a) $z = 0$ and (b) $z = 0.556$. 61

4.3 Contour u-perturbation velocity. $Re = 1000$, $c_s = 0.8$, $c_1 = 0.05$, and $t = 30$. Contour values start from -0.025, increment 0.01. —— positive, - - - - negative. (a)$z = 0$ and (b)$z = 0.556$. 62

4.4 Contours u-perturbation velocity.$Re = 1000$, $c_1 = 0.05$, $t = 45$. Contour values start from -0.025, increment 0.01, $z = 0$ ——positive, - - - - negative. (a) $c_s = 0.95$, (b) $c_s = 0.8$, (c) $c_s = 0.7$ (d) $c_s = 0.6$ 64

4.5 Contours u-perturbation velocity.$Re = 1000$, $c_1 = 0.05$, $t = 45$. Contour values start from -0.025, increment 0.01, $z = 0.556$ ——positive, - - - - negative. (a) $c_s = 0.95$, (b) $c_s = 0.8$, (c) $c_s = 0.7$, (d) $c_s = 0.6$ 66

4.6 v profiles at $t = 35$, $y = 4.22$. (a) $c_s = 0.8$ and (b) $c_s = 0.6$ 67

5.1 Eigenvaules of the normal vorticity equation. $Re = 1000$, $\alpha = 0.3$, $\beta = 0$. 84

5.2 Eigenfunctions of the normal vorticity equation. (a) Mode $s1$, $c = 0.959 - i0.041$, (b) Mode $s3$, $c = 0.796 - i0.203$, (c) Mode $s2$, $c = 0.460 - i0.238$. Mode $s1$ is concentrated around channel centre, $z = 0$, whereas Modes $s3$ and $s2$ near the walls, $z = 1$ 86

5.3 u perturbation contours calculated from eigenfunctions. $Re = 1000$, $t = 45$, $c_s = 0.8$. Contours start from -0.025, increment 0.01, $z = 0$. (a) $s1$, (b) $s2$, (c)$s3$ and (d) $s1 + s2 + s3$ 88

5.4 v profiles for $c_s = 0.8$ at $t = 35$, $y = 4.22$ calculated from eigenfunctions. (a) $s1$, (b) $s1 + s3$, (c) $s1 + s2 + s3$, (d) $s1 + s2 + s3 + s4$, (e) $s1 + s2 + s3 + s4 + s5$, (f)$s1 + s2 + s3 + s4 + s5 + s6$ 91

6.1 Normal velocity contours at $z = 0$. Contours start at -0.0000025, increment=0.000001. (a)$t = 0.0$, (b)$t = 10$, (c)$t = 20$, (d)$t = 30$, (e)$t = 40$, (f)$t = 50$. 115

6.2 Streamwise perturbation velocity. Contours start at -0.000005, increment=0.000002. (a) $t = 20$, (b)$t = 30$, (c)$t = 40$, (d)$t = 50$. 117

6.3 Growth rate, ω_i *.vs.* streamwise wavenumber, α. Each line has a fixed β value. 118

6.4 $\omega_i Re$ as a function of β for $\alpha = 0$. 119

6.5 Growth rate for 2-dimensional waves at different Reynolds numbers . . . 120

6.6 Growth of total energy E_t and partial energy E_p in natural logarithmic scale 121

6.7 Contours of w for $c_s = 0.6$. Contours start at -0.0000025, increment=0.000001. (a)$t = 0$, (b)$t = 10$, (c)$t = 20$, (d)$t = 30$. 123

6.8 Contours of w for $c_s = 0.7$. Contours start at -0.0000025, increment=0.000001. (a)$t = 20$, (b)$t = 30$. 124

6.9 Contours of w for $c_s = 0.8$. Contours start at -0.0000025, increment=0.000001. (a)$t = 20$, (b)$t = 30$. 125

6.10 Contours of w for $c_s = 0.95$. Contours start at -0.0000025, increment=0.000001. (a)$t = 20$, (b)$t = 30$. 126

6.11 Contours of plots for $c_s = 0.7$ at $t = 20$. (a) u-contours start at -0.05, incr=0.02, (b)w-contours start at -2.5×10^{-6}, incr=10^{-6} 127

7.1 Contours of w in unmodified flow field. $Re = 1000$, $c_1 = 0$. Contours are $w = -0.02$, -0.01, 0.01 and 0.02. (a) $t = 10$, (b) $t = 20$. 139

7.2 Contours of w. $Re = 1000$, $c_1 = 0.1$, $c_s = 0.6$. Contours plotted are $w = -0.02$ and $w = 0.02$. (a) $t = 0$, (b) $t = 10$, (c) $t = 20$ and $t = 30$. . 141

7.3 Amplitudes of wave crests as functions of time. Numbers 1 to 5 indicate different waves crests shown in the figure of the previous page 142

7.4 The r.m.s. amplitude of w as a function of time 143

7.5 Spreading of the strong wave group. □: front, ○: side and △: rear . . 144

7.6 $z = 0$, $t = 55$. (a) R.m.s. value of w. Lowest contour value=0.02, highest=0.10, incr=0.02. (b) Streamwise mean velocity. Lowest contour=0.7, highest 1.06, incr=0.02 145

7.7 Contour plots of normal velocity, w. The symmetric forcing is turned off at $t = 55$ and wave breakdown begins. (a) $t = 70$, (b) $t = 80$. 146

7.8 Migration of the flow "state", (Re, A), into the unstable region from the original stable "state", (Re_1, A_1). The solid curve is the secondary instability boundary. In the direction marked 1, Re increases accompanied by a decrease in A. In direction 2, Re decreases and A increases 147

Nomenclature

Roman Letters

A	Amplitude of perturbations
c_s	Speed of assumed forcing in the laboratory frame
c_1	Strength of the symmetric part of the assumed forcing
c_2	Strength of the antisymmetric part of the assumed forcing
c_j	(a) Eigenvalue of the normal vorticity equation
	(b) Eigenvalue of the Orr-Sommerfeld equation
E_t	Total perturbation enery defined $E_t = (u - U)^2 + v^2 + w^2$
E_t	Partial perturbation enery defined $E_t = v^2 + w^2$
f	Real function representing the z-direction distribution of the assumed forcing
H_1	Length of the domain of computation
H_2	Width of the domain of computation
h	Channel half depth
i	The imaginary unit equal to $\sqrt{-1}$
L	Number of x-direction Fourier modes retained
M	Number of y direction Fourier modes retained

N	Number of difference steps over the depth of the channel
p	Perturbation pressure
$\hat{p}$	fourier coefficient of p
q	A quatity representing any of u, v, w and p
Re	Reynolds number based on the channel half-depth
t	Time
$U(z)$	Flow velocity profile of unmodified flow
u	Velocity in x-direction
$\hat{u}$	Fourier coefficient of u
$\vec{v}$	Perturbation velocity vector
v	Perturbation velocity in y-direction
$\hat{v}$	Fourier coefficient of v
w	Perturbation velocity in z-direction
$\hat{w}$	Fourier coefficient of w
x	Streamwise co-ordinate
y	Spanwise co-ordinate
z	Co-ordinate in perpendicular to the channel walls

Greek Letters

α	x-direction wavenumber
β	y-direction wavenumber

Δt	Time step size
ϵ	Parameter proportional to the standard deviation of the Gaussian function
μ	Viscosity coeeficient
ν	Kinematic viscosity
ρ	Fluid density
σ	Growth rate of stream perturbation
$\Phi_j(z)$	The j's eigenfunction of the normal vorticity equation
$\phi_j(z)$	The j's eigenfunction of the Orr-Sommerfeld equation
$\psi_j(z)$	Stream function
$\Omega(z)$	Fourier transform of the normal vorticity
$\vec{\omega}$	Vorticity vector
ω_3	Normal vorticity
ω_i	Growth rate of Tollmien-Schlicting waves

Chapter 1

Introduction

The laminar-turbulent transition process in a shear flow is one of the most studied subjects in fluid mechanics. In his pipe flow experiment, Reynolds (1883) showed that two types of flows existed – laminar and turbulent, the transition from the former type to the latter type taking place when a non-dimensional parameter exceeded an critical value. This non-dimensional parameter is now called the Reynolds number. At the critical Reynolds number, he found that the flow had an intermittent character – localized turbulent regions which are separated by laminar regions appear in the pipe. These are the earliest evidences of turbulent spots. He speculated that the breakdown of laminar flow was due to instability of the flow to disturbances. Although a century has passed, the study of transition, initiated by Reynolds (1883), is still being extensively pursued.

This chapter briefly reviews the previous studies on this subject, paying special attention to the investigations in localized disturbances and also giving an outline to the present work. Since most discussions are related to Blasius boundary layer and plane Poiseuille flows and involve references to Reynolds numbers and length scales *etc*, we will define these quantities below.

The Reynolds number is based on the displacement thickness and edge velocity for Blasius boundary layer flows and on the channel half-depth and channel centre-plane velocity for plane Poiseuille flows unless otherwise stated. All the length scales, velocity scales and time scales are non-dimensionalized with these quantities in their respective cases. For example, a downstream distance of 10 in a plane Poiseuille flow implies 10 times the channel half-depth and a velocity of 0.5 means half of the edge velocity for Boundary layer or half of the centre-plane velocity for plane Poiseuille flow. Non-dimensionalization for plane Poiseuille flows will be explained in more detail later in this thesis. For this chapter, the above descriptions are sufficient.

1.1 Two dimensional instability

The study of instability mechanisms leading to turbulence began with the analysis of perturbations to simple flows. Rayleigh (1887) was the first to study the stability properties of fluid motions by analyzing the evolution of infinitesimal wave-like disturbances in an inviscid parallel shear flow. He derived the governing equation, which bears his name today, and showed that a necessary condition for an inviscid parallel flow to become unstable was that the mean velocity profile had an inflexion point. A stronger form of this condition was obtained much later by Fjørtoft (1950), which requires, loosely speaking, not only an inflexion point in the mean velocity profile, but also maximum vorticity at the inflexion point. Examples of shear flows with inflexional points can be found in boundary layers in adverse pressure gradients.

In flows which are not inflexional, *e.g.* plane Poiseuille flow, viscous effects are important in causing the instability. Orr (1907) and Sommerfeld (1908) independently derived the equation governing the linear stability of viscous parallel flows – the Orr-Sommerfeld equation. The asymptotic solution of Heisenberg (1924) to the Orr-Sommerfeld equation showed that inviscidly stable flows can be unstable at large but finite Reynolds numbers. Tollmien (1929, 1935) and Schlichting (1933) developed Heisenberg's theory and estimated, for the Blasius boundary layer, a value for the critical Reynolds number (the Reynolds number above which some infinitesimal disturbances grow) and obtained the normal variation of the wave disturbances. These infinitesimal wave disturbances are called Tollmien-Schlichting waves. Squire (1933) showed that the first wave to become unstable as the Reynolds number was increased was always two-dimensional. Consequently, two-dimensional perturbations had been extensively studied.

The experimental verification of the existence of the Tollmien-Schlichting waves was first done by Schubauer & Skramstad (1948), who used the vibrating ribbon technique in a low turbulence wind tunnel and showed that Tollmien-Schlichting waves were excited in a Blasius boundary layer. They experimentally determined that the stability boundary and critical Reynolds number agree, on the whole, with linear stability theory. This experiment demonstrated that Tollmien-Schlichting waves are indeed responsible for the initial stages of laminar-turbulent transition in boundary layer flows. Gaster (1974), among others, took into account the growth of the boundary layer, leading to even better agreement between theory and experiment.

In contrast to the boundary layer flow, whose Reynolds number increases as a disturbance is followed downstream because of the boundary growth, the plane Poiseuille flow is an exact parallel flow and has constant Reynolds number everywhere in the flow field. Orszag (1971) developed an accurate numerical method for solving the Orr-Sommerfeld equation by expanding the eigenfunctions in Chebyshev series. For plane Poiseuille flow, he showed, among other things, that the critical Reynolds number was 5772.22. Experiments by Nishioka, Iida & Ichikawa (1975) approximately confirmed the numerical results. They studied the stability of plane Poiseuille flow using a channel of rectangular cross section with an aspect ratio (the ratio of width to depth of the channel) of 27 and very low background turbulence level (0.05 %) and showed that under very carefully controlled conditions, small amplitude waves excited by a vibrating ribbon became unstable at a Reynolds number of about 6000. They also demonstrated that finite amplitude waves could grow at subcritical Reynolds numbers.

In order to understand the early stage of the laminar-turbulent transition following the initial growth of the infinitesimal waves and to explain the subcritical instability observed in certain parallel parallel flows, finite amplitude disturbances must be analyzed. The nonlinear stability theory for finite amplitude disturbances was first considered by Landau (1944). When the Reynolds number of the flow is in a small neighbourhood of the critical Reynolds number, unstable waves are confined to a small band of wave numbers close to the most unstable wave. Since other waves are stable and decay relatively fast, this most unstable wave will soon become dominant and will generate its harmonics and cause distortions to the mean flow. Landau gave an equation (Landau equation) governing the growth of the amplitude of the dominant waves. A parameter in this

equation, called the Landau constant, determines the nonlinear stability characteristics of the flow. Meksyn & Stuart (1951) and Stuart (1960) showed that plane Poiseuille flow was subcritically unstable to finite amplitude disturbances, *i.e.* disturbance grows when the disturbance amplitude exceeds a threshold and the Reynolds number is lower than the critical value. They found that this instability occurs when the Reynolds number exceeded about 2800 with a threshold of about 8%. Orszag & Kells (1978) numerically solved the Navier-Stokes equations and found nonlinear instability first set in at Reynolds number 2800. Rozhdestvensky & Simakin (1984) computed this Reynolds number to be 2855.

Herbert (1977) computed the threshold amplitudes above which two-dimensional disturbances grow for various subcritical Reynolds numbers ($Re < 5772$). His results agree qualitatively with the experimental data of Nishioka *et al.* (1975) at low disturbance frequencies. At high frequencies, the computation showed that the threshold increases monotonically with frequency. On the other hand, the experiment showed that, at high frequencies, the threshold reached a local maximum before dropping rapidly on further increase of the frequency. This may have been due to three-dimensional effects present in the experiment.

1.2 Three-dimensional instabilities

Turbulence is a three-dimensional phenomenon. The investigations of flow instability leading to turbulence have to include the study of the three-dimensional evolution

of the disturbances to laminar flows. Many three-dimensional instability mechanisms have been analyzed over the years. Klebanoff, Tidstrom & Sargent (1962) experimentally investigated the three-dimensionality of the boundary layer transitions using the vibrating ribbon technique. Below the ribbon tapes were regularly placed to produce a controlled spanwise variation. The resulting flow showed peak and valley patterns along the wave crests. The lambda vortices that were found to form from the these structures quickly broke down to turbulence. Herbert (1983) investigated the instability of plane Poiseuille flow to subharmonic and three-dimensional disturbances. He superposed three-dimensional small disturbances on the periodic, finite amplitude waves at subcritical Reynolds numbers and found that the peak and valley structures can develop rapidly. Orszag & Patera (1980, 1981, 1983) analyzed subcritical transition to turbulence and showed that two-dimensional primary finite amplitude waves were exponentially unstable to three-dimensional linear secondary waves along the crest of the primary waves. By effectively using "frozen" primary disturbances (since neutral solutions do not exist for the primary waves at about $Re < 2800$), they found that secondary waves can grow above $Re \approx 400$. They also used numerical simulation to study the growth of the secondary waves, allowing the primary waves to decay with time, and showed that the "critical" Reynolds number of the secondary wave growth is around 1000.

A different three-dimensional growth mechanism was analyzed by Gustavsson & Hultgren (1980) and Gustavsson (1981) — resonant growths in plane Couette and plane Poiseuille flows respectively. At subcritical Reynolds numbers, the resonance between velocity and vorticity normal to the walls causes the disturbance to grow linearly for

some time before decaying at subcritical Reynolds numbers. At $Re = 1000$, Gustavsson (1981) found that the resonant growth can last about 15 nondimensional time units in plane Poiseuille flow (based on channel half-depth and centre-line velocity).

Since the Reynolds number is large in many fluid dynamic problems of interest, the inviscid analysis may be used to approximate the evolution of perturbations in non-inflexional flow fields for some time before viscous effect become important. Landahl (1975) showed that a major part of the streamwise momentum was retained when a fluid particle was displaced across the shear layer in an inviscid flow . He showed that this "permenant scar" does not decay. Using piecewise linear profiles to approximate a boundary layer, Gustavsson (1978) considered the development of a three-dimensional initial perturbation. He found analytically that the solution could be identified as consisting of two parts – one dispersive part which travelled at speeds according to the dispersion relations and one advective part which travelled with the local velocity of the unperturbed flow and did not decay, consistent with Landahl (1975). Landahl (1980) showed that, subject to certain constraints, the perturbation energy following a three-dimensional initial disturbance in an inviscid flow would grow and it had a lower bound which grew linearly with time.

1.3 Localized disturbances and turbulent spots

In addition to the investigations focused on the global instabilities discussed above, the response of a shear flow to local disturbances are also of interest because globally

uniform disturbances are unlikely to occur in reality. Gaster & Grant (1975) experimentally investigated the formation and development of a wave packet in a laminar boundary layer created by a pulsed disturbance at a point on the boundary. Their experimental results were compared with the theoretical model of Gaster (1975), in which the wave packet resulting from a pulsed disturbance was modeled as a superposition of solutions to the Orr-Sommerfeld equation, and good agreement was found. From these results, one concludes that linear theory will predict that a linear wave packet in a shear flow will grow only at supercritical Reynolds numbers so that such a calculation would not be able to explain the observed growth of turbulent spots at subcritical Reynolds numbers in plane Poiseuille flow.

Henningson (1988) used the approach of Gustavsson (1978) to analyze the time evolution of a small localized disturbance in an inviscid plane channel flow with a piecewise linear profile to approximate the parabolic velocity profile of plane Poiseuille flow. He showed that the velocity component normal to the walls is largely dispersive and decaying, and that the velocity components parallel to the walls are dominated by the advective part and do not decay, due to the "permanent scar" effect (Landahl, 1975). Breuer & Haritonidis (1990) studied the evolution of localized, weak disturbances in a laminar boundary layer both theoretically and experimentally. Their calculations based on linear inviscid theory showed that the advective part of the solution took the form of an inclined, elongating shear layer and did not decay. The amplitude of the advective part of the solution exceeds by far that of the dispersive part. These findings were confirmed by their experiments for some distance downstream before the viscous effect caused the advective part to decay. The corresponding evolution of strong dis-

turbances were analyzed by Breuer & Landahl (1990). They solved the Navier-Stokes equations with the localized initial disturbance located at $Re = 950$ (based on displacement thickness). They found that the dispersive part of the solution evolved according to Tollmien-Schlichting instability theory and the advective part grew much more rapidly than the dispersive part, giving rise to two distinct nonlinear effects which, respectively, produced streamwise low speed streaks and caused secondary instabilities on the vertical shear layer formed as a result of spanwise stretching of the mean vorticity.

The appearance of turbulent spots in the surrounding laminar flows is a localized mechanism by which the laminar turbulent transition can occur. Emmons (1951) examined a thin layer of water running down an inclined plane and observed localized regions of turbulence – the turbulent spots. Subsequently, turbulent spots are found in other flows such as boundary layer and plane Poiseuille flows. Wygnanski, Sokolov & Friedman (1976) studied the growth of turbulent spots in a Blasius boundary layer and found that the rate of spreading of the spot is very nearly independent of Reynolds number. Wygnanski, Haritonidis & Kaplan (1979) measured the laminar flow outside such a turbulent spot and found wave packets consisting of Tollmien-Schlichting waves trailing the spot and concluded that the breakdown of the these waves to turbulence caused the enlargement of the spot. Gad-el-Hak, Blackwelder & Riley (1981) showed that "growth by destabilization" was responsible for the spreading of the spot, *i.e.* the flow field outside the turbulent spot was destabilized.

Carlson, Widnall & Peeters (1982) were the first to present a flow visualization study

of the growth of turbulent spots in plane Poiseuille flow using a water channel of width-to-depth ratio of 133 and observed that both natural and artificially-triggered turbulent spots could grow at Reynolds numbers as low as 1000. They obtained photographs of the turbulent spots showing strong oblique waves in the laminar flow surrounding the spot. The spot expands into the flow with a spreading half-angle of about 8 degrees. The front of the spot travelled with a speed of about 2/3 the centerline velocity and rear at about 1/3. After growing to a size of some 35 times the channel half-depth at a downstream distance of about 130 from the trigger, the spot began to split into two spots, accompanied by strong wave activity. They suggested that wave propagation and breakdown play a crucial role in transition to turbulence in a plane Poiseuille flow. Bullister & Orszag (1983) numerically simulated the turbulent spot in plane Poiseuille flow at $Re = 6000$ with a computational box of $20 \times 5 \times 2$ in the streamwsie, spanwise and normal directions respectively. A turbulent spot was generated by using a localized force to drive a jet of fluid vertically, then allowing the disturbance to develop. However, since the Reynolds number used was above the critical value predicted by linear stability theory, the simulation does not offer an explanation to the transition phenomenon at subcritical Reynolds numbers in plane Poiseuille flow. Their computational box had a spanwise dimension of the same order as the wavelength of the experimentally observed waves outside the turbulent spot, hence it was too small to show the observed turbulent spot features which is, at least, ten times larger in spatial extent. A flow visualization experiment of turbulent spots in plane Poiseuille flow was done by Alavyoon, Henningson & Alfredsson (1986) in the Reynolds number range 1100 to 2200, waves were observed outside the turbulent spot. The spreading half-angle varied approximately linearly from 6 to 12 degrees in this Reynolds number range (smaller than that observed by Carlson *et*

al., 1982). The speeds of propagation of the front and rear of the spot were, respectively, larger than those found by Carlson *et al.* Splitting of spots occurred only at low Re. Henningson & Alfredsson (1987) experimentally investigated the wave packets generated by the turbulent spot in plane Poiseuille flow by hot film anemometry. They found that the streamwise velocity disturbance associated with the waves was anti-symmetric with respect to the channel centre-line, and showed that the wave packet consisted of the locally, least-stable Tollmien-Schlichting modes. A symmetric disturbance in the spanwise velocity was found directed towards the spot downstream of the spot and away from the spot upstream, indicating a blockage effect, consistent with the idea of Widnall (1984). They also did a linear stability analysis of the modified velocity profiles measured in the experiment and found, by considering the eigenvalues of the Orr-Sommerfeld equation, that the modified flow field was slightly unstable. A full Navier-Stokes simulation was carried out by Henningson, Spalart and Kim (1987) for both the plane Poiseuille flow and flat plate boundary layer flow. They found that, at $Re = 1500$, the spot travelled with a speed of 0.8 at the front and 0.54 at the rear, and the side of the spot expanded into the surrounding laminar flow at a speed of 0.12. This is in agreement with the flow visualization results of Alavyoon *et al.* (1986), but has, respectively, larger streamwise and lower spanwise spreading rates than those found by Carlson *et al.* The "wing-tip" region consists of large amplitude waves. The simulation results were further analyzed by Henningson (1989). He studied two possible ways in which waves around the turbulent spot can grow and break down –the exponential wave growth as a result of the "cross-flow" instability due to the highly inflexional spanwise velocity profiles and the wave energy focusing mechanism analyzed by Landahl (1972). He found that the exponential growth is dominant throughout most of the regions

where waves were found, although both exponential growth and wave energy focusing are present close to the edge of the turbulent spot. The turbulent characteristics inside a turbulent spot in a plane Poiseuille flow were analyzed by Henningson and Kim (1990). They found that the mean and r.m.s fluctuations as well as the internal shear-layer structures in a turbulent spot are similar to those in a fully turbulent channel flow. The shear-layer structures in the wave regions outside the spot show similarities to those in the secondary instability of two-dimensional Tollmien-Schlichting waves.

In exploring the findings of Carlson *et al.* (1982), Widnall (1984) raised the following questions. First, how is the turbulent spot able to grow in a stable viscous background where all linear and weakly nonlinear free waves decay? Second, how and why are the waves generated? Is there a preferred wavelength? Finally, what role do the waves play in the growth of the localized turbulence? Widnall proposed that the turbulent spot acts as a region of disturbance which generates waves in a manner similar to that of a ship moving on a free surface and forces the oblique waves to amplitudes such that they become unstable to three-dimensional secondary disturbances. These instabilities break down further into small-scale turbulence which increases the size of the region of disturbance and the cyclical process continues. A mathematical model was constructed which modelled the region of disturbance as a steady travelling delta-function, leading to a non-homogeneous Orr-Sommerfeld equation. Unlike the solution of a pulsed disturbance in a subcritical shear flow which would decay downstream at the Reynolds number considered ($Re = 1000$), a solution forced by a travelling disturbance will retain its form. A far-field solution was obtained using the method of stationary phase which showed qualitative agreement with the experiment of Carlson *et al.* (1982).

Further work along this line was done by Li & Widnall (1989). They modelled the turbulent spot as a region of increased Reynolds stress and used it as a forcing term in the linearized Navier-Stokes equations to solve for the wave field so generated. They found that the waves around the disturbance had approximately the same wavelength as those found in experiments (Carlson *et al.*, 1982 and Henningson *et al.*, 1987). When the forcing was antisymmetric (resulting in antisymmetric perturbations to the streamwise velocity about the channel centre-plane), a wave packet is generated. Whereas, when the forcing was symmetric, no obvious wave crests could be seen and the effect of the forcing was simply to distort the velocity profiles of a plane Poiseuille flow. The forcing was made to travel at different speeds and it was found that the most effective wave generation was achieved when the forcing travelled at about 0.4 of the channel centre-plane velocity at $Re = 1000$. Since this velocity (0.4) was approximately the phase speed of the least damped Tollmien-Schlichting mode, they suggested that the most effective wave generation was due to near-resonance of the forcing with the Tollmien-Schlichting mode.

1.4 Motivation for the present study

A turbulent spot in a boundary-layer eventually travels into regions where the Reynolds number is above critical, and the linear instability helps its growth. It is quit another story for a plane Poiseuille flow where the Reynolds number is constant, subcritical growth of a turbulent spot is certainly not a consequence of the linear instability of the parabolic velocity profiles. The secondary instability theory can not be

applied directly to explain the breakdown of the waves at Reynolds numbers of about 1000 since neutral primary waves with finite amplitudes do not exist at these Reynolds numbers. The numerical solution of Orszag *et al.* (1983) showed that secondary instability could grow on decaying finite amplitude primary waves at about $Re > 1000$, but the rate of growth was small since $Re \approx 1000$ was the boundary between growing and decaying secondary waves. The resonance-growth mechanism (Gustavsson, 1981) indicates that the streamwise and spanwise velocity perturbations could grow for some time at $Re = 1000$, but the normal velocity should decay. Therefore, it alone does not explain the observed strong waves in the normal velocity. Likewise, other theories discussed in the last section which predict growth only in the streamwise and spanwise velocities cannot alone explain the growth of strong waves in the normal velocity around a turbulent spot in plane Poiseuille flow. The "cross-flow" instability mechanism in regions of modified flow field outside the spot analyzed by Henningson (1989) is responsible for the wave growth outside of the turbulent spot.

Some important differences in the known experiments of plane Poiseuille flow spot should also be noted. Flow visualizations of artificially triggered turbulent spots by Carlson *et al.* (1982) and by Alavyoon *et al.*(1987) and experiment of Henningson *et al.* (1987) all showed the presence of waves with approximately the same wavelengths, phase speeds at later stages of the spot development. However, photographs of turbulent spots taken by Carlson *et al.* (1982) showed strong oblique waves all around a turbulent spot in the early stages of the spot development, whereas those by Alavyoon *et al.* (1987) showed strong wave activities mainly near the "wing tips". The numerical simulation of Henningson *et al.* (1987) showed that the waves outside the turbulent spot look much

like those in Alavyoon *et al.* (1987). In Carlson *et al.* (1982), the spots with strong waves all around were early stage spots photographed at distances of 32, 50 and 64 downstream of the trigger. In Alavyoon *et al.* (1987), the spot was photographed at distances of above 100 downstream of the trigger. In the later stages of the spot development (*i.e.* at downstream distances of above 100 from the trigger), the results of Carlson *et al.* (1982) and Alavyoon *et al.* look very similar — strong wave activity near the destabilized "wing tip" regions, where the spanwise velocity profiles are highly inflexional. Following the asymmetric triggering of the turbulent spot in an experiment, *e.g.* by the injection of a small amount of fluid into the flow from a hole on one of the walls of the channel, the turbulent spot wound take some time to become symmetric across the channel in a statistical sense (*i.e.* the ensemble averaged streamwise and spanwise velocities are symmetric across the channel). This asymmetry may well generate forced waves in the same manner as does a ship moving on a free surface (see Widnall, 1984 and Li & Widnall, 1989). Further downstream, the spot becomes statistically symmetric. The linear analysis of Li & Widnall (1989) showed that a modelled symmetric spot does not produce waves of wavelengths comparable to those of the experimentally observed waves, but rather has the effect of distorting the flow around it. Therefore, the waves in the regions outside a well-developed turbulent spot cannot be forced waves, they must arise from the instability of the modified flow field (Henningson, 1989).

We now list the major known facts about a turbulent spot in a plane Poiseuille flow:

- A turbulent spot in a plane Poiseuille flow can grow at Reynolds numbers of about 1000, much lower than the critical Reynolds number predicted by linear

theory and nonlinear theory. Hence, a plane Poiseuille flow can undergo transition subcritically (Carlson *et al.*, 1982, and Alavyoon *et al.*, 1986)

- The spot travels downstream and grows in size. The front of the spot travels at about 80 % of the channel centre-line velocity and rear at about 54 % at $Re = 1500$. The rate of spreading increases as Reynolds number increases (Henningson *et al.*, 1987). The lateral spreading of the spot increases approximately linearly with Reynolds number (Alavyoon *et al.*, 1986)

- The presence of a turbulent spot in a plane Poiseuille flow modifies the surrounding laminar flow to create instabilities. The regions outside the turbulent spot where the distorted mean velocity profiles are highly inflexional (*i.e* unstable), as a result of the presence of the spot (Henningson, 1989).

- Waves which consist of locally unstable Tollmien-Schlichting modes are found in these unstable regions. (Henningson *et al.*, 1987). The exponential growth of these waves and their breakdown are mainly responsible for the spreading of the turbulent spot although the wave energy focusing is also important close to the edge of the spot and the subsequent breakdown of these waves show characteristics of the secondary instability (Henningson *et al.*, 1989).

- The wave field outside an asymmetrically triggered spot in experiments looks different in early stages from later stages of its development. In the early stage waves are found all around the spot, whereas in later stages they are found only near the front of the spot (compare Carlson *et al.*, 1982 and Henningson *et al.*, 1987). Wavenumbers (non-dimensionalizd with the channel half-depth) of typical waves are just under 2.0 (Henningson, 1989).

- The statistical characteristics of the turbulence inside the spot are similar to those of the fully developed turbulence in a channel (Henningson *et al.*, 1989).

The mechanism of the growth of the turbulent spot in plane Poiseuille flow is summarized in Figure 1.1: (1) The turbulent spot acts as a partial blockage and modifies surrounding laminar mean flow. (2) The modified laminar mean flow is unstable to small perturbations, resulting in wave growth. (3) The waves grow to large enough amplitudes and become susceptable to secondary instability. They break down to turbulence and hence enlarge the spot. (4) The laminar mean flow is not modified by the spot alone. The finite amplitude waves could also modify the mean flow before the waves break down.

In this thesis, the turbulent spot in Figure 1.1 is replaced by a simple model. Effects (1) and (2), *i.e.* mean flow modifcations by the model and linear wave growth, are analyzed in some detail. Effect (3) is examined for finite amplitude wave growth. Secondary instability and wave breakdown are are outside the scope of this thesis.

Some questions can still be raised about the transition in plane Poiseuille flow via turbulent spots:

- What is the nature of the destabilized regions outside a spot? In other words, can the modified velocity profiles in these regions be best represented by a few eigenmodes of some fundamental fluid dynamics equations?
- If so, which modes are most responsible of the destabilization of the flow field?

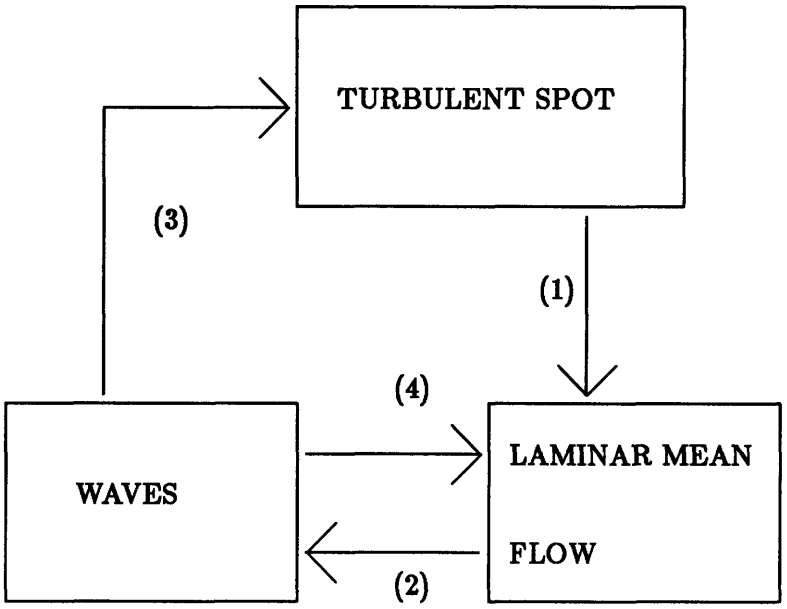

Figure 1.1: Schematic diagram of the turbulent spot growth cycle

- Why does the turbulent spot travel downstream at a speed lower than the channel centre-line speed?
- Why is the appearance of the wave field different in early and later stages of the development of the spot? Can the nature and origins of these different waves be identified?

Analyses designed to answer the above questions forms the basis of this thesis.

1.5 Organization of this thesis

Chapter 2 discusses the assumptions about the Reynolds stress, and the modelling of the turbulent spot.

Chapter 3 introduces the numerical method used in this thesis to solve the incompressible Navier-Stokes equations in a channel.

Chapter 4 shows the results for the large scale flow field modifications by the modelled spot, *i.e.* Effect (1) shown in Figure 1.1.

Chapter 5 shows the decomposition of these modifications into the normal vorticity modes.

Chapter 6 discusses how linear waves behave in the unmodified flow and how the modification of the flow field drastically changes the stability properties of the linear waves, *i.e* Effect (2).

Chapter 7 demonstrates how finite amplitude wave behave in the unmodified and modified flows, *i.e.* Effects (3) and (4).

Chapter 8 is a summary of this thesis.

Chapter 2

Formulation

In this chapter, the geometry of the channel, the orientation of the axes, the governing equations and the model for the turbulent spot are presented.

2.1 The geometry and the orientation of axis system

Plane Poiseuille flow is a flow between two parallel plates of infinite extent separated at a distance of $2h$ and driven by a constant, unidirectional pressure gradient. The flow is parallel to the walls and has a parabolic velocity profile in the steady state. The $x-$axis is in the direction of the flow. The $z-$ axis is perpendicular to the walls. The direction normal the $x-z$-plane is the y-direction which is parallel to the walls and normal the flow direction. Three axes in these directions form a right-handed coordinate system. This system of axes are allowed to travel with specified constant speeds in the x-direction to facilitate the computation and the presentation of results. The x, y and z-directions are also called the streamwise, spanwise and normal directions, respectively. The velocity components in these three directions are u, v and w, respectively. Figure 2.1 shows the geometry of the channel and the axes described above.

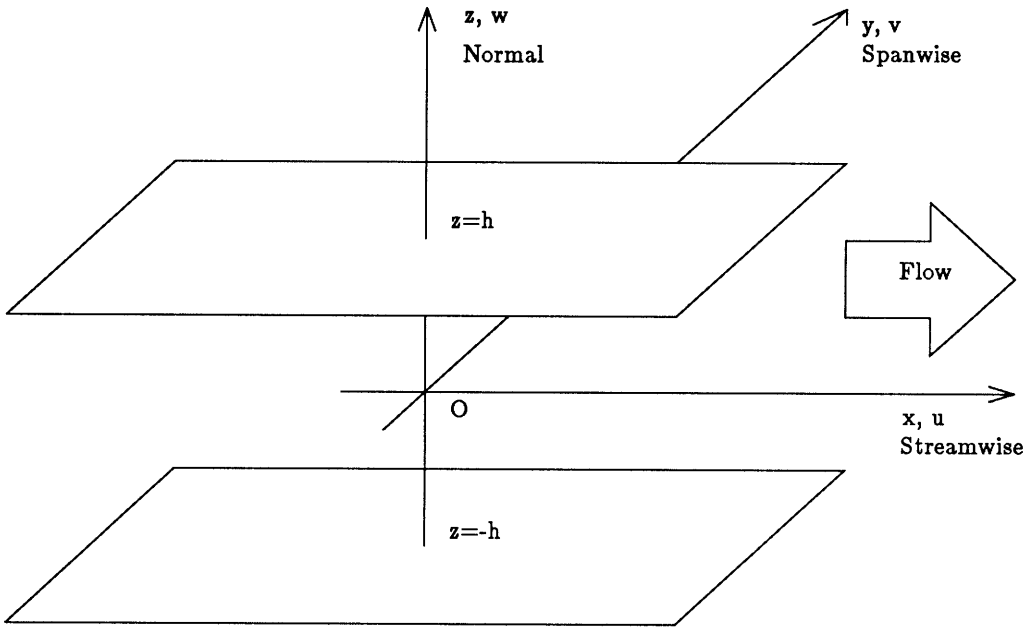

Figure 2.1: The geometry of the channel and the axis system

2.2 Governing equations

Viscous, incompressible flows such as flows in a channel are governed by the Navier-Stokes equations. The velocity and pressure fields can be split into mean and random fluctuating quantities. Taking an ensemble average of the Navier-Stokes equations, we obtain a new set of equations - the Reynolds averaged Navier-Stokes equations. There are additional terms in these averaged equations, the Reynolds stresses, representing the "apparent" stresses due to turbulent fluctuations.

Before presenting the governing equations, we first non-dimensionalize the velocity vector, pressure and Reynolds stresses by appropriate quantities. All components of the velocity vector $\vec{v}$, — (u, v, w) in the x, y and z directions, respectively, are non-dimensionalized with U_o, the channel centreline velocity of the unperturbed parallel flow. The pressure and the Reynolds stresses are non-dimensionalized with ρU_0^2, ρ being the density of the fluid. All length scales are non-dimensionalized with the channel half-depth, h. The Reynolds number is,

$$Re = \frac{\rho U_0 h}{\mu},$$

where μ is the viscosity of the fluid.

The non-dimensional Reynolds-averaged Navier-Stokes equations in rotational form are as follows:

$$\frac{\partial \vec{v}}{\partial t} = \vec{v} \times \vec{\omega} - \nabla \Pi + \frac{1}{Re} \nabla^2 \vec{v} + \vec{F}, \tag{2.1}$$

$$\nabla \cdot \vec{v} = 0, \tag{2.2}$$

where $\vec{\omega} = \nabla \times \vec{v}$, $\Pi = p + \frac{1}{2}\vec{v} \cdot \vec{v}$ (the fluid density, ρ, has been absorbed into the non-dimensional pressure). The vector $\vec{F}$ represents the nondimensional Reynolds stress:

$$\vec{F} = -\begin{pmatrix} \frac{\partial \overline{u'^2}}{\partial x} + \frac{\partial \overline{u'v'}}{\partial y} + \frac{\partial \overline{u'w'}}{\partial z} \\ \frac{\partial \overline{u'v'}}{\partial x} + \frac{\partial \overline{v'^2}}{\partial y} + \frac{\partial \overline{v'w'}}{\partial z} \\ \frac{\partial \overline{u'w'}}{\partial x} + \frac{\partial \overline{v'w'}}{\partial y} + \frac{\partial \overline{w'^2}}{\partial z} \end{pmatrix}, \tag{2.3}$$

The frame of reference is made to travel at a constant speed, c_s, in the streamwise direction. Thus, non-slip conditions at the walls give $\vec{v} = c_s\vec{i}$ at $z = 1$ and $z = -1$ as boundary conditions.

If the whole flow field is laminar, the Reynolds stress term given by (2.3) vanishes. If part of the flow field is turbulent, *e.g* there is a turbulent spot present, (2.3) is non-zero within the turbulent region, but vanishes elsewhere. We will use this fact to the model the turbulent spot, *i.e.* to assume a simple form for (2.3).

2.3 Modelling the Reynolds stress

Our aim is to investigate the laminar flow field outside the turbulent spot, *i.e* the wave field and the distortions to the mean velocity profiles caused by the presence of the spot, but not the turbulence within the spot itself. This will guide the assumptions and simplifications made in this section.

The system of equations (2.1) to (2.3) is not closed because there are more unknowns than there are number of equations (the Reynolds stress term (2.3) is considered unknown). In order to complete the closure of the equations, we have to assume some form for the Reynolds stresses in Equation (2.3).

2.3.1 Fully turbulent flow in a channel and the turbulent characteristics within a turbulent spot

In order to model the turbulent region, we will review some known facts about fully turbulent channel flows and the turbulence within a turbulent spot.

The averaged quantities in a fully turbulent channel flow are well known (see, for example, Landahl & Mollo-Christensen, 1986). Since the averaged flow quantities are independent of x and y, the only possible non-vanishing terms in Equation (2.3) are the z-derivatives of $\overline{u'w'}$, $\overline{v'w'}$ and $\overline{w'^2}$. If the second term were to be non-vanishing, it is necessary that there be a spanwise mean shear. In a fully turbulent, uni-directional

channel flow, the required spanwise mean shear is absent and therefore $\overline{v'w'}$ vanishes.

Henningson & Kim (1990) examined the turbulence within the turbulent spot using numerical simulation and found that the flow structures within a turbulent spot at $Re = 1500$ bear a strong resemblance to those found in the fully turbulent channel flows. They plotted the Reynolds shear stress $\overline{u'w'}$ with respect to z, showing the maximum occurs at about $z = \pm 0.7$. [1] They also evaluated the r.m.s. values of $\overline{u'^2}$, $\overline{v'^2}$ and $\overline{w'^2}$, showing that $\overline{w'^2}$ is much smaller than $\overline{u'^2}$ and that it varies much less rapidly across the channel than either $\overline{u'^2}$ or $\overline{v'^2}$. This may suggest that we can model the turbulent spot using the turbulent properties in fully turbulent flows and that $\partial\overline{w'^2}/\partial z$ can be neglected compared with $\partial\overline{u'w'}/\partial z$.

2.3.2 Assumptions

Except for $\overline{u'w'}$ from the the simulation of Henningson *et al.* (1990), we do not known very much about the Reynolds stresses in a turbulent spot at Reynolds numbers of the order of 1000. However, they found that the turbulent structures within a spot very much resemble those in a fully turbulent channel flow in which $\overline{u'w'}$ is dominant. Hence we assume that this is also true in a spot. We can also base this assumption on the experimental results of Carlson *et al.* (1982) and numerical simulation results of Henningson *et al.*(1987), which showed that a well-developed turbulent spot typically has a $x - y$ length scale of about 20 times the channel half-depth. Therefore, the the

[1] In their convention, this stress is denoted $\overline{uv}$

variations of the Reynolds stresses with respect to x and y are negligible compared to those with respect to z. Thus, the terms with x and y derivatives in (2.3) will be set to zero. This gives $\frac{\partial \overline{u'w'}}{\partial z}$, $\frac{\partial \overline{v'w'}}{\partial z}$, and $\frac{\partial \overline{w'^2}}{\partial z}$ as the only remaining terms to be considered.

The first term is non-zero everywhere inside the turbulent spot. The term $\overline{v'w'}$ is non-zero since there is mean spanwise shear. However, since the spanwise shear is small compared with the streamwise shear, we assume that $\overline{v'w'}$ is also negligible. The amplitude of the w' fluctuations was shown to be an order of magnitude smaller than that of u' near the walls, where turbulence is most intensive. Hence, the third term is also assumed negligible.

The assumption about slowly varing Reynolds stresses with respect to x and y may or may not be accurate at the sharply defined edge of the spot where turbulent flow changes to laminar flow. Also the effect of neglecting $\overline{w'^2}$ is not clear. However, since we are only interested in the development of waves outside the turbulent spot, we may use these assumptions. The comparison of results based on this model with full numerical simulations of Henningson *et al.* (1990) in the wave regions outside the turbulent spot will judge the validity of these assumptions.

2.3.3 Modelling the turbulence within a turbulent spot

After these assumptions, the only non-vanishing term left in Equation (2.3) is, $\frac{\partial \overline{u'w'}}{\partial z}$. Again since we are only interested in the flow field outside the turbulent spot, we will give

the remaining Reynolds stress term a simple form similar to that used by Li & Widnall (1989). Since the rate at which the spot spreads is relatively small (see, for example, Carlson *et al.*, 1982), we assume the spreading of the turbulent spot is negligible and that the modelled Reynolds stress is independent of time in a frame of reference travelling with the spot.

Since the turbulent spot is localized, we assume that the Reynolds stress distribution is Gaussian in x- and y-directions in the traveling frame, we have,

$$\tau_{xz} = -\overline{u'w'} = -\frac{1}{\epsilon^2} f(z) exp(-\frac{x^2+y^2}{\epsilon^2}), \tag{2.4}$$

where $f(z)$ represents the normal variation of the Reynolds stress and ϵ is a measure of the horizontal size of the modelled spot. Integrating Equation (2.4) over a fixed (x, y)-plane, the total strength of the forcing in this plane is found to be $\pi f'(z)$, independent of ϵ. In that sence, Equation (2.4) models the integrated strength of turbulence in the spot.

The Reynolds stress appear in the form of its z-derivative in (2.3). Since the distribution of the Reynolds shear stress in z is odd, and so its $z-$ derivative is even. Experimetal results, *e.g.* Eckelmann (1974), and theoretical models, *e.g.* Haritonidis (1989), of the $z-$variation of the Reynolds stress are available. However, we will use a simple model that takes into account of the qualitative features of the $z-$variation of the Reynolds stress. The assumed $f'(z)$ should vanish at the walls and two interier points (maximum stress). These requirements can be satisfied by the symmetric part

of the fourth order polynomial as given below:

$$\frac{df(z)}{dz} = (c_1(4z^2 - 1) + c_2 z)(1 - z^2), \tag{2.5}$$

where c_1 and c_2 give the strength of, respectively, the symmetric and antisymmetric[2] parts of the $z-$derivative of the Reynolds shear stress. In a well developed turbulent spot c_2 is zero since the turbulence inside the spot symmetrically fills the channel. At very short distances downstream of the spot trigger position the turbulence is not symmetric and non-vanishing c_2 is needed.

From the Reynolds shear stress at $Re = 1500$ shown in Figure 3 of Henningson *et al.* (1990), we deduced the maximum value of $\partial\overline{u'w'}/\partial z$, which is about 0.01 in the nondimensional units of the present work. Supposing we have a spot of area 20 in the (x, y)-plane, we find that the integrated strength is 0.2. Equating this to the maximum of $\pi f'(z)$ with $c_2 = 0$, we obtain $c_1 \approx 0.1$. This is just a very rough estimation, which gives the order of magnitude of c_1. Calculations done in the course of the present research show that, when $c_1 = 0.1$, the maximum spanwise velocity perturbation reaches about 10 percent of the channel centre-plane velocity in agreement with the numerical simulations of Henningson (1989).

The size of the forcing in a (x, y)-plane is proportional to ϵ. Although a turbulent spot grows as it travels downstream, its shape and the modified flow field around it remain self-similar. Therefore, the size of the spot is unimportant in determining the flow outside the spot. We choose $\epsilon = 2$ throughout this thesis unless otherwise stated

[2]See next section for the definition of symmetry

(*i.e.* the modelled spot has roughly the size of the channel depth).

2.4 Symmetry

The assumed forcing term appears as the $z-$derivative of the Reynolds stress. If we let c_2 vanish and c_1 be non-zero in Equation (2.5), the forced streamwise and spanwise velocities, u and v, will be symmetric with respect to the channel centre-plane, while the normal velocity w will be antisymetric. On the other hand, if we let c_1 vanish and c_2 be non-zero, the reverse it true. In the present work, we adopt the convention that the symmetry properties of the flow is the same as that of the streamwise velocity u, *i.e.* when we say a flow is symmetric, u and v are symmetric, but w is antisymetric and vice verse. In following chapters, the words "even" and "odd" are used to describe the properties of certain eigenfunctions and are not to be confused with the symmetry properties of the flow field.

Chapter 3

Numerical Methods

The Fourier-Chebyshev spectral method is used to solve the Reynolds averaged Navier-Stokes Equations (2.1) to (2.5) and the time splitting scheme of Orszag & Kells (1980) is implemented. The time-integration is done in three separate steps and the nonlinear term, $\vec{v} \times \vec{\omega}$, in (2.1) is evaluated using the pseudo-spectral method. This chapter describes this method in some detail.

3.1 Chebyshev polynomial approximations

The Chebyshev polynomial of degree n, is the solution of the differential equation

$$\sqrt{1-z^2}\frac{d}{dz}\sqrt{1-z^2}\frac{dT_n}{dz} + n^2 T_n = 0, \tag{3.1}$$

where $z \in [-1,1] \subset \mathbf{R}$ and $T_n(z) \in \mathbf{R}$. $T_n(z)$ is given by

$$T_n(\cos\theta) = \cos n\theta, \tag{3.2}$$

where $\theta = \cos^{-1} z$. Hence $T_0(z) = 1$, $T_1(z) = z$, $T_2(z) = 2z^2 - 1$, $T_3(z) = 4z^3 - 3z$, $T_4(z) = 8z^4 - 8z^2 + 1$ and so on. These polynomials are orthogonal in the following

sense:

$$\int_{-1}^{1} \frac{T_n(z)T_m(z)}{\sqrt{1-z^2}}dz = \frac{\pi}{2}e_n\delta_{nm}, \tag{3.3}$$

where $e_0 = 2$, $e_n = 1$ for $n > 0$.

A given complex function $f(z) \in \mathbf{C}$ can be expressed as an infinite sum of Chebyshev polynomials[1]

$$f(z) = \sum_{n=0}^{\infty} c_n T_n(z), \tag{3.4}$$

where $c_n \in \mathbf{C}$ can be found by making use of the orthogonal relation (3.3).

If the function $f(z)$ is known only at $N+1$ discrete points, $z_j = \cos\frac{\pi j}{N}$ ($j = 0, 1,$ ....., N), it can be expressed as a finite sum of T_n's

$$f_j = \sum_{n=0}^{N} c'_n T_n(z_j) = \sum_{n=0}^{N} c'_n \cos\frac{\pi jn}{N}. \tag{3.5}$$

where $f_j = f(z_j)$, $c'_n \in \mathbf{C}$ is, in general, not the same as c_n and is given by

$$c'_n = \frac{2}{Ne_n}\sum_{j=0}^{N} \frac{f_j}{e_j}\cos\frac{\pi jn}{N}. \tag{3.6}$$

Equations (3.5) and (3.6) can be evaluated using the Fast Fourier Transform technique (FFT).

[1]In general, $f(z)$ must satisfy certain conditions, which will not be discussed here. The same holds for Fourier transforms discussed later.

The first derivative of $f(z)$ at the discrete points is given by

$$(\frac{df}{dz})_j = \sum_{n=0}^{N} d'_n \cos\frac{\pi jn}{N}, \tag{3.7}$$

where

$$d'_N = 0$$

$$d'_{N-1} = 2Nc'_N$$

and

$$e_n d'_n = d'_{n+2} + 2(n+1)c'_{n+1}, \tag{3.8}$$

for $0 \leq n \leq N-2$, where $e_0 = 2$ and $e_n = 1$ for $n > 0$. Higher derivatives of $f(z)$ can be obtained by repeated application of Equation (3.8).

If the $(k-1)$'th derivative of $f(z)$ is continuous and the k'th derivative integrable, the error in the approximation in (3.5) is asymptotically smaller than $1/N^k$. Detailed descriptions of the Chebyshev approximation can be in Gottieb & Orszag (1977).

3.2 Fourier series approximations

We now discuss the more familiar Fourier series approximations. A given periodic, complex function $g(x) \in \mathbf{C}$ of period L, can be expressed as

$$g(x) = \sum_{n=-\infty}^{\infty} a_n e^{i\frac{2\pi nx}{L}}, \tag{3.9}$$

where $x \in (0, L) \subset \mathbf{R}$ and Inversely

$$a_n = \frac{1}{L}\int_0^L g(x) e^{-i\frac{2\pi nx}{L}}. \tag{3.10}$$

If $g(x)$ is known only at discrete points $x_j = Lj/N$ $(j = 0, 1, ..., N-1)$, Equations (3.9) and (3.10) become

$$g_j = g(x_j) = \sum_{n=-N/2}^{N/2-1} a'_n e^{i\frac{2\pi nj}{N}}, \tag{3.11}$$

$$a'_n = \frac{1}{N} \sum_{j=0}^{N-1} g_j e^{-i\frac{2\pi nj}{N}}. \tag{3.12}$$

The error in (3.11) as a function of N is asymtotically smaller than $1/N^k$ if the function, g(z), has $k-1$ continuous derivatives.(see Section 3 of Gottlieb & Orszag,1977). Equation (3.11) and (3.12) can be evaluated using FFT technique. The periodic solutions of the Navier-Stokes Equation analyzed by Orszag & Kells (1980) were represented with accuracy by only a few terms in the Fourier series .

3.3 Spectral representation of flow variables

Let $Q(x, y, z, t)$ be any flow variable $(u, \omega_x, ...)$. The Fourier-Chebyshev representation of Q is

$$Q(x, y, z, t) = \frac{1}{4\pi^2} \int_{-\infty}^{\infty} \int_{-\infty}^{\infty} \hat{Q}(\alpha, \beta, z, t) e^{i(\alpha x + \beta y)} d\alpha d\beta, \tag{3.13}$$

$$\hat{Q}(\alpha, \beta, z, t) = \sum_{n=0}^{\infty} \hat{\hat{Q}}(\alpha, \beta, n, t) T_n(z), \tag{3.14}$$

where α and β are x- and y- components of the wave number vector and $T_n(z)$ is the n'th order Chebyshev polynomial. The hat quantities are in Fourier-physical space (α, β, z) and the double hat quantities are in Fourier-Chebyshev space (α, β, n).

Fourier transforming Equation (2.4), we get the expression for the Reynolds stress in the Fourier-space,

$$\widehat{\overline{u'w'}} = -\pi f(z) exp[-\frac{\epsilon^2(\alpha^2+\beta^2)}{4}]. \tag{3.15}$$

3.4 The time splitting scheme

In this section we briefly introduce the time splitting scheme used for the time integration of Equations (2.1) and (2.2).[2] The integration from time, t, to a later time, $t+\delta t$, is done in three steps. Starting from step, p, through two intermediate steps, $p+\frac{1}{3}$ and $p+\frac{2}{3}$, the calculation is completed at the final step, $p+1$.

The first step is done explicitly in Fourier-Physical space using the 2-step Adams-Bashforth method. Only nonlinear convective terms are involued

$$\frac{\hat{\vec{v}}^{p+\frac{1}{3}} - \hat{\vec{v}}^{p}}{\delta t} = \frac{3}{2}\hat{\vec{G}}^{p} - \frac{1}{2}\hat{\vec{G}}^{p-1}, \tag{3.16}$$

where $\hat{\vec{G}}$ is the 2-dimensional Fourier transform of $\vec{G} = \vec{v} \times \vec{\omega} + \vec{F}$ given by (3.13). No boundary conditions are applied at this step.

The second step is the implicit pressure correction step

$$\vec{v}^{p+\frac{2}{3}} - \vec{v}^{p+\frac{1}{3}} = -\delta t \bigtriangledown \Pi^{p+\frac{2}{3}}, \tag{3.17}$$

[2]For more detailed description, the reader is referred to Orszag & Kells (1980)

$$\nabla^2 \hat{\hat{v}}^{p+\frac{2}{3}} = 0. \tag{3.18}$$

The boundary conditions applied at this step is the inviscid condition of no normal flow through the walls

$$w^{n+\frac{2}{3}}(x, y, \pm 1) = 0. \tag{3.19}$$

This is done in Fourier-Chebyshev space, so that (3.17), (3.18) and (3.19) become

$$\hat{\hat{u}}^{p+\frac{2}{3}}(\alpha, \beta, n) = \hat{\hat{u}}^{p+\frac{1}{3}}(\alpha, \beta, n) - i\alpha\delta t \hat{\hat{\Pi}}^{p+\frac{2}{3}}(\alpha, \beta, n), \tag{3.20}$$

$$\hat{\hat{v}}^{p+\frac{2}{3}}(\alpha, \beta, n) = \hat{\hat{v}}^{p+\frac{1}{3}}(\alpha, \beta, n) - i\beta\delta t \hat{\hat{\Pi}}^{p+\frac{2}{3}}(\alpha, \beta, n), \tag{3.21}$$

$$\hat{\hat{w}}^{p+\frac{2}{3}}(\alpha, \beta, n) = \hat{\hat{w}}^{p+\frac{1}{3}}(\alpha, \beta, n) - \delta t \hat{\hat{\Pi}}_1^{p+\frac{2}{3}}(\alpha, \beta, n), \tag{3.22}$$

$$i\alpha\hat{\hat{u}}^{p+\frac{2}{3}}(\alpha, \beta, n) + i\beta\hat{\hat{v}}^{p+\frac{2}{3}}(\alpha, \beta, n) + \hat{\hat{w}}_1^{p+\frac{2}{3}}(\alpha, \beta, n) = 0, \tag{3.23}$$

$$\sum_{n=0}^{\infty} \hat{\hat{w}}^{p+\frac{2}{3}}(\alpha, \beta, n) = 0, \tag{3.24}$$

$$\sum_{n=0}^{\infty} (-1)^p \hat{\hat{w}}^{p+\frac{2}{3}}(\alpha, \beta, n), = 0 \tag{3.25}$$

where $\hat{\hat{\Pi}}_1^{p+\frac{2}{3}}$ and $\hat{\hat{w}}_1^{p+\frac{2}{3}}$ are the Fourier-Chebyshev Transforms of the $\frac{d\Pi}{dz}$ and $\frac{dw}{dz}$ respectively.

Equations (3.20) to (3.25) can be re-organized and an equation is obtained for $\hat{\hat{w}}$ of the form,

$$C_{n-2}\hat{\hat{w}}_{n-2}^{p+\frac{2}{3}} - (1 + C_n)\hat{\hat{w}}_n^{p+\frac{2}{3}} C_{n+2}\hat{\hat{w}}_{n+2}^{p+\frac{2}{3}} = f_n, \tag{3.26}$$

where the $C_n's$ are positive real numbers dependent on α, β and n, and f_n is dependent on variables at fractional step, $p + \frac{1}{3}$, as well as α, β and n. This, together with boundary conditions (3.24) and (3.25), form two systems of equations for odd and even Chebyshev modes respectively. Total pressure Π^p and other velocity components can be easily obtained.

The final step is the implicit viscous correction step:

$$\frac{\vec{v}^{p+1} - \vec{v}^{p+\frac{2}{3}}}{\delta t} = \frac{1}{Re} \bigtriangledown^2 \vec{v}^{p+1}, \tag{3.27}$$

$$\vec{v}^{p+1}(x, y, \pm 1) = \vec{V}_{\pm}, \tag{3.28}$$

where $\vec{V}_{\pm}$ is the velocity at walls respectively. This step is evaluated in Fourier-Chebyshev space. Equation (3.27) can be written in the form of Equation (3.26).

The nonlinear term is obtained by evaluating the cross product, $\vec{G}^{p+1} = \vec{v}^{p+1} \times \vec{\omega}^{p+1}$, in physical space and then transformed into Fourier-Chebyshev space for use in the first fractional step, Equation (3.16)

This scheme has global error of the order $O(\delta t^2) + O(\frac{\delta t}{Re})$

Chapter 4

Modifications of the Flow Field

A turbulent spot modifies its surrounding flow field. In the experiment of Henningson & Alfredsson (1987), perturbations to the streamwise velocity are about 10 percent of the unperturbed centre-plane velocity in the channel and highly inflexional spanwise velocity profiles were also found around the turbulent spot.

This chapter examines the modifications of the mean flow created by a concentrated disturbance of the kind described in Chapter 2. We will pay special attention to the regions outside the modelled turbulent spot where the streamwise perturbation velocity is positive. These regions appear in the contour plots in (x, y) plane as two sets of nearly circular curves on either side of the modelled turbulent spot. As will be shown later, these are responsible for the destabilization of plane Poiseuille flow.

4.1 General patterns of flow around the disturbance

We recall that, in Chapter 2, the turbulent spot is modelled as a steady Gaussian distribution of Reynolds stress in a frame of reference travelling with speed c_s. Constants c_1 and c_2 represent the strengths of its symmetric and antisymmetric distributions

in the normal (z) direction, respectively. The ensemble averaged turbulent spot is symmetric with respect to the channel centre-plane in the sense that it creates symmetric u-perturbations in the flow field. We shall now examine the response of the flow field to symmetric forcing travelling with the speed $c_s = 0.8$. We use 64×64 Fourier modes in the x- and y- directions and 33 Chebyshev modes in the z- direction, respectively. The computational domain is 40×30 in the (x, y) - plane. The coordinate system travels with the modelled spot.

At time, $t = 0$, the symmetric forcing is switched on, and the flow is allowed to develop. The forcing strength used is small, $c_1 = 0.00001$, in order that the perturbed flow field is linear. The Reynolds number used is 1000. Figure 4.1 shows the contour plots of the u-perturbation velocity at $t = 10$ in aframe of reference travelling at the same speed as the forcing ($c_s = 0.8$). Contour values of u-perturbation plotted start from -0.000005, in increments of 0.000002. In the channel centre-plane, $z = 0$, the perturbation is negative in the neighbourhood of the point, $(x, y) = (0, 0)$, where the forcing is centered. In the plane = 0.556, a positive perturbation is seen around $(0, 0)$. This is an indication that the modelled Reynolds stress smears out the velocity gradients in the z-direction by slowing down the fast flow in the centre-plane and speeding up the slow flow closer to the walls.

At $t = 30$, there is one region of positive perturbation on each side of the modelled spot, much like that found by Henningson (1989). The u-velocity field looks typically like those shown in Figure 4.2, for time $t = 30$. The contour values plotted start at

-5 $\times$ 10^{-5}, with increments of 2 $\times$ 10^{-5}. These perturbation patterns are of relatively large scale (10 to 20 times the channel half-depth).

Now we look at the effect of stronger symmetric forcing on the flow field. The symmetric forcing strength is set at, $c_1 = 0.05$ (5000 time larger than the value used in the linear case). The forcing speed is $c_s = 0.8$, the same as in the linear case, and $Re = 1000$. Figure 4.3 shows the contour plots of u-perturbation velocity in planes, $z = 0$ and $z = 0.556$, at $t = 30$. The contour values start from -0.025, in increments of 0.01. The comparison between Figure 4.2 and Figure 4.3 shows that the patterns of the u-perturbation field are very similar in the two cases. The regions with positive u-perturbation velocity on both sides of $(x, y) = (0, 0)$ are clearly seen. At larger time, t, the basic patterns shown in Figure 4.3 remains approximately the same, but the perturbation velocity becomes larger.

The fact that strong forcing does not greatly alter the perturbation patterns is an indication that a linear analysis may be employed to study flow field outside the turbulent spot for moderately large t.

4.2 Flow fields forced at different speeds

A real turbulent spot grows in size as it travels downstream. The front of a spot travels at approximately 0.75-0.85, and its rear travels at approximately 0.6-0.5, in a range of Reynolds numbers, Re = 1000–3000 (see, Henningson *et al.* (1987)). In the

present formulation, the modelled turbulent spot can be made to travel at different speeds c_s. Four cases are presented: (i) $c_s = 0.95$, (ii) $c_s = 0.8$, (iii) $c_s = 0.7$ and (iv) $c_s = 0.6$ with $Re = 1000$ and the symmetric forcing strength $c_1 = 0.05$ in all cases. The coodinate system travels with the modelled spot with speed c_s in respective cases.

We look at the flow patterns in two planes parallel to the channel walls — one is the centre-plane ($z = 0$) and the other is a plane between the channel centre and the walls ($z = 0.556$). We are interested mainly in two properties of the perturbation flow field at different forcing speeds – (i) the amplitudes of u-perturbation velocities and (ii) the positions at which the regions of positive u-perturbation velocity appear, since these are the regions where the growth and breakdown of waves are found (see Henningson *et al* (1987)).

Figure 4.4 shows the contour plots of the u-perturbation velocity at the channel centre-plane, $z = 0$, at time, $t = 45$. The contour values plotted are ± 0.005, ± 0.015 and ± 0.025 in each of the contour plots in Figure 4.4. The forcing is made to travel at $c_s = 0.95$, $c_s = 0.8$, $c_s = 0.7$ and $c_s = 0.6$ in respective cases. The flow patterns look similar in all four cases — a region of negative perturbation is found around $(x, y) = (0, 0)$, where the modelled spot is located, because the increased Reynolds stress slows down the flow. One region of positive perturbation is found away from $(x, y) = (0, 0)$ on each side. The positive perturbation amplitude is largest for $c_s = 0.95$, and is notably smaller for $c_s = 0.8$, $c_s = 0.7$ and $c_s = 0.6$.

Thus, it is found that, in the channel centre-plane, $z = 0$, the amplitude of positive u-perturbation velocity on each side of the modelled spot increases when the speed, c_s, of the forcing increases.

By inspection of Figure 4.4 (a), (b), (c) and (d), we find that the regions of positive perturbations appear at different streamwise locations for different forcing speeds. At time $t = 45$, they are located at roughly $x = 0$, $x = 5$, $x = 7.5$ and $x = 12$ for $c_s = 0.95$, $c_s = 0.8$, $c_s = 0.7$ and $c_s = 0.6$, respectively. At some later time, these regions remain roughly where they are for $c_s = 0.95$, $c_s = 0.8$ and $c_s = 0.7$, but not for $c_s = 0.6$. For $c_s = 0.6$, the region of positive perturbation actually travels downstream and moves out of the computational domain, and, at the same time, the amplitude decays. This may be best explained with the ship-wave analogy. When a ship moves steadily on the water-surface, the only wave modes that can keep up with the ship and appear steady in the co-ordinate system fixed to the ship are those whose phase velocities in the direction of the ship motion are equal to the velocity of the ship. It is a little more complicated in the present case of the modelled steady "spot". The perturbations created by the spot will eventually settle to a steady state (at least in the linear case) since the "spot" is assumed to be constant with respect to time. If we assume that the perturbations consist of some free modes yet to be specified, then the only modes that can be found around the "spot" in steady state are those with the phase speed equal to the speed of the "spot" c_s. There is also an additional effect in the case of the steady "spot". If the free modes making up the velocity perturbations have complex dispersion relations, the least damped modes (assumming all free modes are damped) will attain large amplitudes following the initial excitation by the "spot". If these modes have

phase speeds much larger than c_s, they will travel out of the "zone of influence" of the "spot". The fact that, at $c_s = 0.6$, the regions of positive perturbations evetually move away from the "spot" is an indication that these regions are associated with some fast free modes.

We now look at the plane, $z = 0.556$, between the channel centre and the walls. The amplitude of the perturbation is smallest for $c_s = 0.95$ and larger for $c_s = 0.8$, $c_s = 0.7$ and $c_s = 0.6$. Therefore, if the forcing is slow moving, the amplitude of the positive perturbation is large, in contrast to what happens in the channel centre-plane ($z = 0$). The regions of positive perturbations appear roughly at streamwise positions $x = -3$, $x = 0$, $x = 3$ and $x = 4$ for $c_s = 0.95$, $c_s = 0.8$, $c_s = 0.7$ and $c_s = 0.6$ respectively. These regions remain roughly where they are for $c_s = 0.8$ and $c_s = 0.6$ at some later time, but are left behind and decay for $c_s = 0.95$. This is again in contrast to what happens in the channel centre-plane. This indicates that the regions of positive perturbations are associated with some slow free modes. When it is slow moving, the forcing continuously causes these slow modes to grow, whereas when it is fast moving, it leaves these modes behind to decay.

The differences in speeds and locations of the modified flow regions in the planes $z = 0$ and $z = 0.556$ suggest that the perturbation to the mean flow consists of two types of modes – (i) a fast type that has maximum amplitudes at the channel centre-plane and (ii) a slower type that has maximum amplitudes near the walls.

We can also look at the distribution of spanwise velocity, v, across the channel depth in the regions of positive u-perturbation (Figure 4.6). We chose a spanwise position, $y = 4.22$, which approximately corresponds to the y-position of the region of maximum positive streamwise perturbation, and plot the spanwise velocity v as a function of z at 5 different streamwise positions ($x = 0$, $x = 1.25$, $x = 2.5$, $x = 3.75$ and $x = 5$), at $t = 35$. Highly inflexional profiles can be seen. The profiles with large amplitudes near the centre-plane, $z = 0$, for $c_s = 0.8$ shown in Figure 4.6 (a) very much resemble those obtained by Henningson *et al.* (1987) and Henningson (1989). The profiles for $c_s = 0.6$ (Figure 4.6 (b)) resemble those for $c_s = 0.8$ near the walls, but lack the large amplitudes near the centre. For even slower forcing speed, the spanwise velocity profiles remain inflexional near the walls, but all have smaller amplitudes near the centre-plane, $z = 0$. The numerical results for the cross channel profiles of the streamwise velocity do not show noticable inflexion.

Having examined the perturbation patterns in the two (x, y) –planes , $z = 0$ and $z = 0.556$, we may conclude the following:

- The perturbations found by using a modelled turbulent spot show similar features to existing experiments and numerical simulations. On either side of the modelled spot, there is a region of positive $u-$perturbation.
- The spanwise velocity profiles are inflexional.
- The regions of positive u-perturbations on each side of a turbulent spot may consist of several kinds of free modes — some fast-moving modes and some slow moving

modes

- The amplitudes of the fast-moving modes are largest near the centre of the channel ($z = 0$).
- The amplitudes of the slow-moving modes are largest away from the centre of the channel ($z \neq 0$)

In order to check the effect of increasing Reynolds number on the flow field, another case is run with $Re = 2000$, $c_s = 0.7$, and $c_1 = 0.05$. The flow patterns are the same as those for $Re = 1000$. In fact, no noticeable difference can be shown in the contour plots of streamwise perturbation velocities. Even at, $t = 60$, the differences are small. The insensitivity of the flow field to increasing the Reynolds number may be due to the fact that the perturbations are of such large scale that viscosity plays a relatively small role even at Reynolds numbers of the order 1000.

In the next chapter we will analyze the linear modes which contribute to the velocity perturbations by considering the eigenfunctions of the normal vorticity equation.

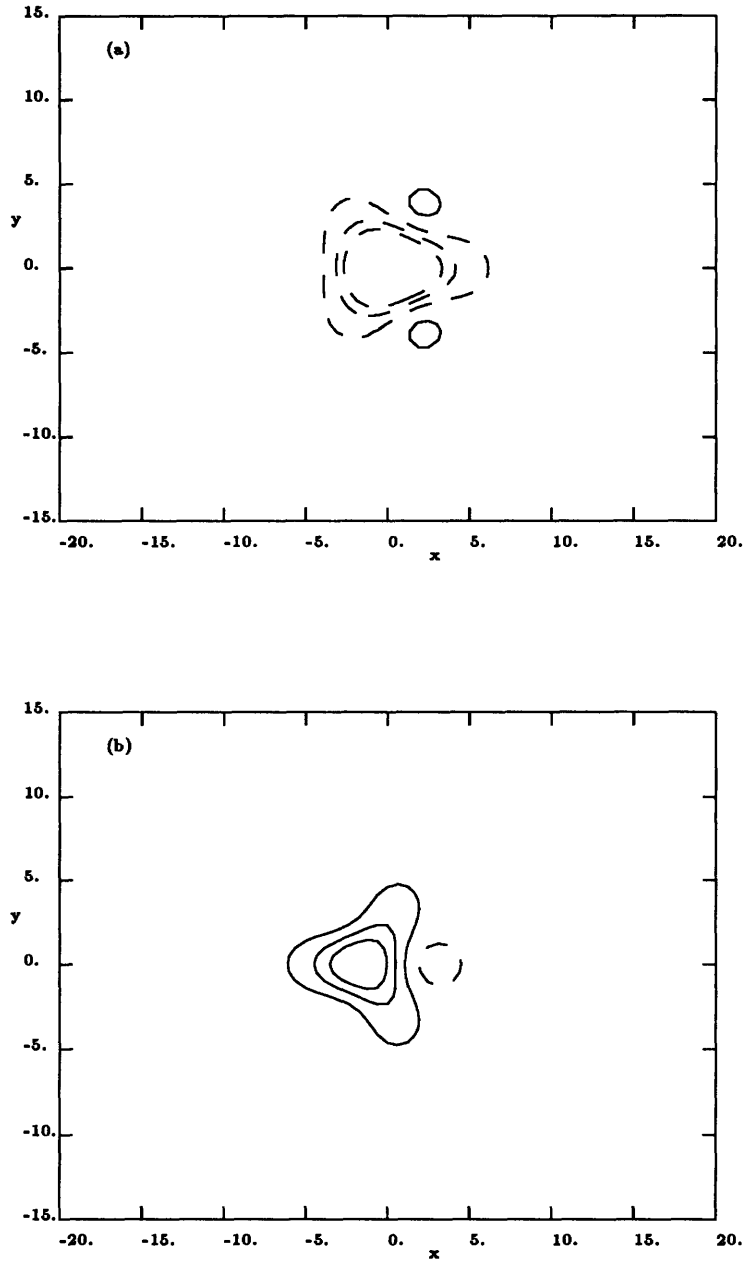

Figure 4.1: Contours u-perturbation velocity. $Re = 1000$, $c_s = 0.8$, $c_1 = 1 \times 10^{-5}$, $t = 10$. Contour values start from -5×10^{-6}, increment 2×10^{-6}. ——positive, - - - - negative. (a) $z = 0$ and (b) $z = 0.556$

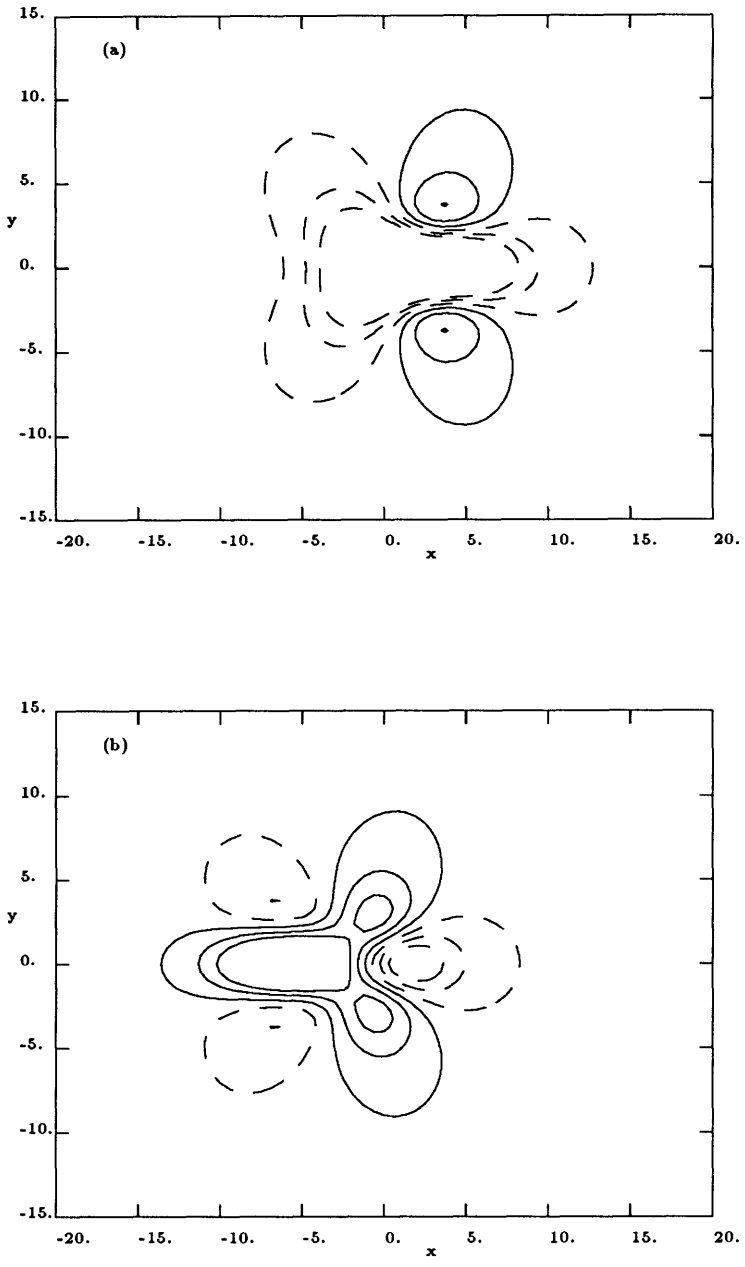

Figure 4.2: Contours of u-perturbation. $Re = 1000$, $c_s = 0.8$, $c_1 = 1 \times 10^{-5}$, $t = 30$. Contour values start from -5×10^{-6}, increment=2×10^{-6}. (a) $z = 0$ and (b) $z = 0.556$.

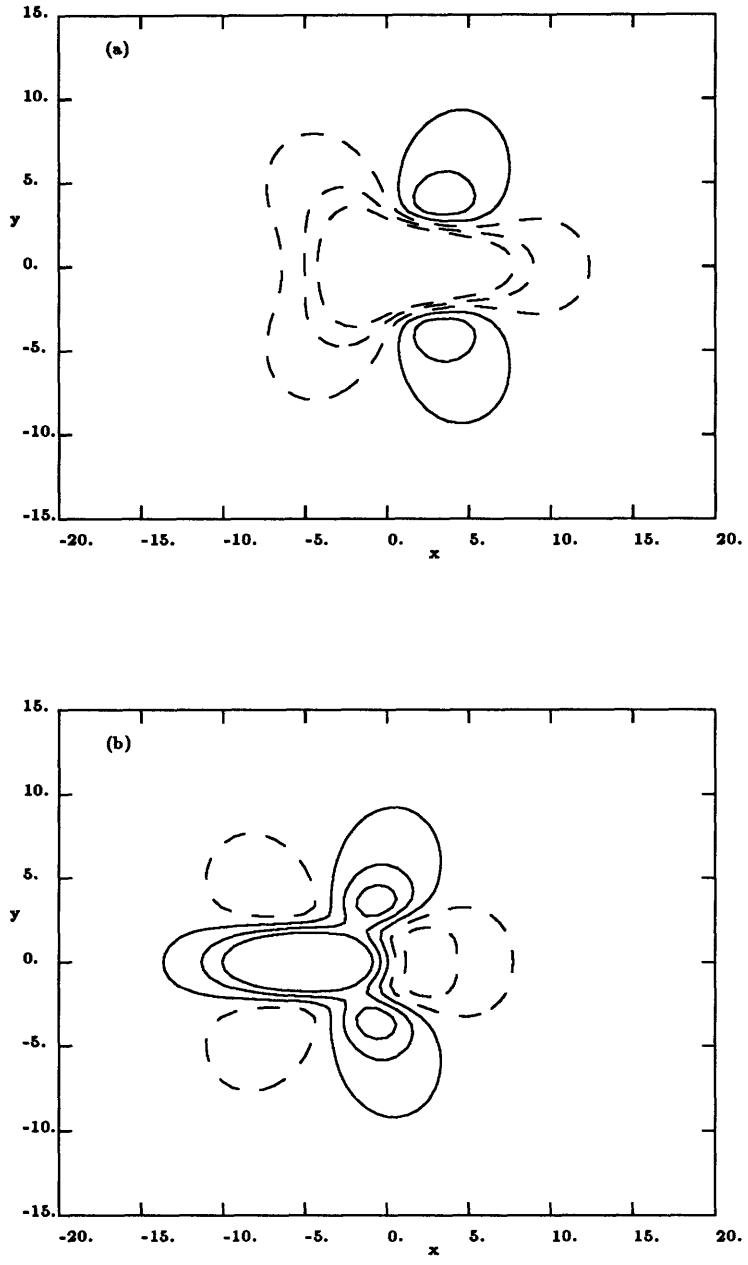

Figure 4.3: Contour u-perturbation velocity. $Re = 1000$, $c_s = 0.8$, $c_1 = 0.05$, and $t = 30$. Contour values start from -0.025, increment 0.01. —— positive, - - - - negative. (a)$z = 0$ and (b)$z = 0.556$.

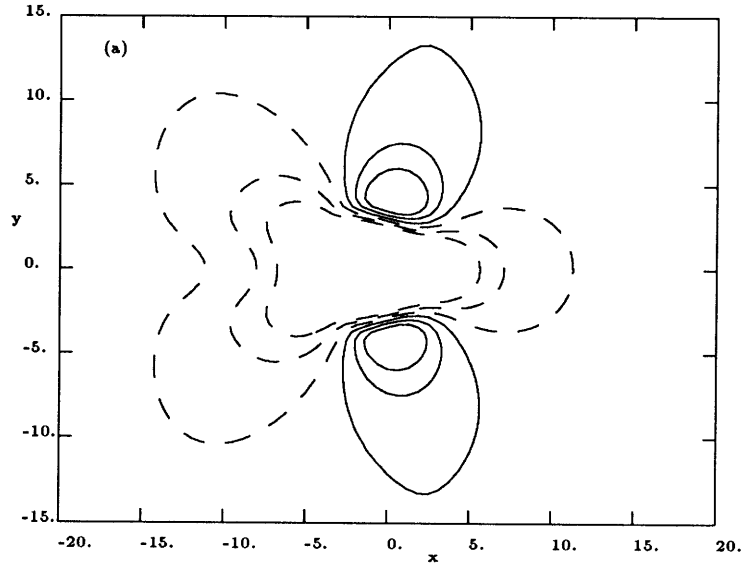

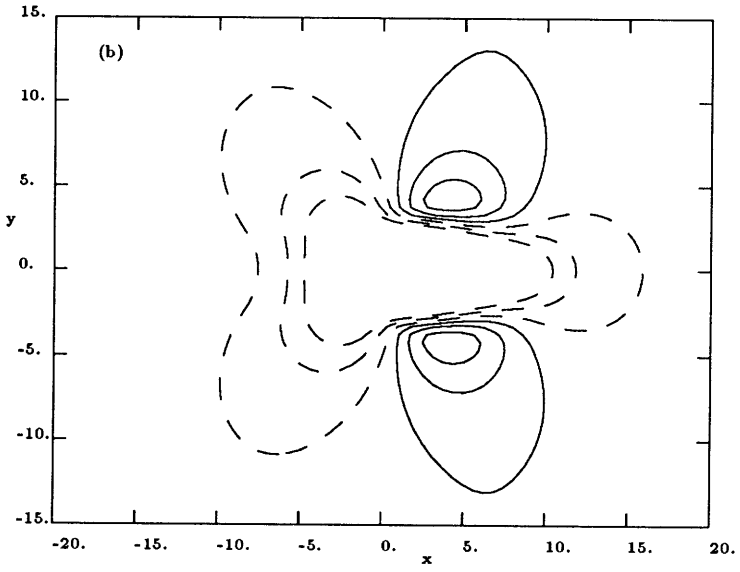

See next page for captions.

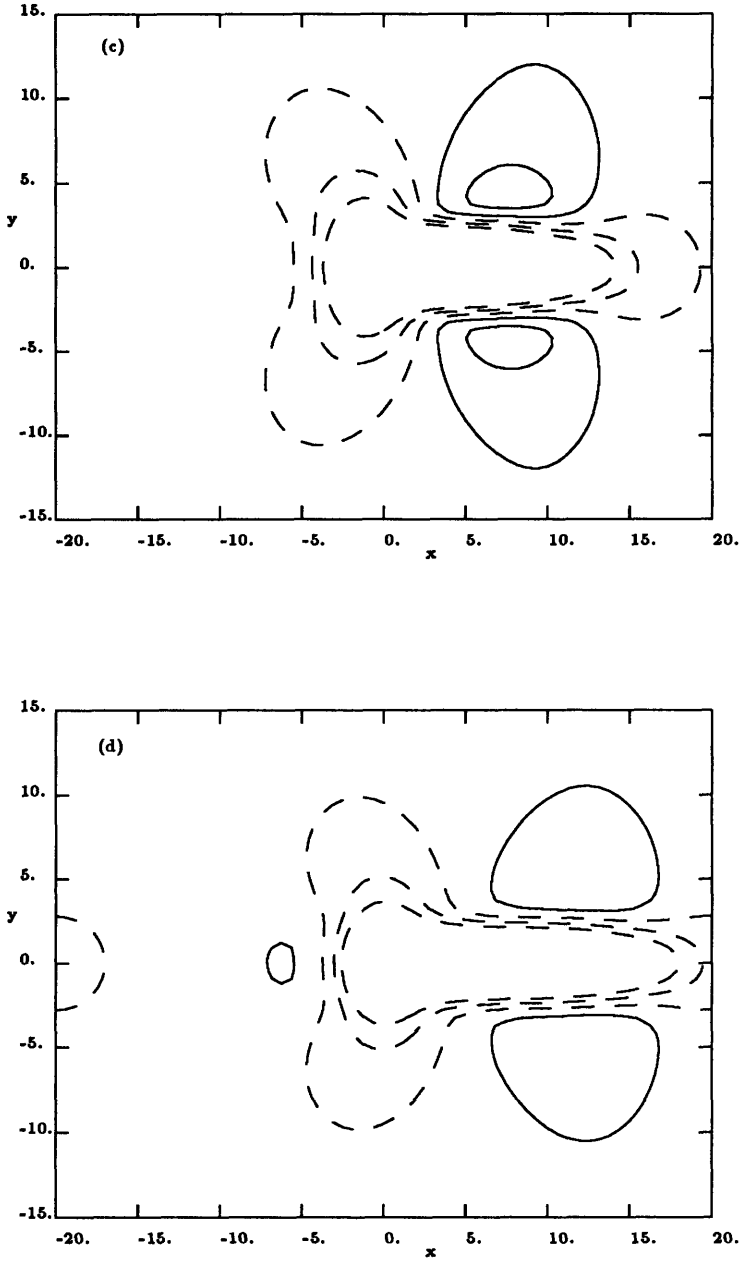

Figure 4.4: Contours u-perturbation velocity.$Re = 1000$, $c_1 = 0.05$, $t = 45$. Contour values start from -0.025, increment 0.01, $z = 0$ ——positive, - - - - negative. (a) $c_s = 0.95$, (b) $c_s = 0.8$, (c) $c_s = 0.7$ (d) $c_s = 0.6$

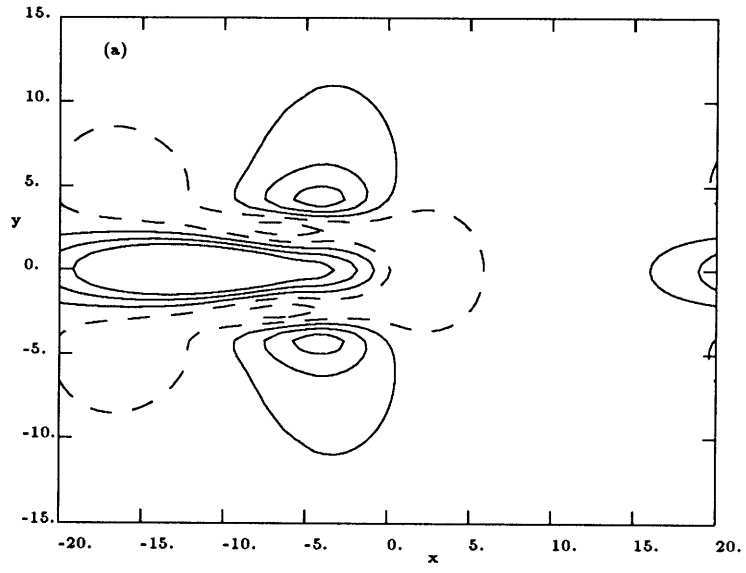

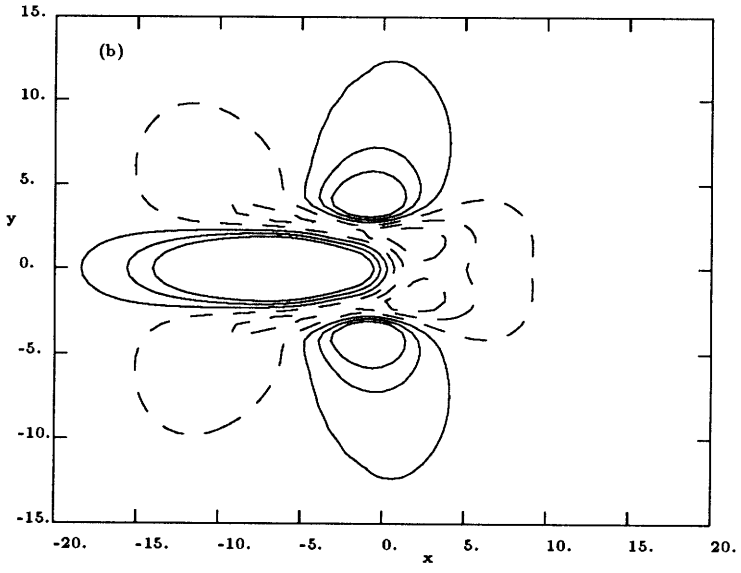

See next page for caption.

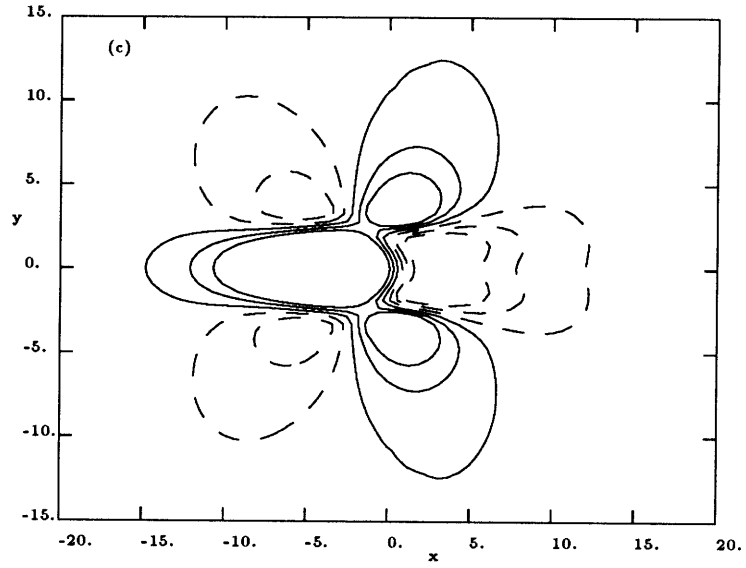

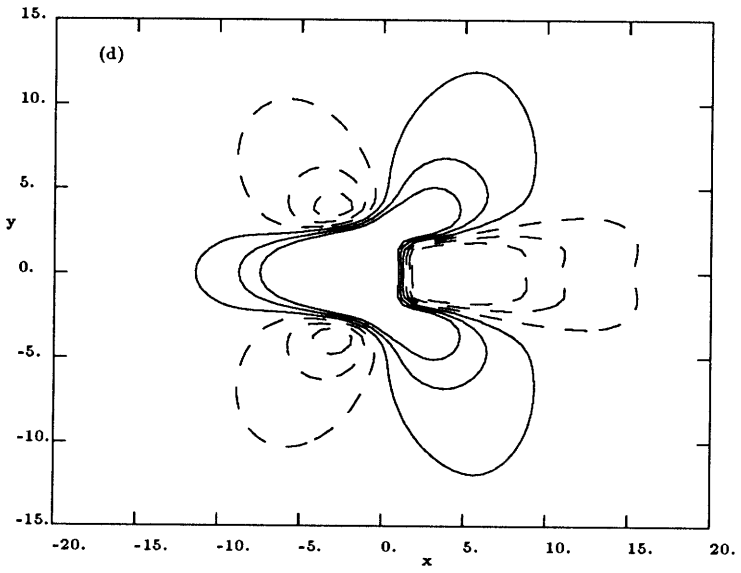

Figure 4.5: Contours u-perturbation velocity.$Re = 1000$, $c_1 = 0.05$, $t = 45$. Contour values start from -0.025, increment 0.01, $z = 0.556$ ——positive, - - - - negative. (a) $c_s = 0.95$, (b) $c_s = 0.8$, (c) $c_s = 0.7$, (d) $c_s = 0.6$

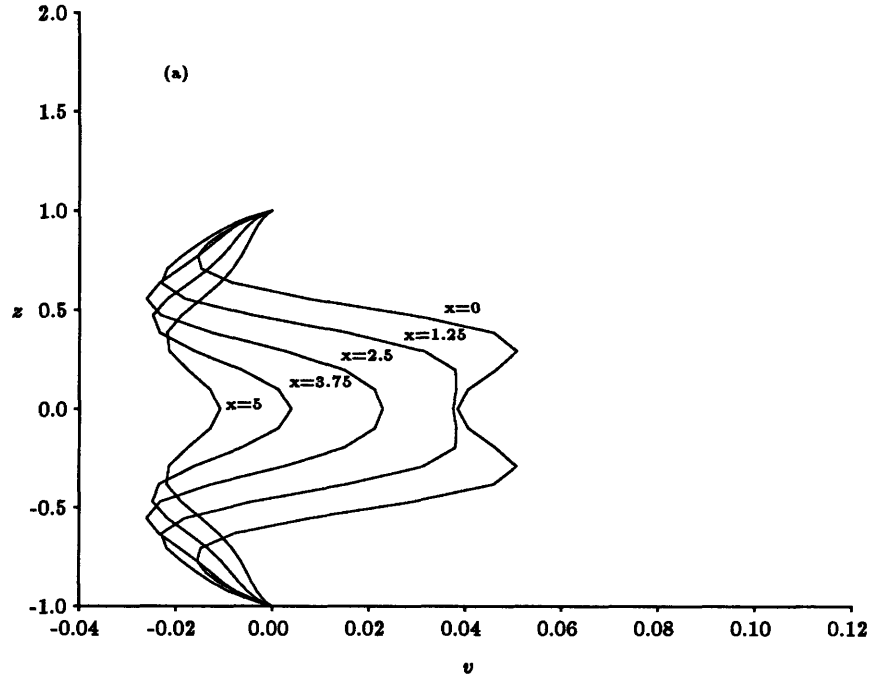

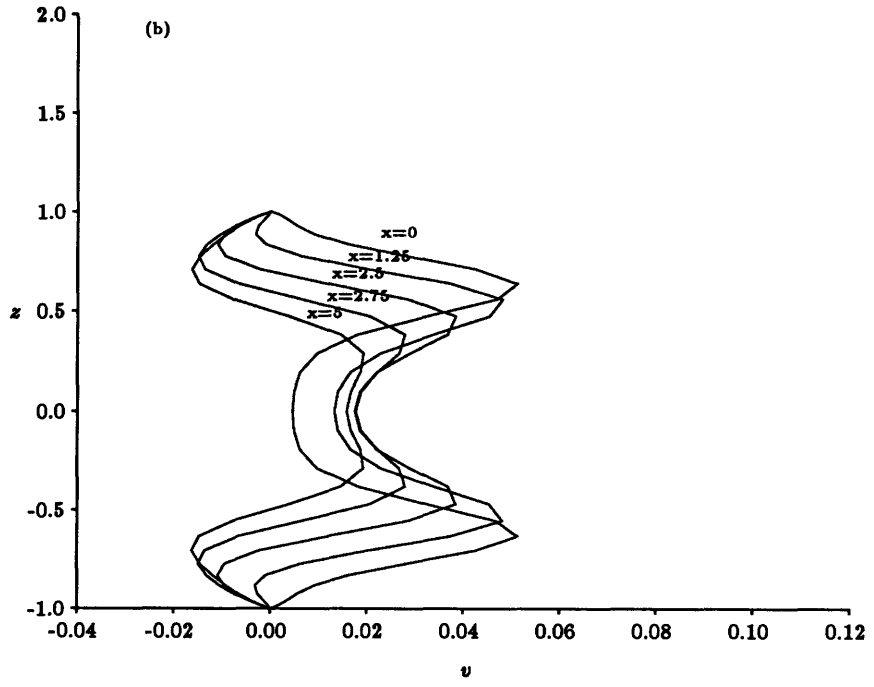

Figure 4.6: v profiles at $t = 35$, $y = 4.22$. (a) $c_s = 0.8$ and (b) $c_s = 0.6$

Chapter 5

Origins of the modified flow field

In this capter, we will discuss the eigenfunction decompositions of the streamwise and spanwise velocities. We will not attempt to find all the eigenmodes to describe the flow field modifications exactly, but rather to analyze the first few eigenmodes that contribute the most to the flow field modifications.

5.1 Eigenvalue problem of the normal vorticity equation

If we linearize the Reynolds averaged Navier-Stokes equations (2.1) around the unperturbed plane Poiseuille flow $U(z) = 1 - z^2$, the following equations are obtained by eliminating the presure p from the momentum equations:

$$\frac{\partial}{\partial t} \nabla^2 w + U \frac{\partial}{\partial x} (\nabla^2 w) - \frac{1}{Re} \nabla^4 w - \frac{d^2 U}{dz^2} \frac{\partial w}{\partial x} = \frac{\partial^3 \overline{u'w'}}{\partial x \partial z^2}, \tag{5.1}$$

$$\frac{\partial \omega_3}{\partial t} + U(z) \frac{\partial \omega_3}{\partial x} - \frac{1}{Re} \nabla^2 \omega_3 = \frac{\partial w}{\partial y} U'(z) + \frac{\partial^2 \overline{u'w'}}{\partial y \partial z}, \tag{5.2}$$

where $\omega_3 = \frac{\partial v}{\partial x} - \frac{\partial u}{\partial y}$ is the normal component of vorticity and $\overline{u'w'}$ is the only Reynolds stress term retained. The boundary conditions are

$$w(x, y, \pm 1, t) = \frac{\partial w}{\partial z}(x, y, \pm 1, t) = 0, \tag{5.3}$$

$$\omega_3(x, y, \pm 1) = 0. \tag{5.4}$$

These equations completely describe the linear perturbation flow field. The second equation is the normal vorticity equation which governs the perturbations in the xy-plane. We will discuss the eigenfunctions of Equation (5.2) with zero right hand side and later use these functions to express the u and v velocity perturbations.

We use the normal mode analysis in (5.2) by letting $\omega_3 = \Phi(z)\exp[i(\alpha x+\beta y-\alpha ct)]$ and set the right hand side of (5.2) to zero to obtain the following eigenvalue problem:

$$(D^2 - k^2)\Phi - i\alpha Re(U - c)\Phi = 0, \tag{5.5}$$

$$\Phi(\pm 1) = 0, \tag{5.6}$$

where $k^2 = \alpha^2 + \beta^2$, α and β are real wave numbers, $D = d/dz$ and c is the complex eigenvalue. Equation (5.5) with boundary conditions (5.6) for plane Poiseuille flow was analyzed by Gustavsson (1981). Since solutions to this equation are important in understanding the modifications of the flow field, we will analyze it in some detail.

Following Davey & Reid (1977), we multiply Equation (5.5) by Φ^*, the complex conjugate of Φ, integrate with respect to z from $z = -1$ to $z = 1$ and normalize the solution so that $\int_{-1}^{1} \mid \Phi \mid^2 dz = 1$. We obtain the following,

$$c = c_r + ic_i = \int_{-1}^{1} U \mid \Phi \mid^2 dz - \frac{i}{\alpha Re}(\int_{-1}^{1} \mid D\Phi \mid^2 dz + k^2). \tag{5.7}$$

Hence, we find the $U_{min} < c_r < U_{max}$ and $c_i < 0$. In plane Poiseuille flow with $U(z) = 1 - z^2$, we have, $0 < c_r < 1$.

Equation (5.5) is a regular ordinary differential equation, therefore its solutions are entire functions of not only z, but also of the parameters α, β and Re. For convenience, we make the following transformations

$$R = -iRe, \tag{5.8}$$

$$c' = c - \frac{k^2}{i\alpha Re} = c + \frac{k^2}{\alpha R}, \tag{5.9}$$

$$\lambda = -\alpha R c'. \tag{5.10}$$

Equation (5.5) becomes

$$D^2\Phi + (\alpha R U(z) + \lambda)\Phi = 0. \tag{5.11}$$

Since β is absorbed into λ, Equation (5.11) shows that the eigenfunction, Φ, is independent of β.

Suppose R is real (*i.e*, we have an imaginary Reynolds number), Equation (5.11) subject to boundary conditions (5.6) is a Sturm-Liouville boundary value problem. We state the following mathematical theorem useful for the purpose of this section. (For proof see Hartman (1982), page 337).

Theorem I:

There exist a countable set of real numbers $\lambda_0 < \lambda_1 < .... < \lambda_n ....$ such that,

(i) Equation (5.11) subject to boundary conditions (5.6) has a nontrivial solution if and only if $\lambda = \lambda_n$ for some n;

(ii) If $\lambda = \lambda_n$, the corresponding nontrivial solution, $\Phi_n(z)$, is unique up to a multiplicative constant, and $\Phi_n(z)$ has exactly n zeros on the open interval $(-1, 1)$.

(iii) If $n \neq m$ then

$$\int_{-1}^{1} \Phi_n \Phi_m dz = 0;$$

(iv) If $\lambda \neq \lambda_n$ there exist a unique solution, $\psi(z)$ to the following equation

$$D^2\psi + (\alpha RU(z) + \lambda)\psi = h(z)$$

with boundary condition $\psi(\pm 1) = 0$;

(v) If $\lambda = \lambda_n$, then the above equation has a solution if and only if

$$\int_{-1}^{1} \Phi_n(z) h(z) dz = 0$$

(vi) $\Phi_0(z)$, $\Phi_1(z)$, ... , $\Phi_n(z)$, ... form a complete orthonormal basis for functions that are square-integrable in the close interval [-1,1].

The eigenvalues and eigenfunctions are entire functions of the parameter, R, therefore, Theorem I can be generalized to include complex R. The statements about the ordering of the eigenvalues and the zeros of the eigenfunctions would have to be modified since the λ_n's and Φ_n's are now complex numbers and functions, respectively.

Let us now find λ_n and the corresponding $\Phi_n(z)$ when n is large. We expand $\Phi_n(z)$ and λ_n in powers of $1/\lambda'$, where λ' is some large number approximately equal to λ_n, so

that we have

$$\Phi_n(z) = \phi^{(0)}(z) + \frac{1}{\lambda'}\phi^{(1)}(z) + O(\frac{1}{\lambda'^2}), \tag{5.12}$$

$$\lambda_n = \lambda' + \bar{c} + O(\frac{1}{\lambda'}), \tag{5.13}$$

where $1/\lambda' \ll \bar{c} \ll \lambda'$. By substituting Equations (5.12) and (5.13) into Equation (5.11) and balance the terms, we get,

$$D^2\phi^{(0)} + \lambda'\phi^{(0)} = 0, \tag{5.14}$$

with boundary conditions $\phi^{(0)}(\pm 1) = 0$ and

$$D^2\phi^{(1)} + \lambda'\phi^{(1)} = -\lambda'(\alpha RU(z) + \bar{c})\phi^{(0)}, \tag{5.15}$$

with boundary conditions $\phi^{(1)}(\pm 1) = 0$.

We only deal with solutions that are even about $z = 0$ (odd solutions can be obtained in similar ways). The solution to Equation (5.14) is $\phi^{(0)} = \cos((\lambda')^{\frac{1}{2}}z)$, with $\lambda' = \pi^2 n^2/4$ (n = 1, 3, 5, ...) in order that the boundary conditions are satisfied. A first approximation to λ_n is thus found. n must be large for the solution to be asymptotically valid.

We proceed to find λ_n to the next order. We observe that the λ' on the left hand side of Equation (5.15) is an eigenvalue of the corresponding homogeneous equation, therefore, the solvability condition in Theorem I (iv) requires

$$\int_{-1}^{1}(\alpha RU(z) + \bar{c})(\phi^{(0)})^2 dz = 0$$

We know that $\phi^{(0)}(z) = \cos((\lambda')^{\frac{1}{2}}z)$. Integration by parts of the above expression gives

$$\int_{-1}^{1}(\alpha R(1-z^2)+\overline{c})dz + O(\frac{1}{\lambda'}) = 0.$$

Hence we obtain $\overline{c} = -\frac{2}{3}\alpha R + O(\frac{1}{\lambda'})$. Combining the first and second approximations to the large eigenvalues and using Equations (5.8), (5.9) and (5.10), we obtain the n'th eigenvalue of Equation (5.5)

$$c_n = \frac{2}{3} - i\frac{\pi^2 n^2 + 4k^2}{4\alpha Re} + O(\frac{1}{n^2}), \tag{5.16}$$

where n is odd. The eigenfunctions obtained this way have the correct oscillating behaviour, but the phase angles are incorrect. This is due to the fact that the phase difference between the real and the imaginary parts of the eigenfunctions is small for large λ'.

For small n's, Equation (5.16) is not valid. Numerical methods must be used to find the small eigenvalues. The Tau-spectral-integration method is used to solve the eigenvalue problem associated with Equation (5.5).

Figure 5.1 show the eigenvalues, c, in the complex c-plane for $Re = 1000$, $\alpha = 0.3$ and $\beta = 0$. The eigenfunction for $\beta \neq 0$ is the same provided α is fixed as explained earlier. The symbols s and a indicate even and odd mode respectively. We can see that eigenvalues with large imaginary parts lie on a line $c_r = \frac{2}{3}$ as shown in Equation (5.16). We analyze only the even modes. Modes $s1$ is a fast mode and Mode $s2$ (indistinguishable from $a2$ [1]) is slow, while Mode $s3$ is somewhere in between. The

[1]The solution is not degenerate since two eigenfunctions are found for this eigenvalue – one is even and the other is odd

eigenmodes alternate from even to odd down the line $c_r = 2/3$. Figure 5.2 show the eigenfunctions of these three modes over half the channel from $z = 0$ to $z = 1$. The eigenvalues are functions of parameters αRe and $k^2 = \alpha^2 + \beta^2$, and the eigenfunctions are functions of the parameter αRe only (see Gustavsson, 1981). We choose to show these three modes at $\alpha = 0.3$ just to demonstrate the qualitative properties of these eigenfunctions.

- Mode $s1$ has eigenvalue $c = 0.959 - i0.041$. The eigenfunction of Mode $s1$ has maximum modulus at the centre-line of the channel and monotonically decreases as z increases.

- Mode $s2$ has eigenvalue $c = 0.460 - i0.238$. The eigenfunction of Mode $s2$ has maximum modulus near the wall, its real and imaginary parts oscillate as z increases.

- Mode $s3$ has eigenvalue $c = 0.796 - i0.203$. The modulus of the eigenfunction has its maximum between the channel centre, $z = 0$, and the wall, $z = 1$. and its real and imaginary parts cross 0 once in interval $(0, 1)$.

For wavenumbers different from $\alpha = 0.3$, the eigenvalue spectrum is similar to Figure 5.1. As α is reduced, the positions of Modes s1, a1, s3 and a3 move down along the line joining these modes, while modes s2 and a2 move toward their lower right. If α is increased, the opposite occurs.

5.2 Eigenmodes contributing to flow field modifications

We linearize the Navier-Stokes equations about the unperturbed plane Poiseuille flow and let u, v, w and p be the perturbation quantities. We write the Fourier-transformed linearized equations in the following form to facilitate the analysis:

$$\frac{\partial}{\partial t}(D^2-k^2)\hat{w}+i\alpha[U(D^2-k^2)-\frac{d^2U}{dz^2}]\hat{w}-\frac{1}{Re}(D^2-k^2)^2\hat{w}=i\alpha\frac{\partial^2\widehat{u'w'}}{\partial z^2}, \tag{5.17}$$

$$D^2\hat{p}-k^2\hat{p}=-2i\alpha\hat{w}\frac{dU}{dz}-i\alpha\frac{\partial\widehat{u'w'}}{\partial z}, \tag{5.18}$$

$$\frac{\partial\hat{u}}{\partial t}+i\alpha U\hat{u}-\frac{1}{Re}(D^2-k^2)\hat{u}=-i\alpha\hat{p}-\hat{w}\frac{dU}{dz}-\frac{\partial\widehat{u'w'}}{\partial z}, \tag{5.19}$$

$$\frac{\partial\hat{v}}{\partial t}+i\alpha U\hat{v}-\frac{1}{Re}(D^2-k^2)\hat{v}=-i\beta\hat{p}, \tag{5.20}$$

where $D=\partial/\partial z$ and $\hat{u}$ is the Fourier transform of u, *etc.* The left hand side differential operators in Equations (5.19) and (5.20) are the same as that of the normal vorticity equation (5.2) in Fourier-space. This fact enables us to express solutions to $\hat{u}$ and $\hat{v}$ in terms of the eigenfunctions of the normal vorticity equation.

The boundary conditions at the walls become:

$$\hat{u}(\alpha,\beta,\pm1,t)=\hat{v}(\alpha,\beta,\pm1,t)=\hat{w}(\alpha,\beta,\pm1,t)=0, \tag{5.21}$$

$$\frac{\partial\hat{w}}{\partial z}(\alpha,\beta,\pm1,t)=0, \tag{5.22}$$

$$\frac{\partial\hat{p}}{\partial z}(\alpha,\beta,\pm1,t)=\frac{1}{Re}\frac{\partial^2\hat{w}(\alpha,\beta,\pm1,t)}{\partial z^2}. \tag{5.23}$$

We note that Equations (5.17) and (5.18) are uncoupled with Equations (5.19) and (5.20). Therefore, we can first solve for w and p before using the solutions as known driving terms on the right hand side of Equations (5.19) and (5.20).

In Equation (5.18), the differential operator, $D^2 - k^2$, is independent of time and the right hand side has two parts – (i) a time-dependent part $-2i\alpha\hat{w}U'(z)$ and (ii) a time-independent part $-i\alpha\partial(\widehat{u'w'})/\partial z$. Because of linearity we can write $\hat{p}$ as the sum of $\hat{p}_1$ and $\hat{p}_2$ which represent time-independent and time-dependent solutions respectively:

$$\hat{p} = \hat{p}_1 + \hat{p}_2. \tag{5.24}$$

The boundary conditions on $\hat{p}_1$ and $\hat{p}_2$ are, respectively,

$$\frac{\partial \hat{p}_1}{\partial z}(\alpha, \beta, \pm 1, t) = 0, \tag{5.25}$$

$$\frac{\partial \hat{p}_2}{\partial z}(\alpha, \beta, \pm 1, t) = \frac{1}{Re}\frac{\partial^2 \hat{w}(\alpha, \beta, \pm 1, t)}{\partial z^2}. \tag{5.26}$$

Henningson (1991) solved an linear initial value problem in plane Poiseuille flow by expanding the normal velocity in eigenfunctions of the Orr-Sommerfeld equation and the normal vorticity in eigenfunctions of the normal vorticity equation. Here we are interested in the eigenfunction compositions of u and v, hence we will apply eigenfunction expansions to u and v only. Supposing we have already solved Equations (5.17) and (5.18) so that the right hand sides of Equations (5.19) and (5.20) are now known functions, we can proceed to solve $\hat{u}$ and $\hat{v}$. The eigenfunction expansions for $\hat{u}$ and $\hat{v}$

are given below,

$$\hat{u} = \sum_{j=0}^{\infty} A_j \Phi_j, \tag{5.27}$$

$$\hat{v} = \sum_{j=0}^{\infty} B_j \Phi_j, \tag{5.28}$$

where Φ_j is the jth eigenfunction of Equation (5.5), which are normalized so that $\int_{-1}^{1} \Phi_j^2 dz = 1$.

By substituting Equations (5.27) and (5.28) into Equations (5.19) and (5.20), and making use of the orthogonality relation of Theorem I (iii), we obtain:

$$\frac{dA_j}{dt} + i\alpha(c_j - c_s)A_j = Q_j + q_j, \tag{5.29}$$

$$\frac{dB_j}{dt} + i\alpha(c_j - c_s)B_j = R_j + r_j, \tag{5.30}$$

where c_j is the j'th eigenvalue and Φ_j is the corresponding eigenfunction. Q_j, q_j, R_j and r_j are given, respectively, by the following:

$$Q_j = \int_{-1}^{1} \Phi_j(z)(-i\alpha\hat{p}_1 - \frac{\partial \widehat{u'w'}}{\partial z})dz, \tag{5.31}$$

$$q_j = \int_{-1}^{1} \Phi_j(z)(-i\alpha\hat{p}_2 - \hat{w}U'(z))dz, \tag{5.32}$$

$$R_j = \int_{-1}^{1} \Phi_j(z)(-i\beta\hat{p}_1)dz, \tag{5.33}$$

$$r_j = \int_{-1}^{1} \Phi_j(z)(-i\beta\hat{p}_2)dz. \tag{5.34}$$

It is clear from Equations (5.31) to (5.34) that Q_j and R_j are time-independent, and q_j and r_j are time-dependent.

We assume that there is no disturbance initially, the modelled forcing is switched on at time, $t = 0$, and the flow is allowed to develop. Equations (5.29) and (5.30) are first

order ordinary differential equations with constant coefficients, whose solutions can be easily obtained. They are, respectively,

$$A_j = \frac{Q_j(1 - e^{-i\alpha(c_j - c_s)t})}{i\alpha(c_j - c_s)} + e^{-i\alpha(c_j - c_s)t} \int_0^t q_j(\tau) e^{i\alpha(c_j - c_s)\tau} d\tau, \tag{5.35}$$

$$B_j = \frac{R_j(1 - e^{-i\alpha(c_j - c_s)t})}{i\alpha(c_j - c_s)} + e^{-i\alpha(c_j - c_s)t} \int_0^t r_j(\tau) e^{i\alpha(c_j - c_s)\tau} d\tau. \tag{5.36}$$

In order to evaluate the integrals in Equations (5.35) and (5.36), we need to calculate $q_j(\tau)$ and $r_j(\tau)$ for all values of $\tau \in [0, t]$. However, if t is large, the integrals can be approximated by replacing $q_j(\tau)$ and $r_j(\tau)$ with $q_j(t)$ and $r_j(t)$, respectively, so that the integrations can be done analytically. The errors caused in making these approximations decay faster than or equal to $O(te^{-at})$ for large time, where a is a positive constant [2]. The approximate expressions for A_j and B_j are, respectively,

$$A_j = \frac{Q_j + q_j(t)}{i\alpha(c_j - c_s)}(1 - e^{-i\alpha(c_j - c_s)t}), \tag{5.37}$$

$$B_j = \frac{R_j + r_j(t)}{i\alpha(c_j - c_s)}(1 - e^{-i\alpha(c_j - c_s)t}). \tag{5.38}$$

We solve for $\hat{w}$ and $\hat{p}$ with a 4th-order finite difference method, and then use Equations (5.31) to (5.34) to obtain $Q_j(\tau)$, $q_j(\tau)$, $R_j(\tau)$ and $r_j(\tau)$ at $\tau = t$. Equations (5.37) and (5.38) give A_j and B_j respectively. Once $A_j(\alpha, \beta)$ and $B_j(\alpha, \beta)$ are found for all values of (α, β), the inverse Fourier transforms will give the solutions to $u(x, y, z, t)$ and $v(x, y, z, t)$.

The streamwise perturbation velocity contours at $t = 35$ and $z = 0$ with $c_s = 0.8$ otained from the eigenfunction expansions are shown in Figure 5.3. The essential

[2]See Appendix for proof

features of perturbation is already captured with only one eigenmode, namely, the $s1$ mode. Adding the $s2$ and $s3$ modes to the $s1$ mode reduces the amplitudes of the perturbations in these region regions. The contour values plotted are the same as in Figure 4.4. It appears that the amplitude of the perturbation at $t = 35$ obtained with three eigenmodes is comparable to that obtained from running the Navier-Stokes code at $t = 45$ (Figure 4.4 (b)), indicating an over-prediction of the perturbation amplitude. There may be two main reasons for this over-prediction. Firstly, $t = 35$ may be too small for the approximations made in Equations (5.37) and (5.38) to hold. Secondly, the non-orthogonality of the normal vorticity modes could lead to an over-prediction of the energy in the flow if the number of modes used is insufficient. The latter of these will be discussed in the next section.

The spanwise perturbation velocity profiles are shown in Figure 5.4. Using the s1 mode only, we find that the spanwise perturbation velocity away from the walls are captured and other modes are needed to account for the perturbations near the walls. With two eigenmodes, $s1$ and $s3$, the inflexional features of the v profiles are captured. The velocity profiles look similar to those shown in Figure 4.6. The addition of the $s3$ mode, however, makes the profiles close to the walls oscillatory, but does not significantly change the profiles near the centre-plane of the channel. By adding the $s4$, $s5$ and $s6$ modes, we find that the oscillation amplitude near the walls becomes consecutively smaller.

5.3 Energy in the spanwise modes

Henningson (1989) showed that the "cross-flow" instability due to the inflexional spanwise profiles is responsible for the exponential growth of waves outside the turbulent spot. In this section, we will analyze the energy contribution to the spanwise perturbation due the the first few normal vorticity modes. The kinetic energy in the spanwise velocity is given by,

$$E = \frac{1}{2}\int_{-\infty}^{\infty}\int_{-\infty}^{\infty}\int_{-1}^{1} \mid \hat{v}(\alpha,\beta,z) \mid^2 dzd\alpha d\beta. \tag{5.39}$$

By substituting Equation (5.28) into (5.39), we obtain the following:

$$E = \sum_{m=1}^{\infty}\sum_{n=1}^{\infty} E_{mn}, \tag{5.40}$$

where

$$E_{mn} = \frac{1}{2}\int_{-\infty}^{\infty}\int_{-\infty}^{\infty}\int_{-1}^{1} B_m(\alpha,\beta)B_n^*(\alpha,\beta)\Phi_m(\alpha,\beta,z)\Phi_n^*(\alpha,\beta,z)dzd\alpha d\beta. \tag{5.41}$$

The integration of (5.41) is done by Simpson's rule and the numerical value of the energy component, E_{mn}, is listed in Table 5.1 for the first six modes of the normal vorticity equation. These modes are not orthogonal, *i.e.* $\int_{-1}^{1}\Phi_m(z)\Phi_n^*(z) \neq 0$ for $m \neq n$, hence $E_{mn} \neq 0$. Since $E_{mn} = E_{nm}^*$, resulting in cancellations of the imaginary parts in the summation (5.40), only the real parts of the E'_{mn}s are shown in Table 5.1. E_{mn} is normalized so that $E_{11} = 1$. From Table 5.1, we can get an idea of the relative importance of these modes. The energy associated with mode $s6$ (*i.e.* summing the last row and the last column of Table 5.1) is small (-0.003). We may assume that the sum of the numbers in Table 5.1 is a rough estimate of the total energy in v, $E = 2.117$. If

-	$s1$	$s3$	$s2$	$s4$	$s5$	$s6$
$s1$	1	0.258	-0.094	-0.016	-0.005	-0.002
$s3$	0.258	0.510	-0.180	0.078	-0.033	-0.007
$s2$	-0.094	-0.180	0.441	-0.032	0.012	-0.012
$s4$	-0.016	0.078	-0.032	0.260	-0.074	0.018
$s5$	-0.005	-0.033	0.012	-0.074	0.067	-0.013
$s6$	-0.002	-0.007	-0.012	0.018	-0.013	0.041

Table 5.1: Energy component, E_{mn}, due to normal vorticity modes sm and sn in the spanwise velocity for the first four modes. The energy components are normalized so that E_{11} is unity.

we use only two modes to represent v, namely the $s1$ and $s3$ modes, the energy due to these modes is, $E' = E_{11} + E_{22} + E_{12} + E_{21}$. From Table 5.1, we find that $E' = 2.026$, which is 96% of the total energy. As more modes are included in the summation(5.40), E' as a percentage of E may change slightly. However, $s1$ and $s3$ modes will still have major contributions to the spanwise velocity perturbation. It should be noted that the addition of modes $s5$ and $s6$ reduces E from 2.239 to 2.117. Therefore, if only 4 modes were used, the total energy would be over-predicted.

As we see in Figure 4.2, the length scale of the perturbations is about 20, which translates to a wave number of about 0.3 in Fourier space. The eigenvalues along $c_r = \frac{2}{3}$

shown in Figure 5.1 are large, and so $\frac{1}{i\alpha(c_j-c_s)}$ is small. For the $s5$ mode, the "exact" (numerical) eigenvalue is, $c = 0.67137 - i0.63643$, and the asymptotic approximation (5.16) gives $c = 0.66667 - i0.66650$. The error of the approximation is about 5%. Further down the line $c_r = 2/3$ the error is even smaller. The magnitude of $\frac{1}{c_j-c_s}$ for the sm mode should be of order $(2m-1)^{-2}$ according to (5.16). Hence, for large m, the sm mode does not contribute significantly to A_j and B_j given by (5.37) and (5.38). Major contributions come from modes having small imaginary parts. The three representative modes, $s1$, $s2$ and $s3$ at $\alpha = 0.3$, have eigenvalues $0.959 - i0.041$, $0.460 - i0.238$ and $0.796 - i0.203$, respectively. If we let the modelled turbulent spot travel at a speed equal to the real part of one of these eigenvalues, *i.e* c_s =Real(c_j), then the denominator in Equations (5.37) and (5.38), $\frac{1}{c_j-c_s}$, is smallest and we have a large contribution from this mode.

Now, we may speculate why the turbulent spot front travels at a speed of about 0.6 to 0.8 as shown by the experiments and numerical simulations (Henningson, *et al* 1987 and Henningson 1989). The waves in the destabilized regions grow and break down into small scale turbulence which makes the spot larger. This, in turn, destabilizes more regions in the flow and the cyclic process continues. Suppose the spot front travels at the phase speed of mode $s3$ (0.796), then the highly inflexional velocity profiles of mode s3 and other slower modes are large in the perturbed regions of the flow field. Certain waves are unstable in this region and their growth will keep the growth-breakdown process going. If, instead, the spot travels at an increased speed, say, the phase speed of mode $s1$ (0.959), then mode $s1$ will dominate the perturbed flow field and the perturbed velocity profiles may not be as unstable as before. Even though the perturbation may be

large (since mode $s1$ has the smallest imaginary part), the flow field is perturbed, but not destabilized. The growth-breakdown process cannot be maintained. The turbulent spot, therefore, has to travel at some speed lower than the phase speed of mode $s1$. The above hypothesis is supported by the the results of Chapter 5.

It is important to mention that all eigenmodes of the normal vorticity equation are stable modes, *i.e.* $\mathrm{Im}(c_j) < 0$. Without the Reynolds stress forcing, any small initial perturbation to the streamwise and spanwise velocities will eventually decay. The turbulent spot forces these modes to grow to large amplitudes and hence modifies the flow field.

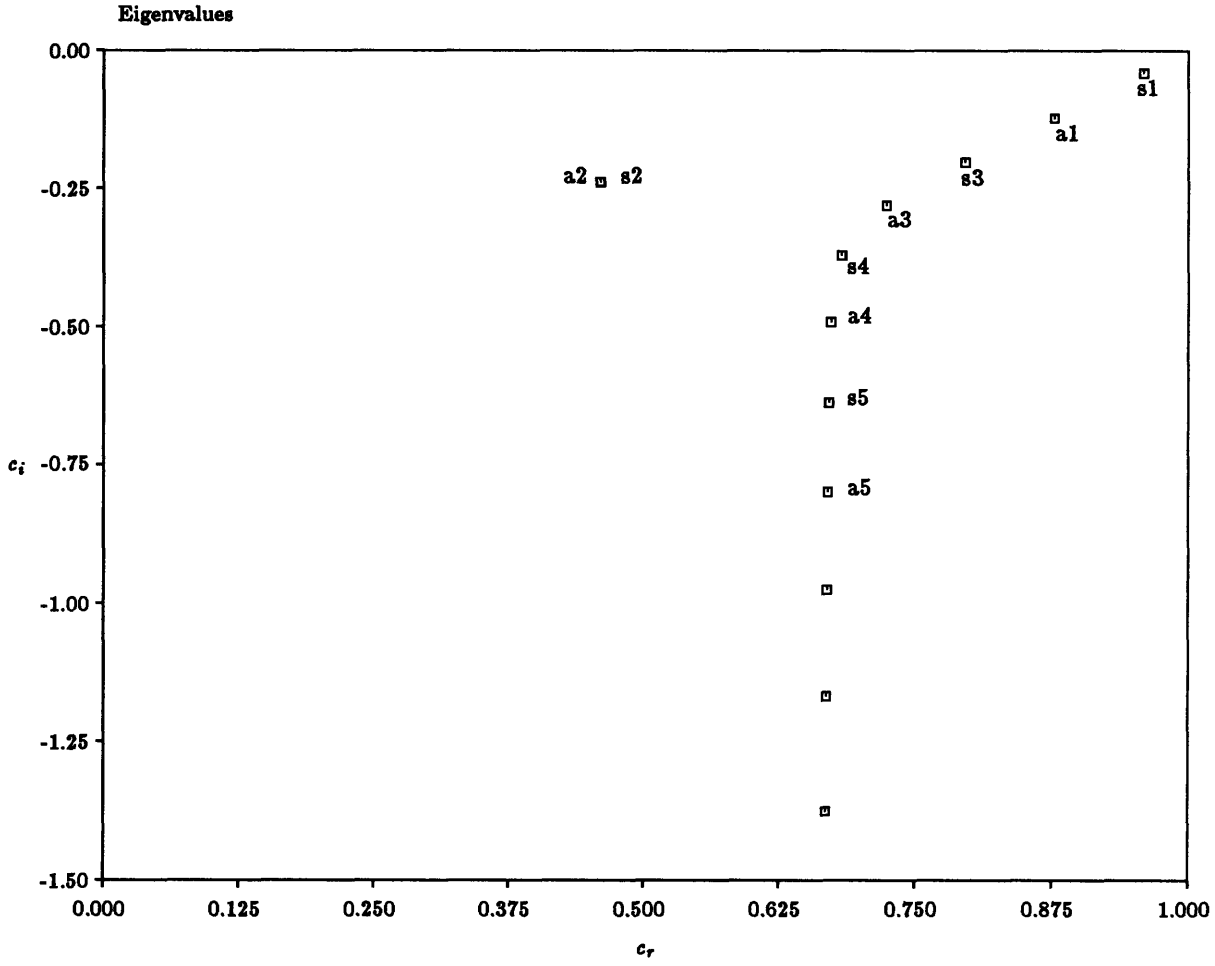

Figure 5.1: Eigenvaules of the normal vorticity equation. $Re = 1000$, $\alpha = 0.3$, $\beta = 0$.

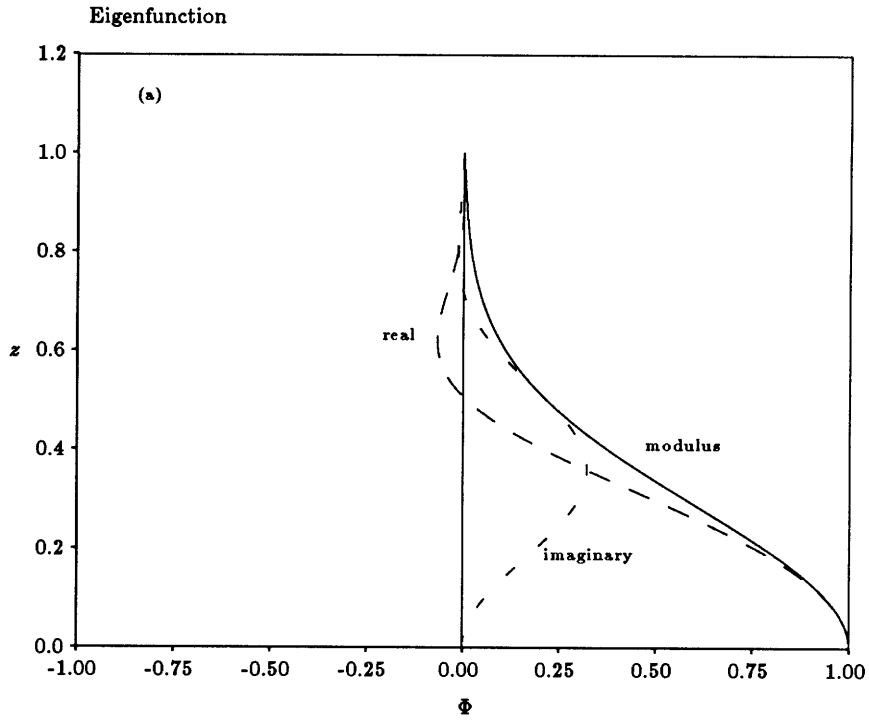

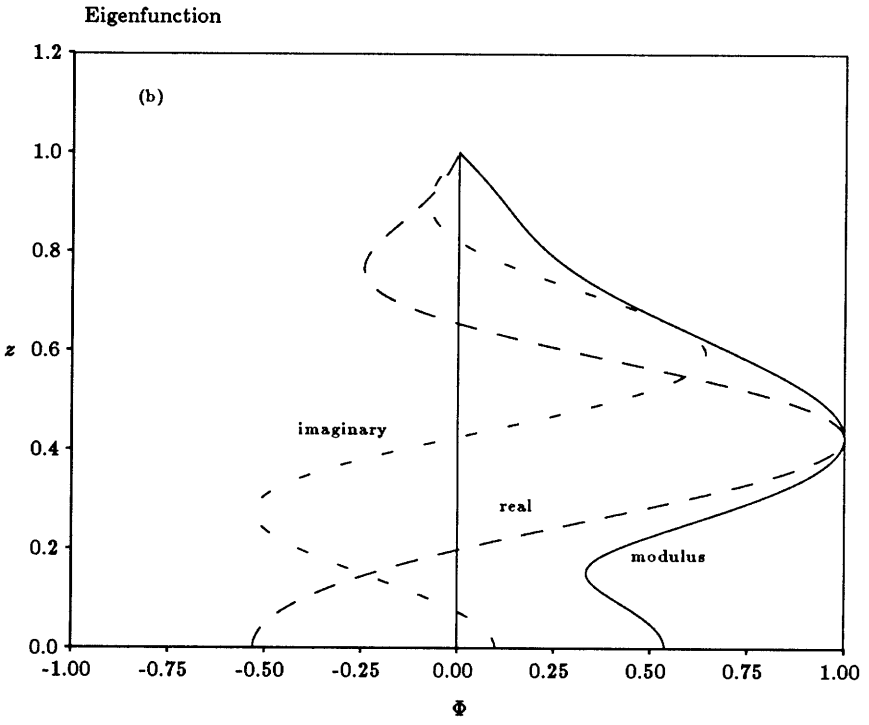

see next page for caption

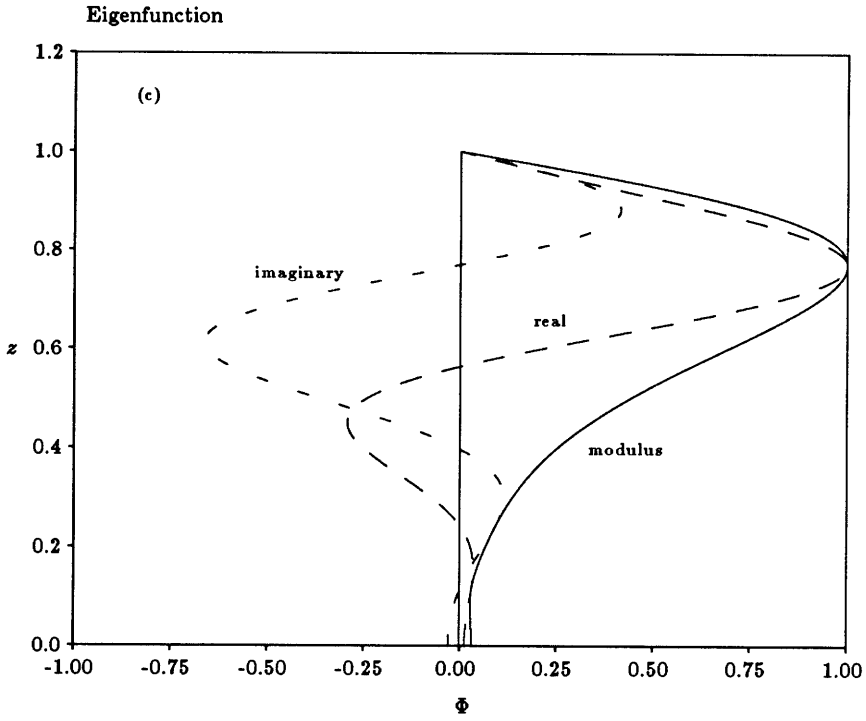

Figure 5.2: Eigenfunctions of the normal vorticity equation. (a) Mode $s1$, $c = 0.959 - i0.041$, (b) Mode $s3$, $c = 0.796 - i0.203$, (c) Mode $s2$, $c = 0.460 - i0.238$. Mode $s1$ is concentrated around channel centre, $z = 0$, whereas Modes $s3$ and $s2$ near the walls, $z = 1$

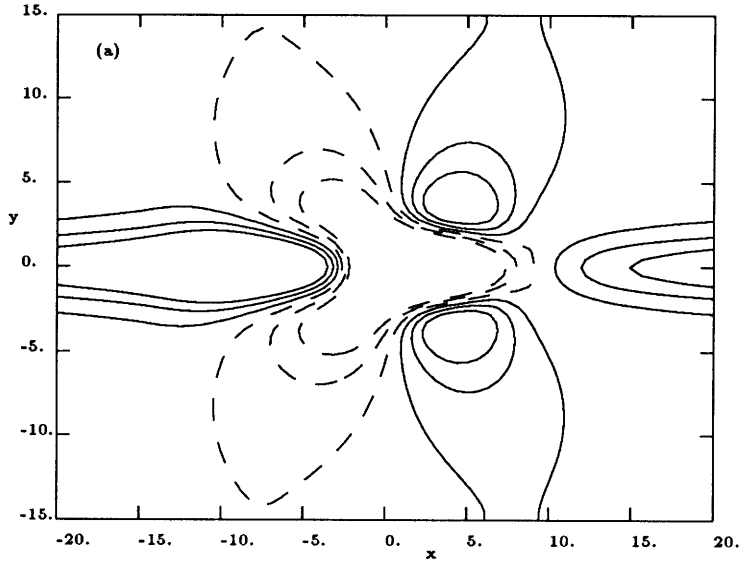

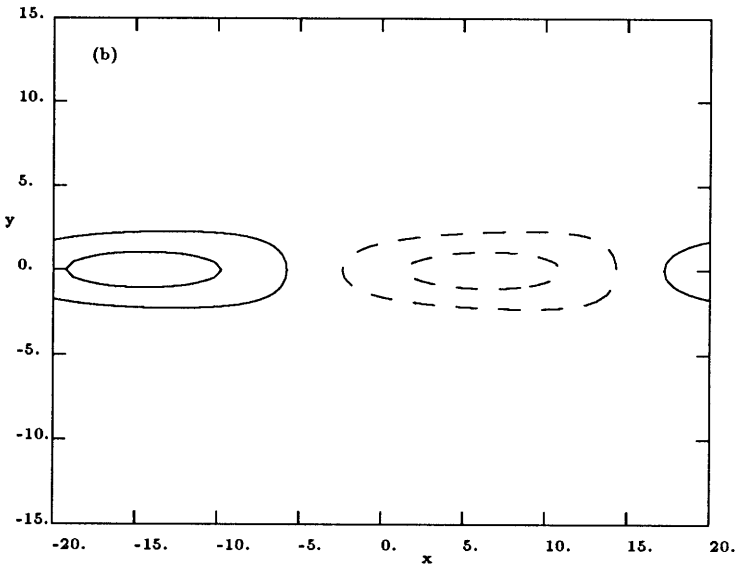

See next page for caption.

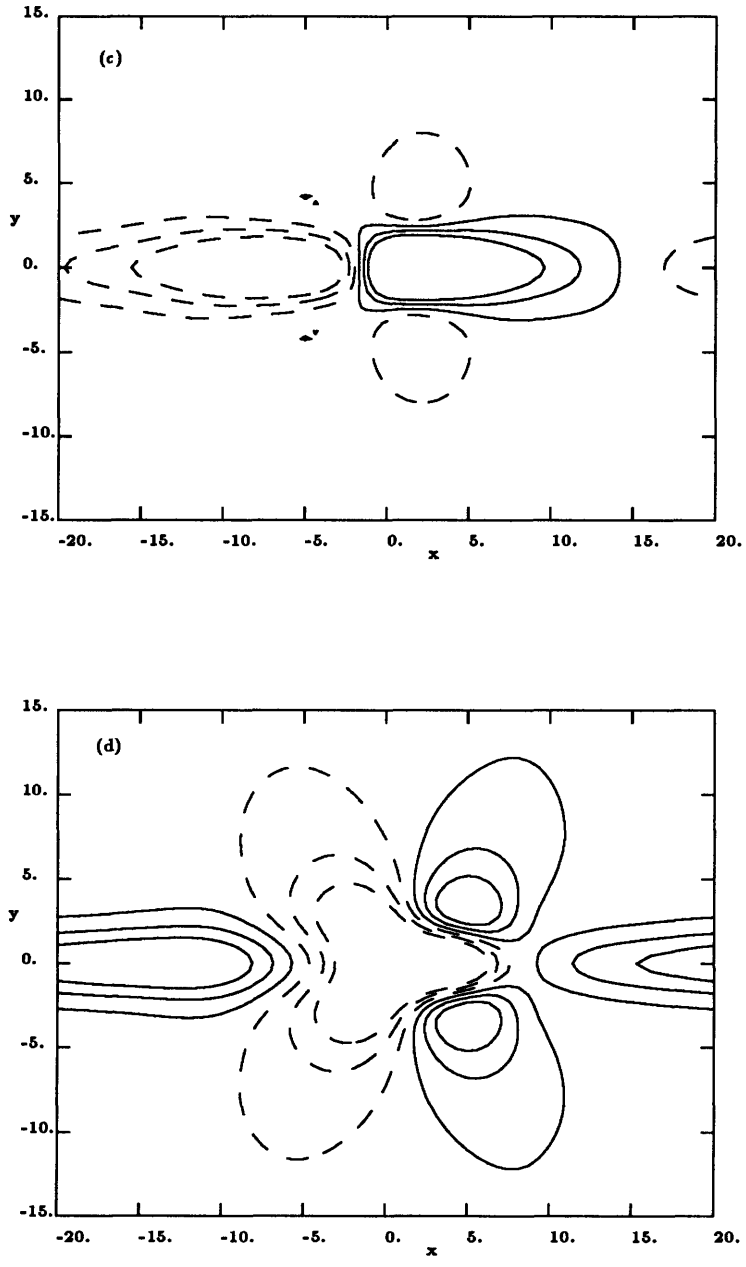

Figure 5.3: u perturbation contours calculated from eigenfunctions. $Re = 1000$, $t = 45$, $c_s = 0.8$. Contours start from -0.025, increment 0.01, $z = 0$. (a) $s1$, (b) $s2$, (c)$s3$ and (d) $s1 + s2 + s3$

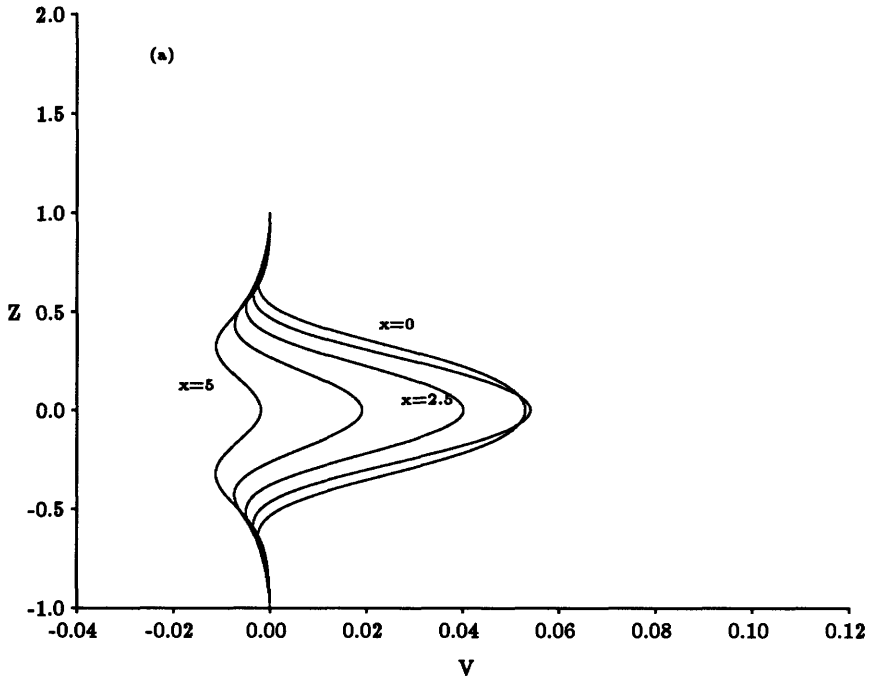

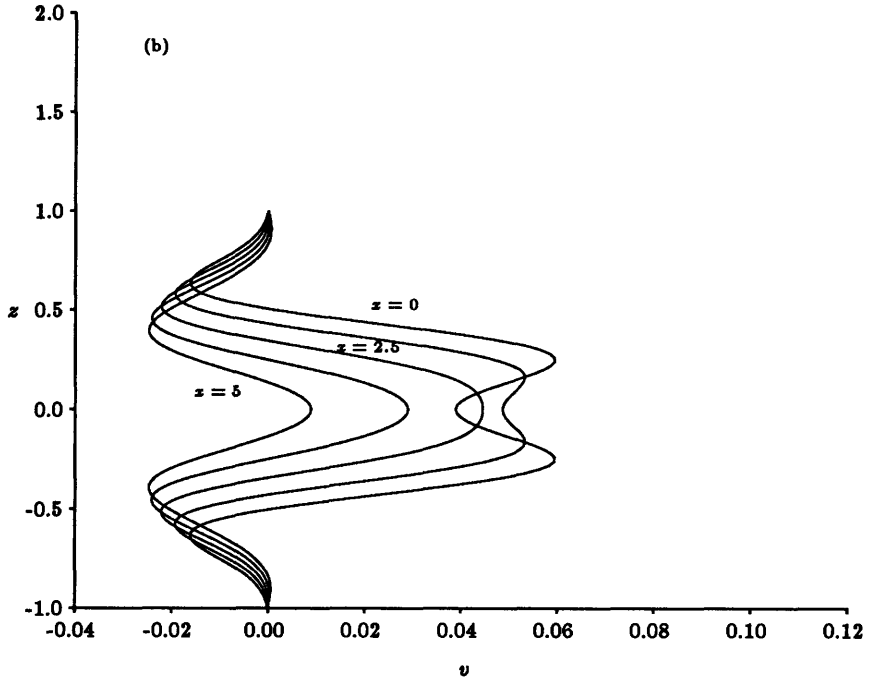

See next page for caption.

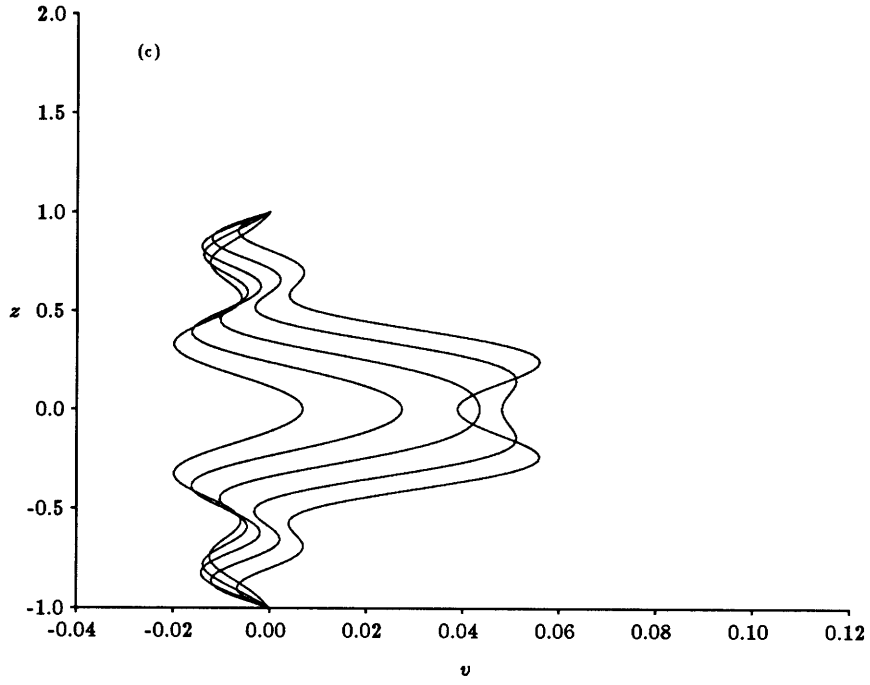

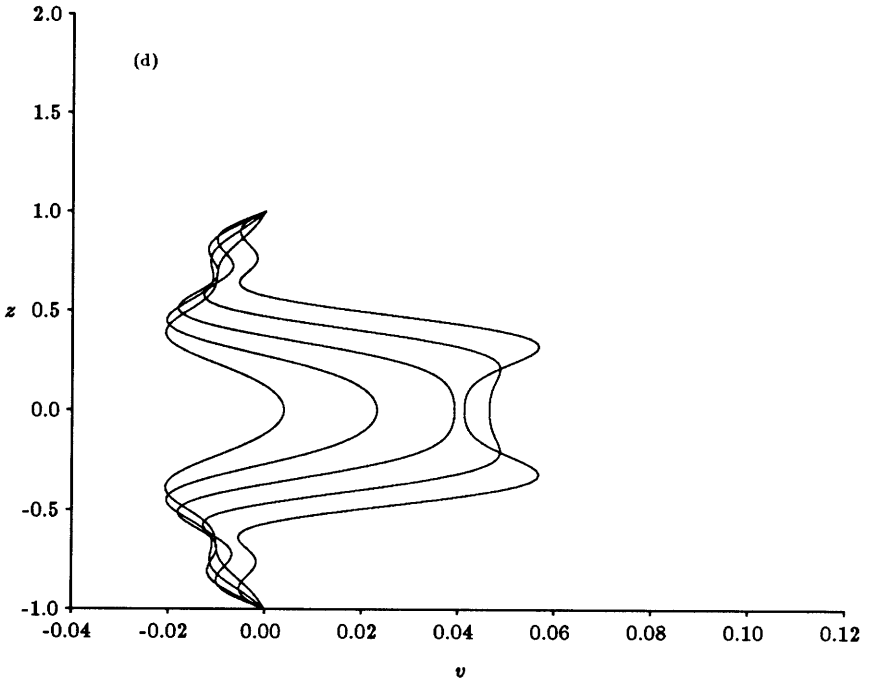

See next page for caption

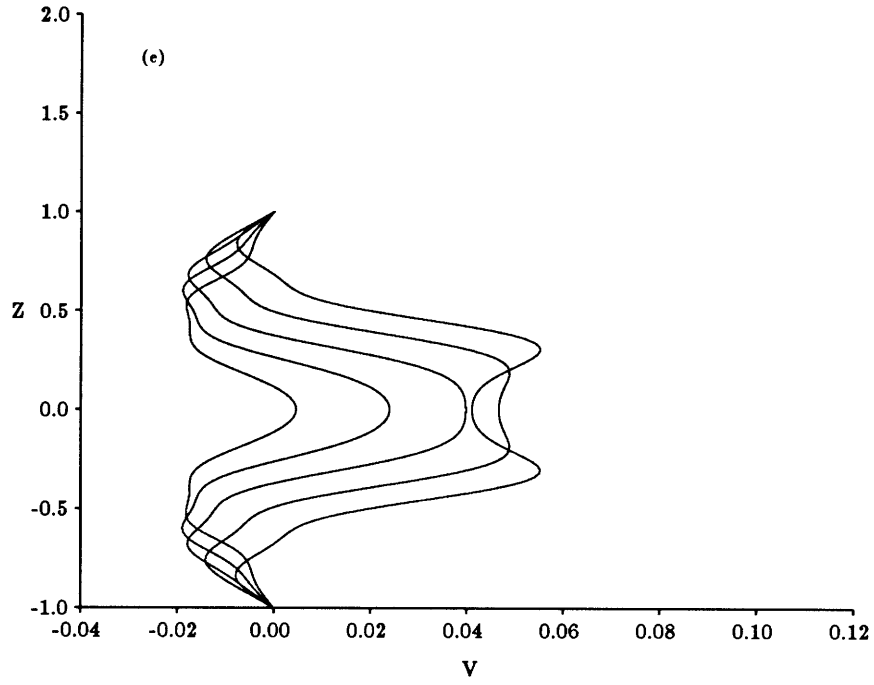

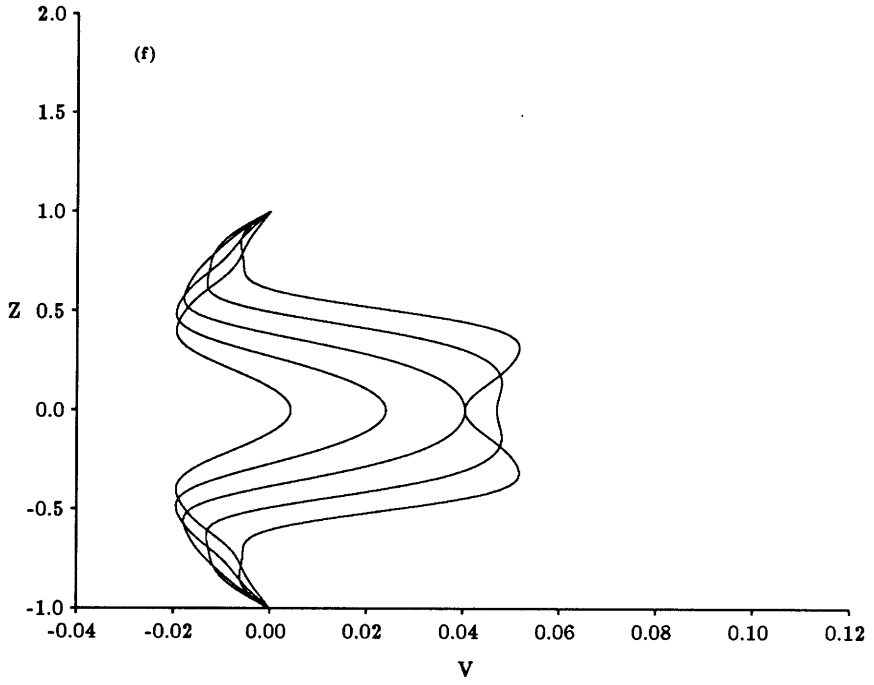

Figure 5.4: v profiles for $c_s = 0.8$ at $t = 35$, $y = 4.22$ calculated from eigenfunctions. (a) $s1$, (b) $s1 + s3$, (c) $s1 + s2 + s3$, (d) $s1 + s2 + s3 + s4$, (e) $s1 + s2 + s3 + s4 + s5$, (f)$s1 + s2 + s3 + s4 + s5 + s6$

Chapter 6

Linear Waves in Plane Poiseuille Flow

The breakdown of the waves seen outside the turbulent spot in plane Poiseuille flow ultimately results in the enlargement of the turbulent spot as shown by Henningson (1989). We will analyze both linear waves in both unmodified and modified plane Poiseuille flow to examine how the modification affects waves.

6.1 Linear waves in unmodified flow field

Plane Poiseuille flow has a parabolic streamwise velocity profile. Linear stability theory shows that a particular 2-dimensional wave with wavenumber $\alpha = 1.021$ phase speed $c = 0.264$ first become unstable at Reynolds number $Re = 5772$ (Orszag, 1971). For other wavenumbers, the corresponding waves are stable. This represents a maximum in the the growth rate $\omega_i = \omega_i(\alpha)$. If the Reynolds number is continuously lowered, this maximum still exists (at least locally) although $\omega_i(\alpha)$ is now negative for all values of α. The value of α at which maximum ω_i occurs also changes continuously with Reynolds number. At the Reynolds number of interest to the present work, $Re = 1000$, this maximum occurs at about $\alpha = 1.25$ with growth rate $\omega_i = \alpha c_i = -0.045$, phase speed

$c_r = 0.4$ and group velocity $c_g = 0.55$.[1] In the following numerical calculations, we will use 64×64 Fourier modes in the x- and y- directions and the computational domain is 40×30 in the (x, y)-plane and 33 Chebychev modes.

We introduce a perturbation to the flow by switching on the antisymmetric forcing term given by Equation (2.5) at time, $t = -5$, and switching it off at time, $t = 0$. The forcing travels with speed, $c_s = 0.55$. This, in effect, perturbs the streamwise pressure gradient and drives the perturbation velocity field. Since the forcing is very weak (c_2=0.0001), the resulting perturbation is linear. After the forcing is switched off at $t = 0$, a free wave packet develops. The least-stable eigenmode is even in the normal velocity, w, and the maximum amplitude occurs at the channel centre-plane. The frame of reference travels with the forcing speed, $c_s = 0.55$. Figure 6.1 (a) shows the contour plots of the normal velocity at the channel centre-plane at the moment the forcing is switched off, $t = 0$, and subsequent plots in Figure 6.1 follow the development of the wave packet. The contour values plotted are $\pm 5 \times 10^{-7}$, $\pm 1.5^{-6}$ and $\pm 2.5 \times 10^{-6}$. If we follow each wave crest in the wave packet through time, we find that wave crests move to the left of the contour plots since the phase speed of the dominant wave is slower than the speed of the frame of reference, while the whole wave packet remains roughly in the same position. The dominant mode of this wave packet has an absolute wavenumber of about 1.1 and is oblique, – not 2-dimensional mode with $\alpha = 1.25$. The appearance of more wave crests is due to dispersion effects. The normal perturbation,

[1]Here c_r and c_i are, respectively, the real and imaginary parts of the eigenvalue of the Orr-Sommerfeld equation. They should not be confused with the notations of Chapter 5. The group velocity based on the real part, αc_r, of the complex frequency still makes sense because c_i is small.

w, starts to decay as soon as the forcing is switched off at $t = 0$. This is consistent with the linear stability theory, which shows that all linear waves are stable at $Re = 1000$.

The decay of streamwise perturbation takes longer. Figure 6.2 shows its development in a plane $z = -0.556$. Initially, at $t = 0$, the perturbation to the streamwise velocity field is just an area of negative perturbation. It soon develops into a wave packet, which grows until $t = 45$ approximately. This could be due to the resonance or near-resonance between the normal velocity and the normal vorticity (see Gustavsson *et al.*, 1980; Gustavsson, 1981 and Henningson, 1990). Another interesting feature is the lengthening of the u-perturbation along the line of symmetry ($y = 0$) as shown in Figure 6.2 (d). This is very likely to be a manifestation of the algebraic instability mechanism analyzed by Landahl (1980). The wave crests are fairly straight and the oblique angles of these wave crests at large time range from about 54 to 70 degrees. The waves become more oblique as time increases. The u-perturbations appear to extend farther in the streamwise direction than in the spanwise direction.

It is interesting to compare these results with those of Henningson, Johansson & Lundbladh (1989). They used Reynolds number, $Re = 6000$, slightly above the critical Reynolds number of 5772, and two pairs of localized vortices as the initial condition, and as a result, the wave packet thus developed consists of very oblique waves from the start. Their contour plots of the normal velocity show that most of the perturbation modes decay rapidly. After some time, only the least-stable ones remain. They also found that the streamwise perturbation velocity grows if the initial perturbations satisfy

the condition for algebraic growth (Landahl, 1980). In the present work the initial wave packet was created by a concentrated disturbance whose amplitude in the Fourier spectrum is largest at $\beta = 0$ for fixed α. Therefore, the wave packet initially consists of both 2-dimensional and oblique waves. The numerical results in Figure 6.1 suggest that the wave packet shows strong oblique wave activities. The different appearances in wave patterns between the these two cases are mainly due to the different initial conditions. The streamwise perturbation grows for quite some time before it finally decays, showing that the algebraic growth may be important even at Reynolds number as low as 1000.

6.2 Importance of oblique waves at subcritical Reynolds numbers

In this section, we will show that 3-dimensional waves are prominant feaure for plane Poiseuille flows at low Reynolds numbers in general.

6.2.1 Eigenvalues of the Orr-Sommerfeld Equation at $Re = 1000$

The Squire's theorem for a viscous flow only states that 2-dimensional waves will become unstable first as the Reynolds number is increased. It does not imply 2-dimensional waves are always more unstable or less stable than 3-dimensional waves. Let α and β represent the streamwise and spanwise wavenumbers respectively. For each set of fixed α, β and Re, the Orr-Sommerfeld equation has an infinite number of discrete eigenval-

ues, one of which has the largest imaginary part. The eigenmode associated with this eigenvalue is either referred to as the most unstable mode if Re is above critical or as the least-stable mode if Re is below critical. Figure 6.3 shows the imaginary part, ω_i (the growth rate), of the eigenvalue of the least-stable mode at $Re = 1000$, as functions of α for fixed values of β. Since the Reynolds number is below the critical value of $Re = 5772$, all linear waves are stable (*i.e* $\omega_i < 0$). For these modes, the closer ω_i is to zero, the less stable they are. We first trace the curve for $\beta = 0$ (2-dimensional waves). As α decreases from some large value towards zero, $\omega_i(\alpha)$ increases to a local maximum at about $\alpha = 1.25$ and then decreases to a local minimum before rising again monotonically. At some finite α, ω_i will pass the local maximum $\omega_i(1.25)$, indicating that long waves (small α) are less stable. Therefore, globally least-stable 2-dimensional eigenmode does not exist in the α interval (0,∞) at $Re = 1000$. Similarly, we can trace curves for the 3-dimensional waves ($\beta \neq 0$). For small values of β, the curves look similar to the 2-dimensional case. For β greater than about 1.0, even the local maximum disappears and 3-dimensional modes are less stable than the 2-dimensional modes. For each fixed β, the maximum ω_i occurs at $\alpha = 0$. Therefore, oblique waves decay slower than 2-dimensional waves.

6.2.2 Longitudinal linear perturbations

We take the extreme case of an oblique wave in which $\alpha = 0$, *i.e.* the perturbations are independent of the streamwise co-ordinate, x. We define a perturbation stream

function ψ as follows

$$v = \frac{\partial \psi}{\partial z}, \tag{6.1}$$

and

$$w = -\frac{\partial \psi}{\partial y}. \tag{6.2}$$

Normal mode analysis of the linear problem leads to the Orr-Sommerfeld equation for $\alpha = 0$:

$$(D^2 - \beta^2)^2 \phi + i\omega Re(D^2 - \beta^2)\phi = 0, \tag{6.3}$$

with boundary conditions

$$\beta\phi(\pm 1) = D\phi(\pm 1) = 0, \tag{6.4}$$

where $D = d/dz$ and ϕ is defined by $\psi = \phi e^{i(\beta y - \omega t)}$. Multiply Equation (6.3) by ϕ^*, the complex conjugate of ϕ, and integrate between $z = -1$ and $z = 1$. We can show that ω is imaginary and its imaginary part $\omega_i < 0$. Equation (6.3) is an ordinary differential equation with constant coefficients subject to homogeneous boundary conditions (6.4). The eigenrelations and the eigenfunctions of Equation (6.3) are easily obtained. Let $\lambda = (-\beta^2 - \omega_i Re)^{\frac{1}{2}}$ (this is a real number since $-\omega_i Re > \beta^2$), the eigenvalue ω_i for even modes satisfy the following relation

$$\lambda \tan\lambda + \beta \tanh\beta = 0, \tag{6.5}$$

The eigenfunction for the even mode is given by

$$\phi = \cosh(\beta z) - \frac{\cosh\beta}{\cos\lambda}\cos(\lambda z), \tag{6.6}$$

and the eigenvalue and eigenfunction for the odd mode are obtained, respectively, by replacing the tangent functions in Equation (6.5) with cotangent functions and the

cosine functions in Equation (6.3) with sine functions, and likewise for the hyperbolic functions. Figure 6.4 shows the wave growth rate as a function of β for $\alpha = 0$. For $\beta = 0$, $\omega_i Re = -\pi^2 \approx -9.8696$. It increases slowly as β increases until reaching a global maximum of $\omega_i Re \approx -9.2702$ at $\beta \approx 1.2$. Noting the scale of the $\omega_i Re$ – axis in Figure 6.4, we find that this maximum is relatively flat. The wave at this wavenumber is less, but not much less stable than waves with smaller wavenumbers. $\omega_i Re$ rapidly decreases toward $-\infty$ on further increase of β. At Reynolds number, $Re = 1000$, the smallest decay rate is $-\omega_i = 0.00927$ at $\beta = 1.2$. We can think of these waves of 90 degree oblique angle as streamwise vortices. Over one wavelength, $2\pi/\beta$, there is one pair of counter-rotating vortices. The "preferred" wave at $Re = 1000$ is one of 90 degree oblique angle with wavelength 5.24 (or $\beta = 1.2$). From the $\omega_i Re$ .vs. β curve in Figure 6.4, we can obtain decay rates of these streamwise vortices at all Reynolds numbers. As Reynolds number increases, the decay rate becomes smaller and tends to zero as Re tends to positive infinity.

The problem discussed above is <u>not</u> a 2-dimensional one since there is also a streamwise perturbation velocity, u, driven by the normal perturbation velocity $w = -\partial\psi/\partial y$. This is governed by the following equation

$$\frac{\partial u}{\partial t} - \frac{1}{Re} \nabla_2^2 u = -U'(z)w = U'(z)\frac{\partial \psi}{\partial y}, \tag{6.7}$$

where $\nabla_2 = \partial^2/\partial y^2 + \partial^2/\partial z^2$ The boundary conditions are

$$u(z = \pm 1) = 0. \tag{6.8}$$

The corresponding inviscid problem was analyzed by Ellingsen and Palm (1975).

They showed that a small streamwise perturbation velocity grows linearly with time. Here, we will illustrate that, even in viscous flow of very low Reynolds number, small streamwise perturbation can grow rapidly for a considerable amount of time.

We consider Equation (6.7) with zero right hand side and boundary conditions (6.8). Let $u = \hat{u}e^{i(\beta y - \sigma t)}$. Subsitituting into Equations (6.7) and (6.8), we can show that σ is imaginary and its imaginary part, $\sigma_i < 0$. We obtain the following eigenvalue problem

$$\sigma_i \hat{u} - \frac{1}{Re}(D^2 - \beta^2)\hat{u} = 0, \tag{6.9}$$

and

$$\hat{u}(\pm 1) = 0, \tag{6.10}$$

where $D = d/dz$. The eigenvalues for the odd modes are given by

$$\sigma_i^{(n)} Re = -\pi^2 n^2 - \beta^2, \tag{6.11}$$

where n is any non-zero integer The eigenfunctions for these modes are given by

$$\hat{u} = \sin(\pi n z). \tag{6.12}$$

Solutions to Equation (6.7) with boundary conditions (6.8) can be expanded in terms of these eigenfunctions. We assume that, initially, ψ on the right hand side of Equation (6.7) is purely the least-stable even mode given by Equation (6.6) with $\omega_i Re = -9.2702$ at $\beta = 1.2$ and corresponding eigenfunction $\phi(z)$,

$$\psi = \phi(z) e^{\omega_i t} \cos(\beta y). \tag{6.13}$$

Since $U'(z)$ is odd for plane Poiseuille flow, the right hand side of Equation (6.7) is odd. We can express the solution of Equation (6.7) as sums of the odd eigenfunctions given

by Equation (6.12)

$$u = \sum_{n=1}^{\infty} B_n(t) \sin(\pi n z). \tag{6.14}$$

It is easy to show that equations for $B_n(t)$'s are

$$\frac{dB_n}{dt} - \sigma_i B_n = -\beta F_n e^{\omega_i t} \sin(\beta y), \tag{6.15}$$

where $n = 1, 2, 3....$ and F_n's are given by

$$F_n = \int_{-1}^{1} \sin(\pi n z) U'(z) \phi(z) dz, \tag{6.16}$$

where ϕ is give by $\phi = \psi e^{i(\beta y - \omega t)}$. We assume that initially there is no streamwise perturbation, *i.e* $B_n(0) = 0$, and solve Equation (6.15) for $B_n(t)$, we get,

$$B_n(t) = -\frac{\beta \sin(\beta y) F_n}{\omega_i - \sigma_i^{(n)}} (e^{\omega_i t} - e^{\sigma_i^{(n)} t}), \tag{6.17}$$

and hence the solution for u is,

$$u = \sum_{n=1}^{\infty} -\frac{\beta \sin(\beta y) F_n}{\omega_i - \sigma_i^{(n)}} (e^{\omega_i t} - e^{\sigma_i^{(n)} t}) \sin(\pi n z). \tag{6.18}$$

Therefore, it is easy to see from Equation (6.18) that u grows linearly for small time, t. Since ω_i and σ_i's are negative, $u(t)$ eventually decays to zero. The question is how long the initial growth lasts. We can answer this by roughly estimating where $u(t)$ reaches a maximum. Since $\mid \sigma_i^{(1)} \mid$ is the smallest among all $\sigma_i^{(n)}$'s, we expect that the first term ($n = 1$) in the sum (6.18) will dominate after some time. Differentiating the first term in Equation (6.18) with respect to time, t, and letting the derivative equal to zero, we find the time, t^*, at which $u(t)$ reaches a maximum

$$t^* = \frac{1}{\omega_i - \sigma_i^{(1)}} \ln(\frac{\sigma_i^{(1)}}{\omega_i}). \tag{6.19}$$

Furthermore, let $a_1 = \omega_i Re$ and $a_2 = \sigma_i^{(1)} Re$, we notice from Equations (6.5) and (6.11) that a_1 and a_2 are functions of β only, independent of Re. We have, therefore,

$$t^* = \frac{Re}{a_1 - a_2} \ln(\frac{a_2}{a_1}). \tag{6.20}$$

Hence, t^* is proportional to the Reynolds number. Since we have chosen $\beta = 1.2$ where the driving term,w, decays the slowest and $a_1 = -9.2702$ and $a_2 = -8.4296$, we have

$$t^* \approx 0.113 Re. \tag{6.21}$$

This implies that for $Re = 1000$ – the Reynolds number of interest in the present work, the perturbation in u will grow for a duration of the order $t^* = 100$. Recall that we nondimensionalized time with the channel centre-plane velocity, $U(0)$, and channel half-depth, h, this growth duration is relatively long.

We can check the estimated duration of the growth, t^*, by numerically solving the an initial value problem. At $t = 0$, let $u = 0$ and the perturbation, ϕ, is assumed to be the eigenfunction given by Equation (6.6). We define the amplitude, A, of ψ to be $\psi(0)$. We also define the total kinetic energy per unit streamwise distance, E_t, and the partial kinetic energy, E_p, as follows:

$$E_t = \frac{1}{2} \int_{-1}^{1} \int_{-\frac{2\pi}{\beta}}^{\frac{2\pi}{\beta}} (u^2 + v^2 + w^2) dy dz, \tag{6.22}$$

and

$$E_p = \frac{1}{2} \int_{-1}^{1} \int_{-\frac{2\pi}{\beta}}^{\frac{2\pi}{\beta}} (v^2 + w^2) dy dz. \tag{6.23}$$

We use an initial small forcing amplitude of $A = 1 \times 10^{-6}$ and solve the Navier-Stokes equations for $Re = 1000$ from $t = 0$ to $t = 200$. We find that the partial energy, E_p,

decays at a rate of $\mid 2\omega_i \mid = 0.0185$, consistent with linear theory. The total energy, E_t, grows by 2 orders of magnitudes in a duration of about 100 before starting to decay. Maximum E_t occurs at $t_* \approx 98$, showing that the rough estimation made earlier ($t^* \approx 113$) was reasonably good. The plots of energy with time are given in Figure 6.6. The same result was obtained by Henningson (1991)from the complete eigenfunction expansion. This large total growth at $Re = 1000$ is higher than the exponential growth of classical 2-dimension Tollmien-Schlichting waves. Orszag and Patera (1982) point out that maximum growth rate for Tollmien-Schlichting waves occurs at $Re \approx 48000$, with perturbations growing by a factor of only 10 in amplitude (or 100 in energy) in a time of about 300. The relatively fast growth of the the streamwise perturbation is due to the fact that $\mid \omega_i \mid$ and $\mid \sigma_i \mid$ are small and close, although not equal to each other. There is no exact resonance, but near-resonance is present.

6.2.3 Perturbations of finite extent

In reality, perturbations are of finite spatial extent. Such perturbations in a viscous flow can be analyzed by the algebraic growth theory of Landahl (1980) with an added viscous term. We linearize the Navier-Stokes equations around the parabolic velocity, U(z). After some simple algebra, we get the following set of linear equations

$$\frac{\partial \bigtriangledown^2 w}{\partial t} - \frac{1}{Re} \bigtriangledown^4 w + U\frac{\partial \bigtriangledown^2 w}{\partial x} + \frac{d^2U}{dz^2}\frac{\partial w}{\partial x} = 0, \tag{6.24}$$

$$\frac{\partial u}{\partial t} + U\frac{\partial u}{\partial x} - \frac{1}{Re} \bigtriangledown^2 u = -\frac{\partial p}{\partial x} - w\frac{dU}{dz}, \tag{6.25}$$

$$\frac{\partial u}{\partial x} + \frac{\partial v}{\partial y} + \frac{\partial w}{\partial z} = 0, \tag{6.26}$$

$$\nabla^2 p = -2\frac{dU}{dz}\frac{\partial w}{\partial x}, \tag{6.27}$$

where the $\nabla^4 = \nabla^2(\nabla^2)$, ∇^2 being the 3-dimensional Laplacian operator. The boundary conditions are

$$u(x, y, \pm 1) = v(x, y, \pm 1) = w(x, y, \pm 1) = \frac{\partial w}{\partial z}(x, y, \pm 1) = 0. \tag{6.28}$$

Following Landahl's procedure, we define a overlined quantity, $\overline{Q}$, as follows

$$\overline{Q} = \int_{-\infty}^{\infty} Q dx, \tag{6.29}$$

where Q represents any perturbation variable, u, v, w, p *etc.*, assuming that these variables are sufficiently localized such that integral (6.29) exists. We integrate Equations (6.24) through (6.26) with respect to x, we obtain

$$\frac{\partial \nabla_2^2 \overline{w}}{\partial t} - \frac{1}{Re} \nabla_2^4 \overline{w} = 0, \tag{6.30}$$

$$\frac{\partial \overline{u}}{\partial t} - \frac{1}{Re} \nabla_2^2 \overline{u} = -\overline{w}\frac{dU}{dz}, \tag{6.31}$$

$$\frac{\partial \overline{v}}{\partial y} + \frac{\partial \overline{w}}{\partial z} = 0, \tag{6.32}$$

$$\nabla^2 \overline{p} = 0, \tag{6.33}$$

where the overlined variables are streamwise integrated quantities and $\nabla_2 = \partial^2/\partial y^2 + \partial^2/\partial z^2$. Boundary conditions are

$$\overline{u}(y, \pm 1) = \overline{v}(y, \pm 1) = \overline{w}(y, \pm 1) = \frac{\partial \overline{w}}{\partial z}(y, \pm 1) = 0. \tag{6.34}$$

The integrated flow system governed by Equations (6.30) through (6.32) are mathematically equivalent to the longitudinal perturbation problem of the last subsection. If

the x-averaged initial normal velocity $\overline{w} \neq 0$, then the x-averaged streamwise velocity $\overline{u}$ can grow rapidely for a relatively long time as analyzed in the last subsection. As Reynolds number tends to infinity, the present viscous problem approaches the inviscid algebraic instability problem of Landahl (1980). In numerical simulations shown in Figure 6.2, the streamwise velocity apparently grows for a duration of of about 45 non-dimensional time units. It should be stressed here that this growth mechanism only exists if the perturbations are 3-dimensional since $\overline{w}$ would always be zero if there were no spanwise variation in the perturbation field – a result consistent with the continuity equation (6.32).

6.2.4 More on 3-dimensionality at low Reynolds numbers

The last two subsections have shown that, at $Re = 1000$, the most 'preferred' wave in a plane Poiseuille flow is a longitudinal wave of wavenumber, $\beta \approx 1.2$. Furthermore, there is not a 'most preferred' wave in a 2-dimensional problem at this Reynolds number. We clearify this point in this subsection.

Supposing we continuously lower the Reynolds number from its critical value of 5772. At first, the 'most preferred' wave is a 2-dimensional one having the smallest decay rate amongst all eigenmodes. At $Re = 4810$, the longitudinal wave with $\beta = 1.2$ takes over to become the globally slowest decaying wave. At $Re = 4745$, the 'most preferred' wave no longer exists in a 2-dimensional problem, the 2-dimensional 'wave' with wavenumber, $\alpha = 0$, decays the slowest with decay rate $\mid \omega_i \mid = \pi^2/Re$. Figure 6.5

shows the growth rate, $\omega_i(\alpha)$, for Reynolds numbers of 1000, 2800, 4000 and 6000. At $Re = 6000$, slightly positive growth rate exists around $\alpha = 1.02$, where the $\omega_i(\alpha)$ curve has a global maximum. At lower Reynolds numbers, this maximum becomes local and the waves with small α are less stable.[2]

When the initial disturbance is localized, it usually consists of modes in a wide range of α and β. In certain studies, such as primary finite amplitude waves and the secondary instability of these finite amplitude waves, in which the Reynolds number of interest ranges from about 1000 to 2800, it may not be justified to consider only 2-dimensional waves, since oblique waves may be the dominant feature of the primary disturbance at Reynolds numbers much lower than about 4810.

The evolution of linear waves discussed so far shows possible growth in the streamwise and spanwise velocities for some time at low Reynolds numbers, but not in the normal velocity. Yet, the numerical simulation (Henningson *et al.*, 1987) of the turbulent spot in plane Poiseuille flow shows strong growth in the normal velocity. This implies that these mechanisms are not the only ones to play a role (if any role at all) in the growth of the turbulent spot.

[2]The determination of the Reynolds numbers $Re = 4810$ and $Re = 4745$ was done by trial and error using a shooting method. The aim is to illustrate the points under discussion, not the determination of accurate numbers. The error is within ± 1

6.3 Linear waves in modified flow field

When plane Poiseuille flow is modified by a turbulent spot, the stability properties of the flow field around the spot is altered. The modified flow field is characterized by highly inflexional spanwise velocity profiles, indicating the resulting instability is of inviscid type, if there is instability. In this section, we will analyze how the modified flow field changes the stability characteristics of the small perturbations.

We have discussed, in Chapter 4, that a symmetric Reynolds stress forcing produces distortions to the parabolic velocity profiles. The spanwise velocity profiles are inflexional, indicating the possible existence of instability. Henningson (1989) showed that the "cross-flow" inflexional instability is the dominating factor for the exponential wave growth. We introduce a small perturbation to the modified flow field and observe whether the perturbation will grow in this modelled problem.

Four cases of different forcing speed are represented: (i) $c_s = 0.6$, (ii) $c_s = 0.8$, (iii) $c_s = 0.7$ and (iv) $c_s = 0.95$. In all three cases, $Re = 1000$ and forcing strength, $c_1 = 0.05$.

Case (i) $c_s = 0.6$

We switch on the symmetric forcing with strength $c_1 = 0.05$ at $t = -35$. It travels with $c_s = 0.6$. The flow field is already considerably modified at time $t = -5$. Then, a very weak antisymmetric forcing, $c_2 = 0.0001$, is switched on between $t = -5$ and

$t = 0$ to create some linear disturbance. After c_2 is switched off at $t = 0$, c_1 is kept as it is to continue modifying the flow field. The perturbation is allowed to develop as a free linear wave packet in the modified field. At $t = 0$, the initial perturbation in the spanwise velocity, w, in the channel centre-plane, is roughly the same as in the case with unmodified flow field. Figure 6.7 shows the contour plots of the normal velocity, w, in the channel centre-plane. As before, the contour values plotted are $\pm 5 \times 10^{-7}$, $\pm 1.5^{-6}$ and $\pm 2.5 \times 10^{-6}$. The wave patterns of the resulting wave packet look remarkably different from those in the previous case of unmodified flow field. Instead of the bow-shaped waves crests that decay, we now have wave crests that are fairly straight and are still growing at $t = 30$. The waves near the origin $(x, y) = (0, 0)$ (the inner waves), where the modelled turbulent spot is located, appear to have shorter wavelengths and are more oblique than those further away from the origin (outer waves) (see, Figure 6.7 (d)), the absolute wavenumber ranges from about $k = 1.6$ for outer waves at oblique angles of about 55 degrees to about $k = 2.1$ for inner waves at oblique angles of about 72 degrees. The analysis of the numerical simulation (Henningson, 1988) gives a wavenumber of about $k = 1.88$ at an oblique angle of about 68 degrees in regions where waves are most unstable.

Case (ii) $c_s = 0.7$

We repeat Case (i) with everything unchanged except now the forcing travels at a higher speed, $c_s = 0.7$. The growing waves in the destabilized regions become more oblique than before. The typical absolute wavenumber is about, $k = 2.0$, and the oblique angles range from about 64 to 80 degrees. There is another interesting feature in this

case. The modelled turbulent spot leaves behind some decaying waves which very much resembles those discussed before in unmodified flow field. Unable to keep up with the modelled spot, these waves move out of the region of modified flow field and eventually decay. Figure 6.8 show the contour plots of the w-velocity in the channel centre-plane, $z = 0$, for this case.

Case (iii) $c_s = 0.8$

We again repeat Case (i) with everything unchanged except that now forcing travels at an even higher speed, $c_s = 0.8$. Amplitudes of the wave crests on the sides of the forcing appear to be smaller than in Case (i) and (ii), while the trailing waves are stronger than in Case (ii). This case is shown in Figure 6.9 (a) and (b) for $t = 20$ and $t = 30$. We find that the long wave crests at $t = 20$ have each split into two parts. One part grows in the modified mean flow region and the other part breaks away to from the trailing waves. The typical wavenumber of the growing waves is about, $k = 2.2$, and the oblique angles range from about 70 to 75 degrees.

Case (iv) $c_s = 0.95$

We repeat the calculations again with $c_s = 0.95$. Figure 6.10 shows the contour plots of the normal velocity, w in the the channel centre-plane, $z = 0$. Again oblique waves appear on each side of the modelled spot. The slow trailing waves found in Cases (ii) and (iii) are also present. The amplitudes of waves on the sides of the forcing appear to be smallest amongst all four cases, while amplitudes of the trailing waves are largest.

The waves on the sides of the forcing have typical wavenumber of about, $k = 2.6$. The oblique angle of these waves is about 78 degrees.

We can make cross comparisons among Figure 6.7 (b), Figure 6.8 (b), Figure 6.9 (b) and Figure 6.10 (b), showing the contour plots of the normal velocity, w, for these four cases at $t = 30$. The amplitudes of the wave crests on the sides of the forcing decrease as the forcing speed is increased from, $c_s = 0.6$, in Case (i) to $c_s = 0.95$ in Case (iv). The streamwise positions in which the growing waves appear are approximately $x = 4$, $x = 3$, $x = 0$ and $x = -3$ for $c_s = 0.6$, $c_s = 0.7$, $c_s = 0.8$ and $c_s = 0.95$ respectively. They correspond to the approximate positions of the slow modes of the large scale modifications to the flow field (see Figure 4.5). No waves grow in positions where the fast modes of large scale flow are located. This suggests that the destabilization of the flow field is attributed to the slow modes of the large scale flows. These modes travels at speeds slower than about 0.8 (the phase speed of s3 mode of the normal vorticity equation discussed in Chapter 4). The growth of a turbulent spot in a real plane Poiseuille flow is maintained by the breakdown of oblique waves in the destabilized regions, and if these regions travel with speeds smaller than about 0.8, the propagation of the spot front is unlikely to exceed this speed. The preceding results show that as the forcing speed is increased from $c_s = 0.6$, the amplitudes of the waves on the sides of the travelling forcing decrease while their oblique angles increase. The wavenumber, phase speed and oblique angle of the waves are compared with the numerical simulation of Henningson *et al.* (1987) and the experiment of Henningson *et al.* (1987). The agreement is good (Table 6.1).

-	c_s	k	Phase speed	Obli. ang. (^{o})	Re
1	0.7	2.0	0.60	64-80	1000
2	0.7	2.0	0.58	45-70	2000
3	0.69*	1.88	0.62	68	1500
4	-	1.89	0.53	64	1500

Table 6.1: Comparison between the present work (1 and 2) and the numerical simulation of Henningson, Spalart & Kim, 1987 (3) and the experiment of Henningson & Alfredsson, 1987 (4). * The speed of the region where waves are most unstable.

The experiment of Carlson *et al.* (1982) showed wave activities in the rear of the turbulent spot as well as in the destabilized regions on the sides at the early stages of the spot development. The slow, decaying waves trailing the forcing seen in Cases (ii) and (iii) may be related the waves in the rear of a early-stage spot. These waves may be present early in the spot's development because the initial spot-triggering is asymmetric (*e.g* inject of fluid from one wall). These waves eventually decay, leaving only the growing waves the destabilized flow regions.

6.4 Wave growth at higher Reynolds numbers

In the last section, the Reynolds number used was 1000 in all cases. Alavyoon *et al.* (1986) showed, by flow visualization, that the rate of spanwise spreading of the

turbulent spot is proportional to the Reynolds number. In this section, we will examine the waves at Reynolds number, $Re = 2000$.

The symmetric forcing strength is the same as that in the cases for $Re = 1000$ presented in the last section, $c_1 = 0.05$. This is switched on at, $t = -35$, and perturbations to the mean flow take place. An antisymmetric forcing of strength, $c_2 = 0.0001$ is switched on at, $t = -5$ and then switched off at, $t = 0$. The speed of the forcing is chosen to be, $c_s = 0.7$. As mentioned in Chapter 4, the distortions to the mean flow at $Re = 2000$ is about the same as those at $Re = 1000$, only slight differences in amplitude of the streamwise perturbation velocity can be noticed after time, $t = 30$ (*i.e* a duration of 65 nondimension time units after the start of the symmetric perturbation at, $t = -35$). Figure 6.11 (b) shows the contours of the w -velocity at, $t = 20$, in plane, $z = 0$. The Typical wavenumber is around, $k = 2.0$, and oblique angles range from 45 to 70 degrees. The amplitudes of these waves are larger than the corresponding case at $Re = 1000$ shown in Figure 6.8 (a). The phase speed of the waves is about 0.58. In the numerical simulation of Henningson *et al.* (1987) and Henningson (1989) for $Re = 1500$, the "wing tip" regions where wave-growth are observed travel at speed of about 0.69 and the waves in these region have a phase speed of about 0.62.

In order to stress the fact that the growing waves on each side of the forcing are riding on the large scale modifications to the mean flow, the streamwise perturbation velocity contours, at $t = 20$, in the plane, $z = 0.556$, are shown in Figure 6.11 (a). We notice that the positions of the growing waves coincide with the positions of the region of large scale positive streamwise perturbations represented by the closed solid curves

on either the of the forcing shown in Figure 6.11 (a).

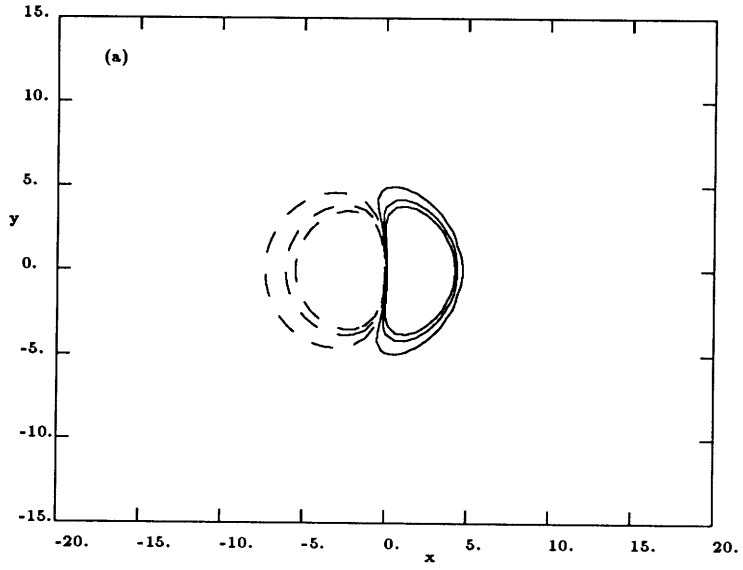

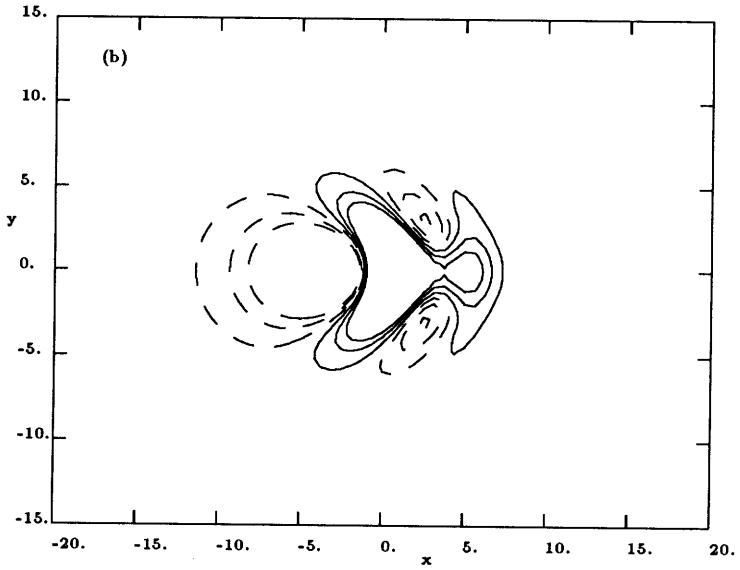

see next page for caption

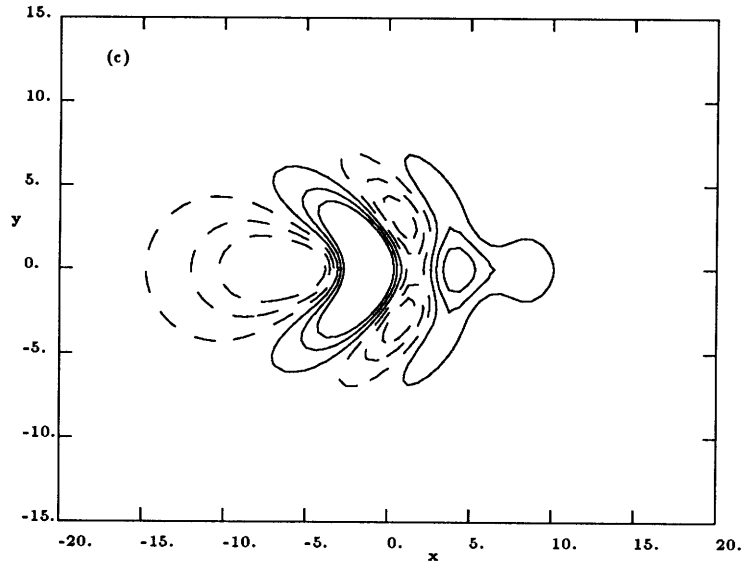

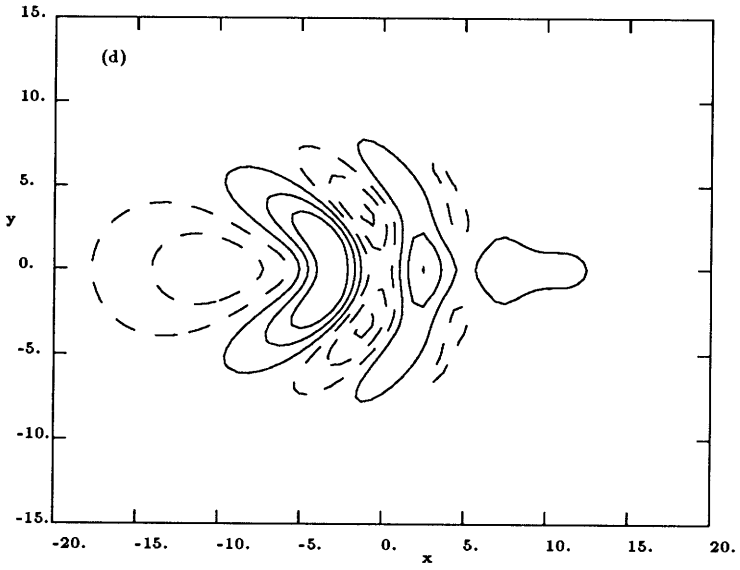

see next page for caption

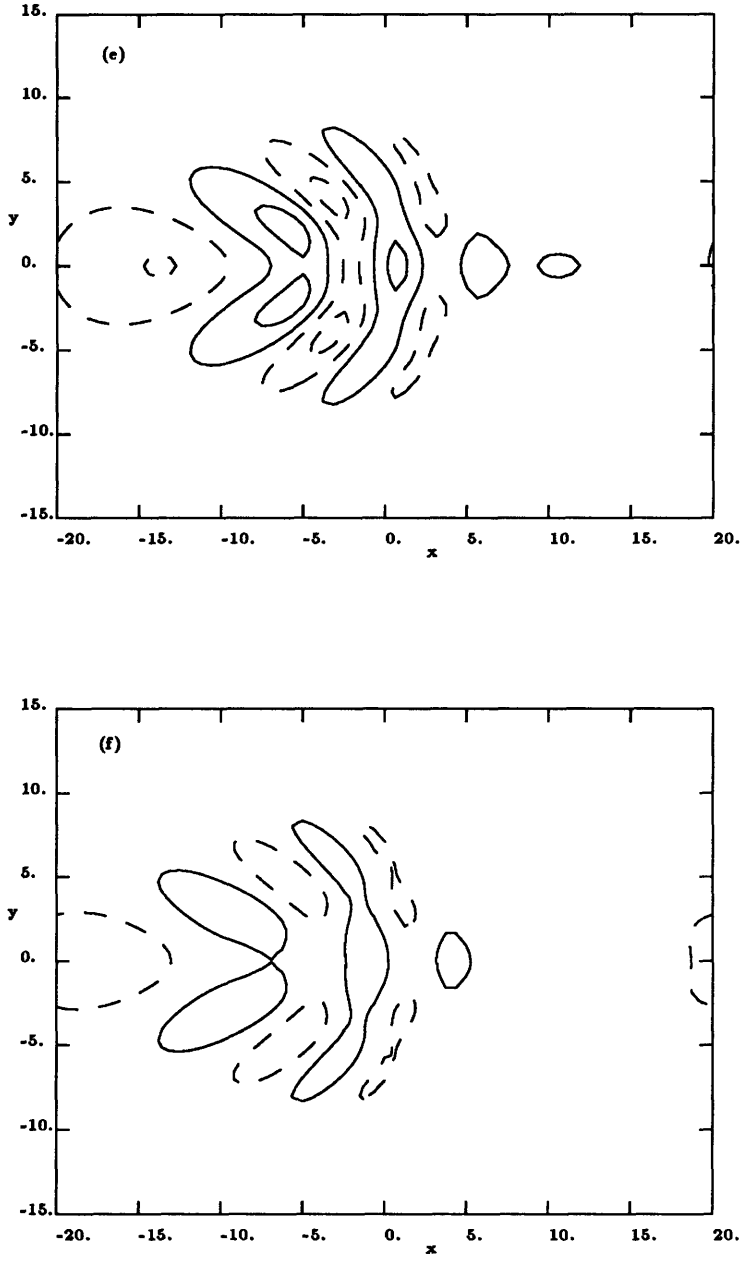

Figure 6.1: Normal velocity contours at $z = 0$. Contours start at -0.0000025, increment=0.000001. (a)$t = 0.0$, (b)$t = 10$, (c)$t = 20$, (d)$t = 30$, (e)$t = 40$, (f)$t = 50$.

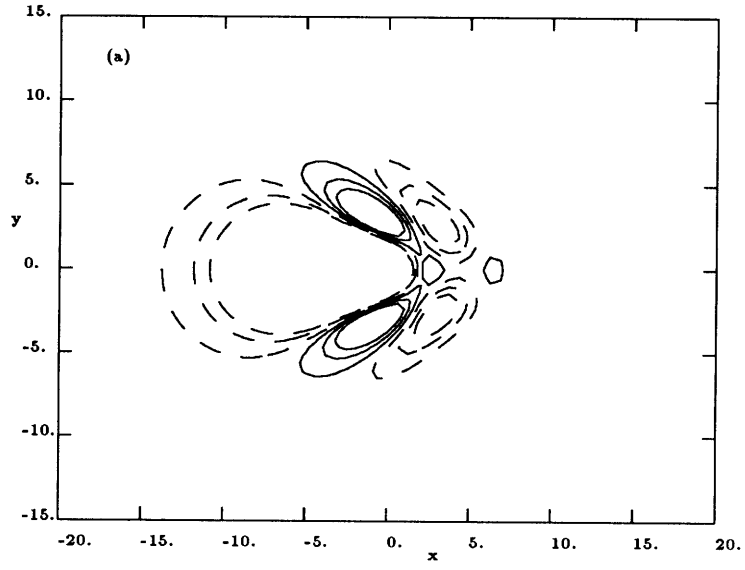

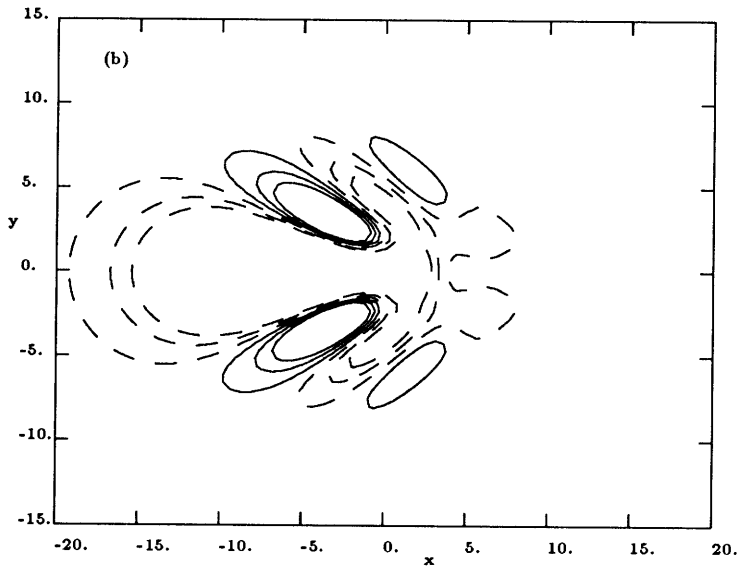

see next page for caption

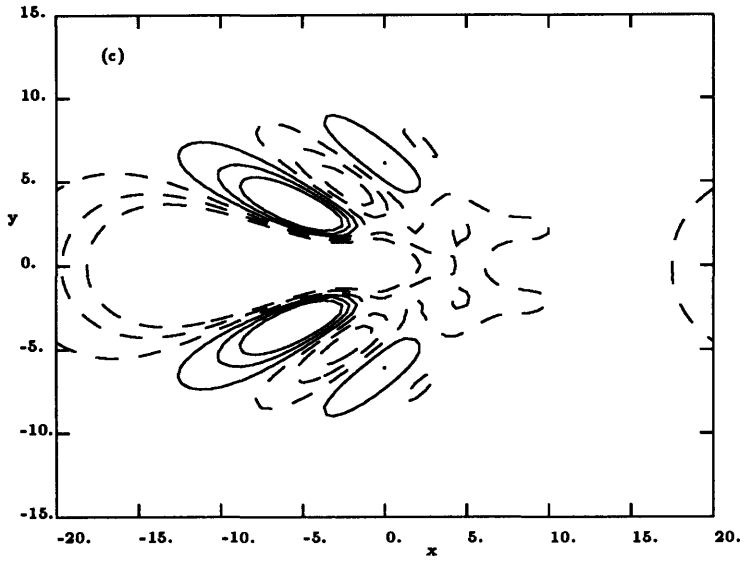

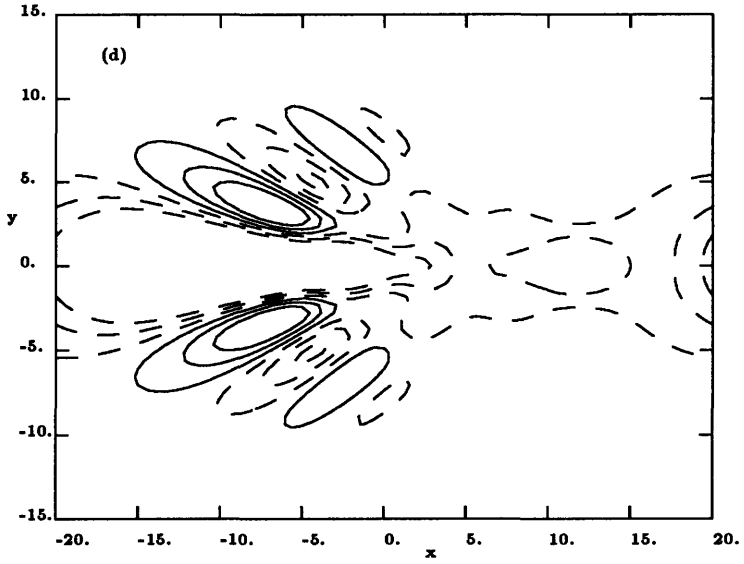

Figure 6.2: Streamwise perturbation velocity. Contours start at -0.000005, increment=0.000002. (a) $t = 20$, (b)$t = 30$, (c)$t = 40$, (d)$t = 50$.

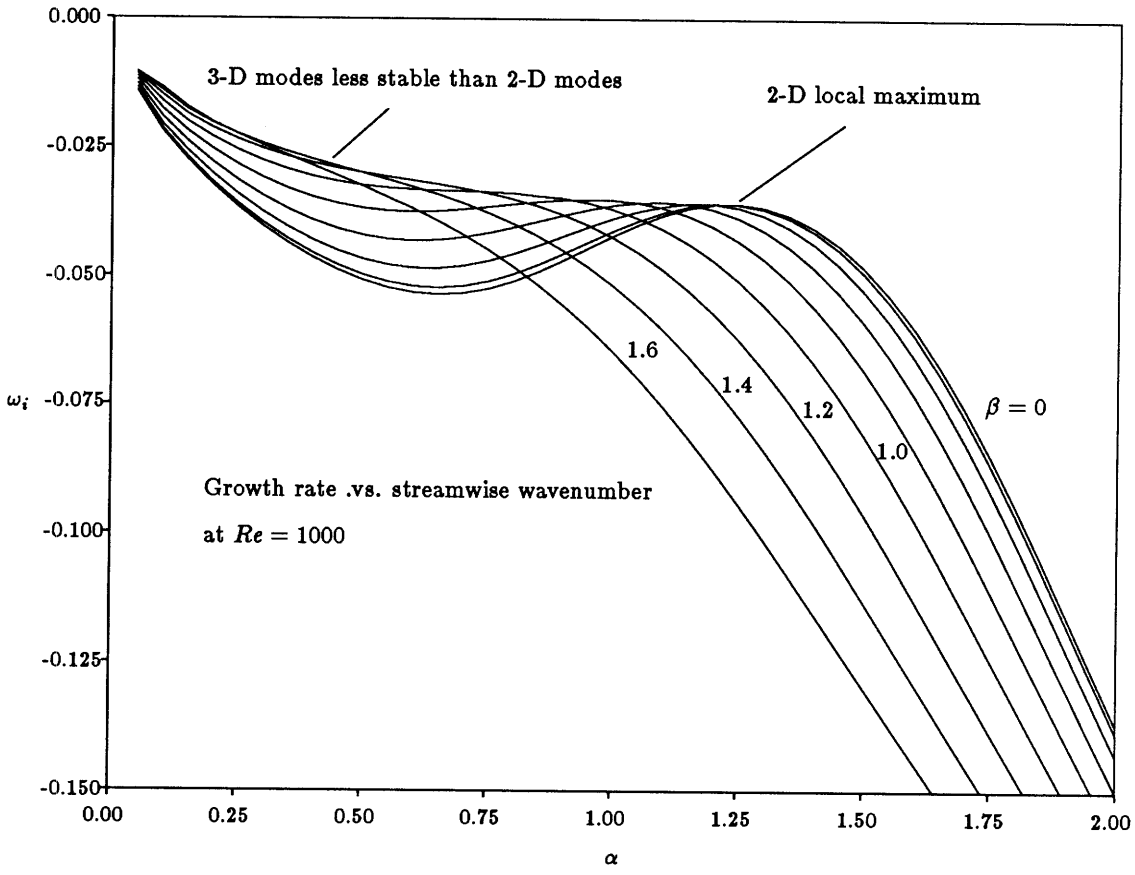

Figure 6.3: Growth rate, ω_i *.vs.* streamwise wavenumber, α. Each line has a fixed β value.

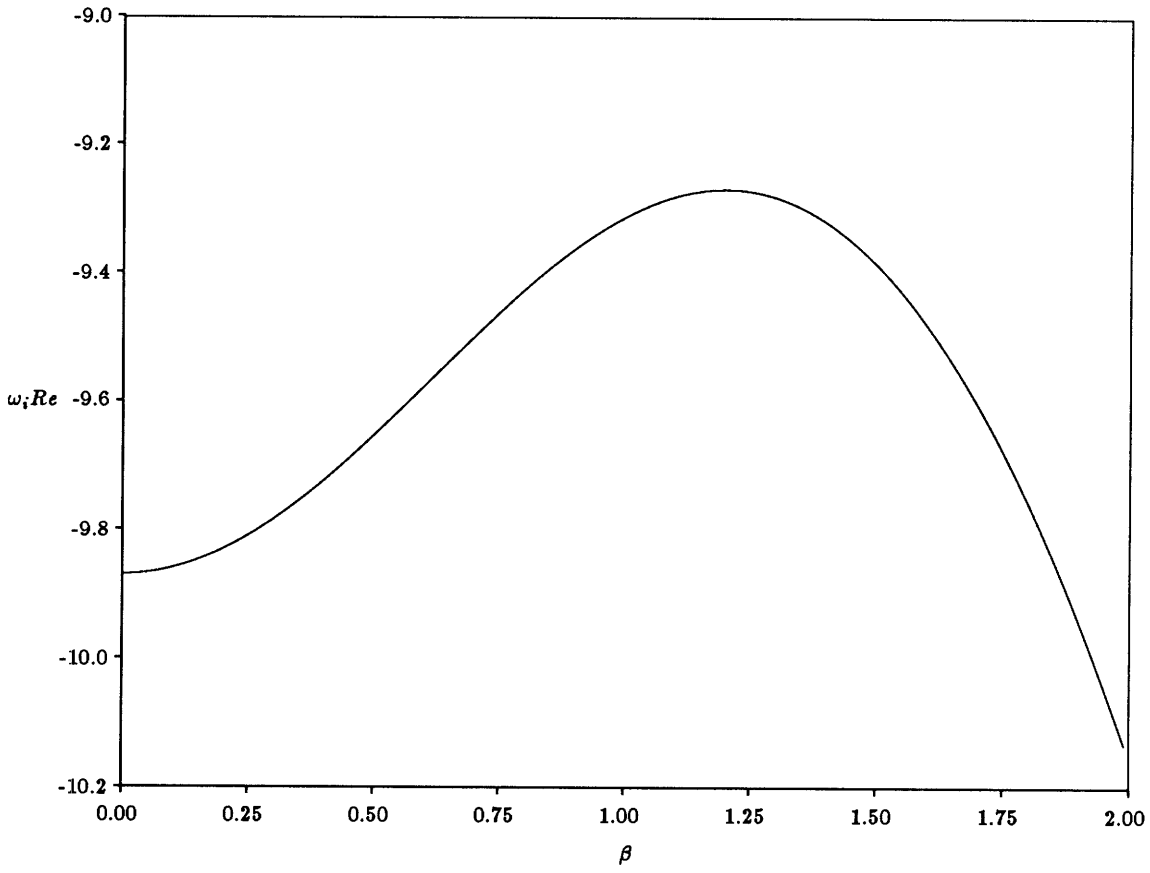

Figure 6.4: $\omega_i Re$ as a function of β for $\alpha = 0$.

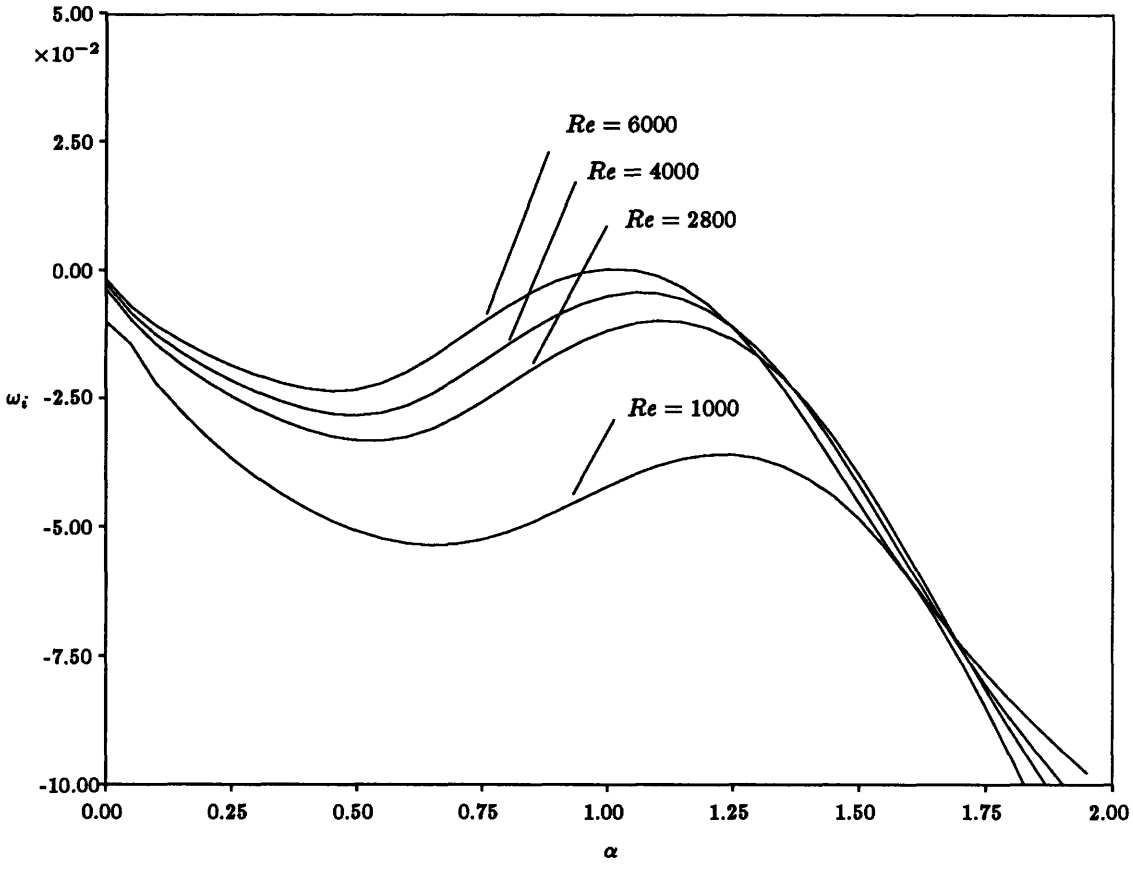

Figure 6.5: Growth rate for 2-dimensional waves at different Reynolds numbers

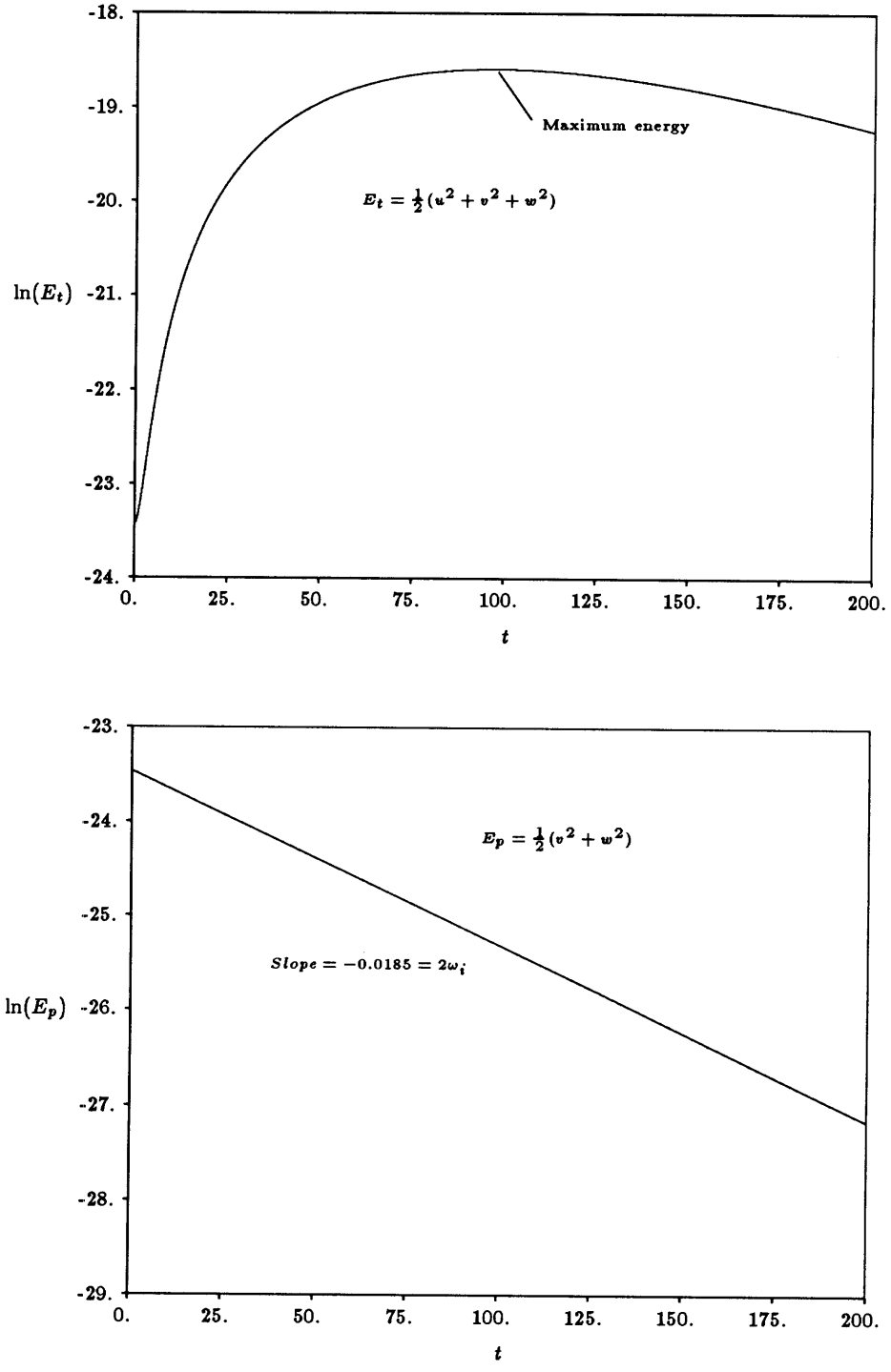

Figure 6.6: Growth of total energy E_t and partial energy E_p in natural logarithmic scale

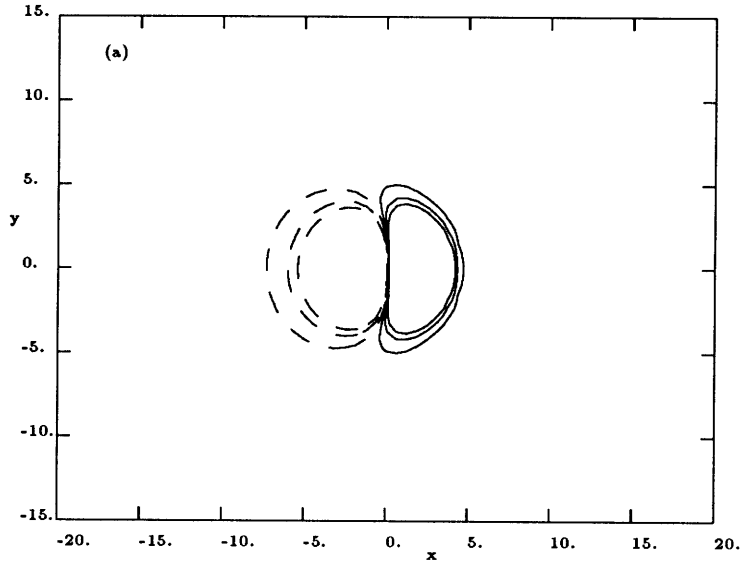

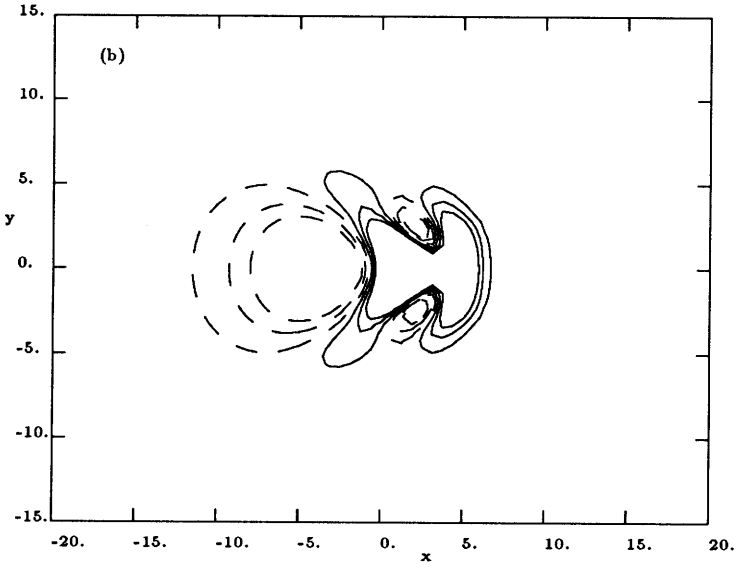

see next page for caption

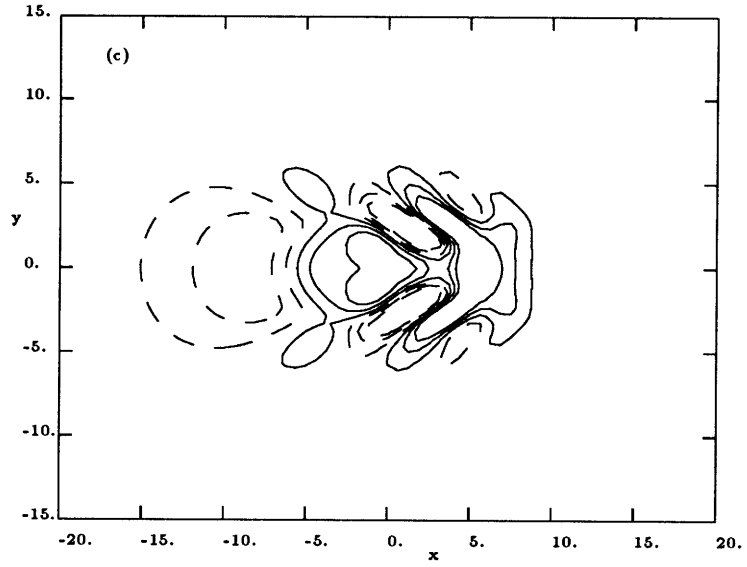

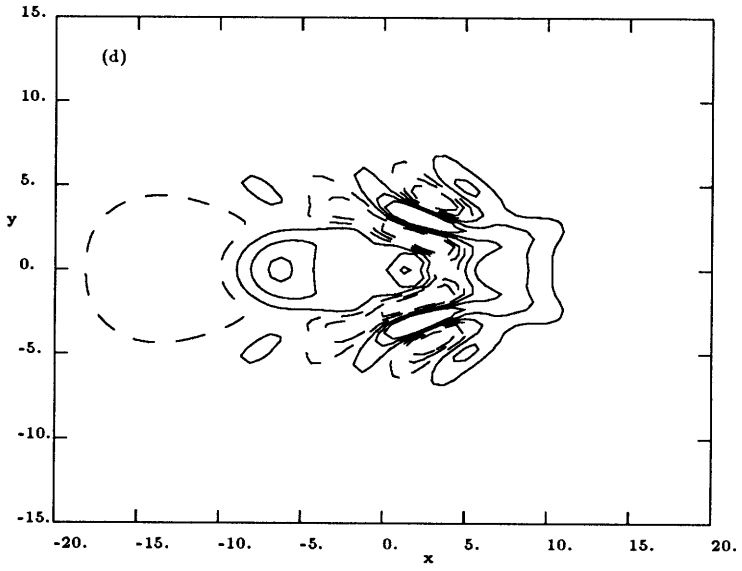

Figure 6.7: Contours of w for $c_s = 0.6$. Contours start at -0.0000025, increment=0.000001. (a)$t = 0$, (b)$t = 10$, (c)$t = 20$, (d)$t = 30$.

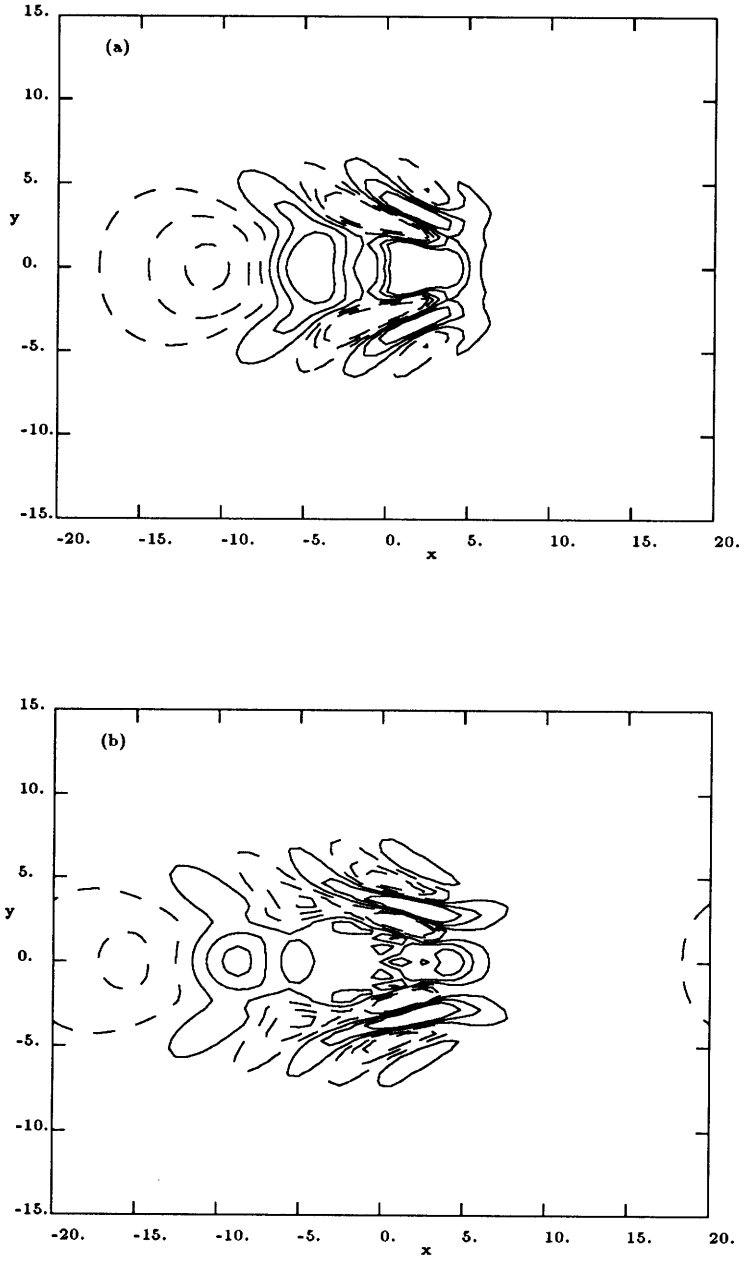

Figure 6.8: Contours of w for $c_s = 0.7$. Contours start at -0.0000025, increment=0.000001. (a)$t = 20$, (b)$t = 30$.

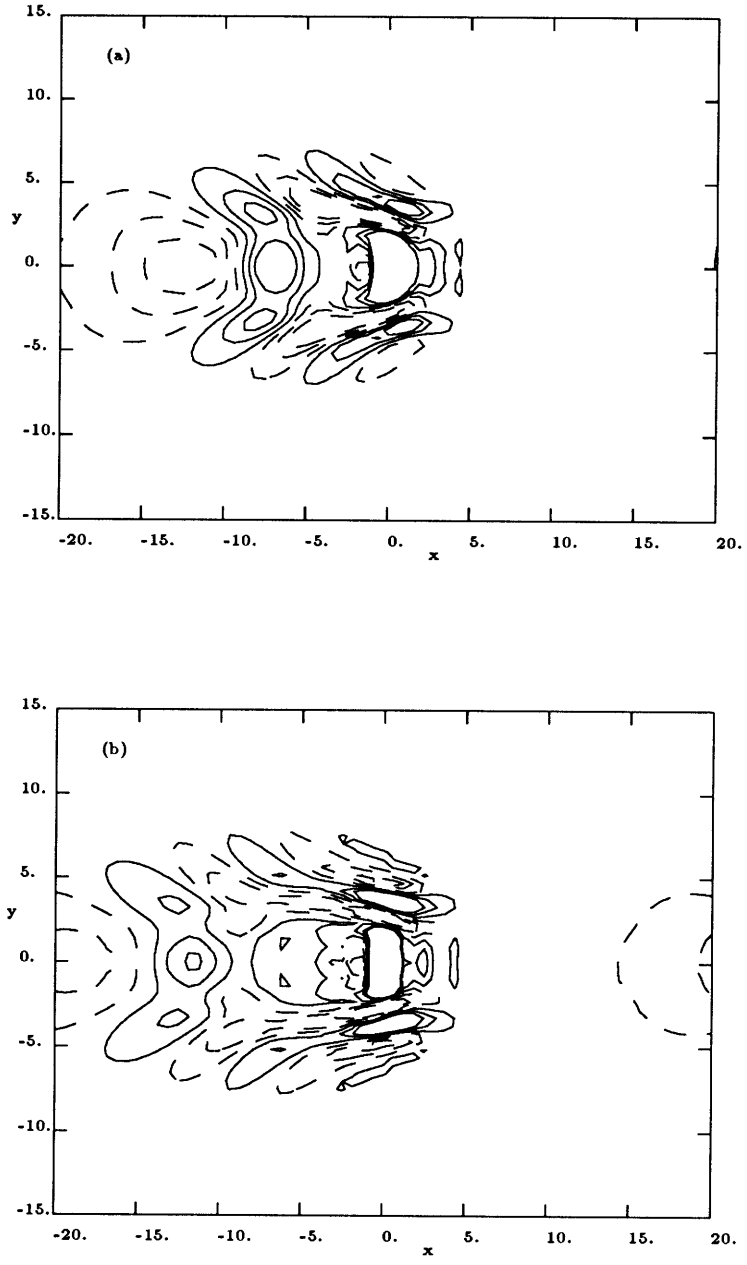

Figure 6.9: Contours of w for $c_s = 0.8$. Contours start at -0.0000025, increment=0.000001. (a)$t = 20$, (b)$t = 30$.

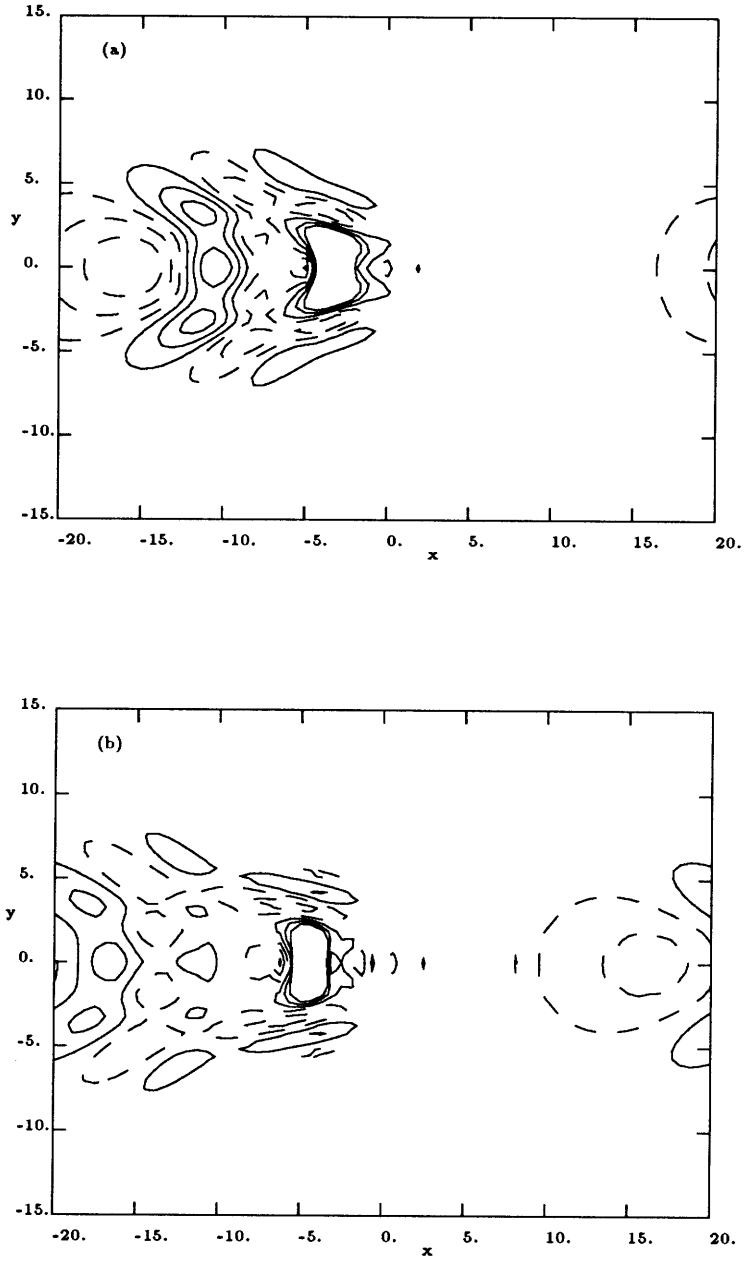

Figure 6.10: Contours of w for $c_s = 0.95$. Contours start at -0.0000025, increment=0.000001. (a)$t = 20$, (b)$t = 30$.

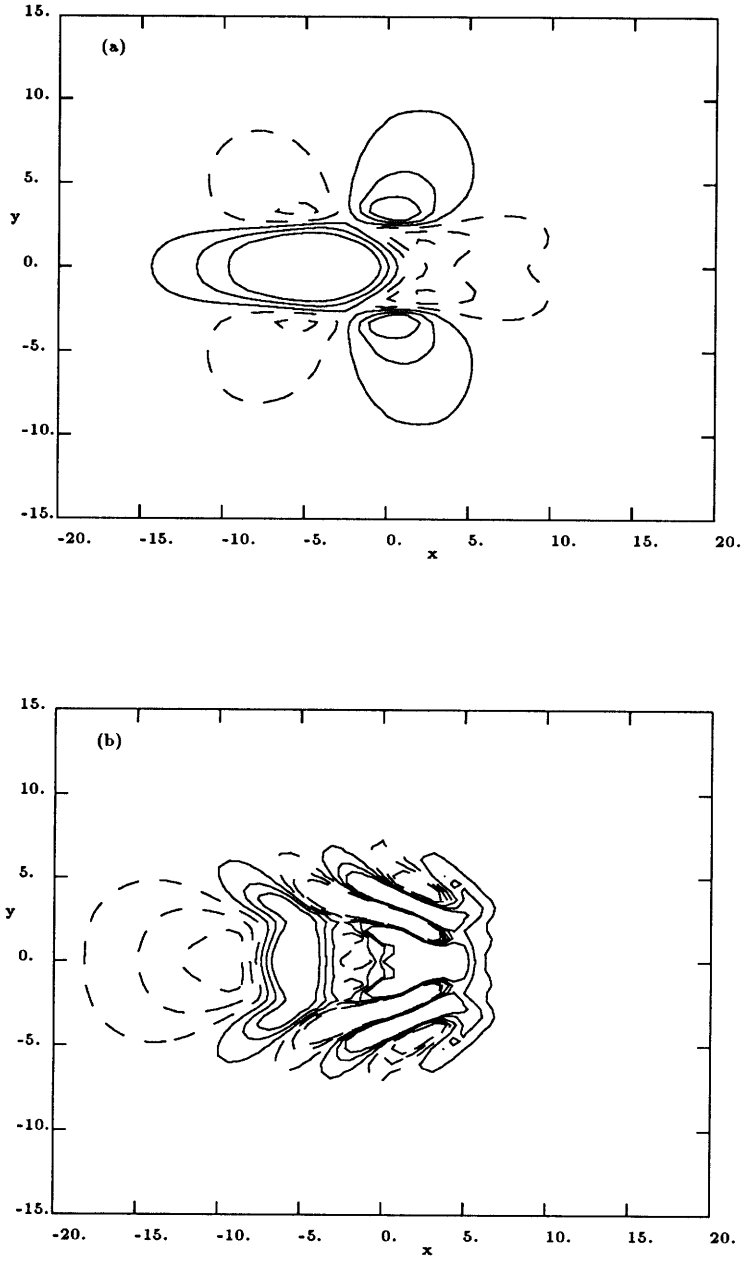

Figure 6.11: Contours of plots for $c_s = 0.7$ at $t = 20$. (a) u-contours start at -0.05, incr=0.02, (b)w-contours start at -2.5×10^{-6}, incr=10^{-6}

Chapter 7

Finite Amplitude Waves

Linear wave growth represents the initial stage of the transition process. As the amplitude of the waves increases, nonlinear interactions between the waves and mean flow takes place, *i.e.* the strong waves can now modify the mean flow. In this chapter we examine finite amplitude waves in plane Poiseuille.

7.1 Finite amplitude waves in unmodified flow field

Here, we introduce a strong disturbance by switching on the antisymmetric forcing with relatively large magnitude, $c_2 = 0.05$, (c_2 was 0.0001 in the corresponding linear case shown in Chapter 6) and travelling at speed, $c_s = 0.6$, while keeping the symmetric forcing zero. This is done at time, $t = -30$. At time $t = 0$, this antisymmetric forcing is switched off. The large scale perturbations to the mean flow as discussed in Chapter 4 are not present, therefore, we can consider the perturbations so created as strong waves in a parabolic background flow. Figure 7.1 follows the development of the perturbation at $t = 10$ and 20. The resulting wave packet consists of very oblique waves. At $t = 20$, the front waves of wave packet become almost 90^o oblique, while rear waves are less so. The front waves have a wavelength of about 2.5, therefore, the very oblique waves are

unrelated to the slowest decaying longitudinal wave discussed in the last chapter, which has a wavelength of about 5.2. Rather, they may be related to the least damped mode on the P-branch of the eigenspectrum of the Orr-Sommerfeld equation as explained by Henningson, Johansson & Lundbladh (1989). These waves do not seem to spread rapidly into the surroundings, indicating that flow modification is necessary for rapid growth even for strong waves.

7.2 Finite amplitude waves in modified flow field

We start by creating some very large symmetric modifications to the flow field and at the same time perturbing the flow antisymmetrically to generate a wave packet. At $t = -30$ we switch on a strong symmetric forcing with $c_1 = 0.1$ and a strong antisymmetric forcing with $c_2 = 0.05$. The forcing travels at speed, $c_s = 0.6$. The former serves to modify the large scale flow field, while the latter generate small scale perturbations. The antisymmetric forcing is switched off at time, $t = 0$, while the symmetric forcing is kept constant at $c_1 = 0.1$ as time advances to maintain the modified large scale flow.

Figure 7.2 shows the contour plots of the normal velocity, w, at time, $t = 0$, 10, 20, and 30 at the channel centre, $z = 0$. The contour values plotted are $w = -0.02$ and $w = 0.02$. At time, $t = 0$, we already see strong, growing oblique waves in regions with strong large scale modification of the flow field. At $t = 10$, more waves crests are visible and they become more oblique. At $t = 20$ and $t = 30$, oblique angles of the wave

crests do not seem to change by any significant amount with time. The waves crests closer to $(x, y) = (0, 0)$, where the forcing is centered, are slightly more oblique than those farther away (from about 74 degrees to 67 degrees). The dominant wavenumber is around 2.1 (Numerical simulations of Henningson (1990) shows the wave number is around 1.88). We identify some wave crests by numbering them. (see Figure 7.2 (d)). Amplitudes *.vs.* time is plotted in logarithmic scale in Figure 7.3, showing the development of these wave crests between $t = 10$ to $t = 55$. The large amplitude wave crests near the origin, $(x, y) = (0, 0)$, grow slower than small amplitude waves away from the origin. All waves crests seem to settle to a finite amplitude of approximately 0.1, indicating that there may be some neutrally stable state for these nonlinear waves, although the computation has not proceeded for long enough to verify this point. No breakdown of the waves is observed. The straight line for wave crest number 5 indicates exponential growth. Growth rate of wave crest number 5 (the slope of line number 5), is approximately 0.13 (13 percent growth in amplitude per unit time).

The growth rate discussed above is that of each individual wave crest. We can also get an idea of how the amplitude of the wave group evolves. We will do the following filtering operation whose purpose will become clear soon:

- Fourier-transform $(w^2)^{\frac{1}{2}}$ –the root square of the normal velocity.
- Applied a low pass filter to the transformed quantity. The filter is given by:

$$f(\alpha, \beta) = 1, \tag{7.1}$$

if $\alpha < a$ and $\beta < b$; and

$$f(\alpha,\beta) = e^{-(\alpha-a)^2-(\beta-b)^2}, \tag{7.2}$$

if $\alpha > a$ or $\beta > b$.

- Inverse Fourier-transform the filtered quantity.

The filter thresholds a and b are chosen to be, respectively, 0.471 and 0.628. Therefore, the largest unfiltered wavenumber is $k = \sqrt{a^2 + b^2} = 0.785$. The wavenumber of the waves in the channel centre-plane is $k \approx 2$, hence the wave fluctuations are suppressed. The filtered quantity should be close to the r.m.s. value of w and is loosely referred to as the r.m.s. value of w in this thesis. This method was used by Henningson *et al.* (1991) to find the r.m.s. value of the normal velocity inside a turbulent spot in plane Poiseuille flow.

The contours of the r.m.s. value of w at $z = 0$ and $t = 55$ are shown in Figure 7.3 (a). We notice that there is a maximum r.m.s. value on each side of the line of symmetry ($y = 0$), represented by the peaks in Figure 7.3 (a). We will call this peak the r.m.s. amplitude of the wave group. The true amplitude of the envelop bounding the wave group should be larger than the r.m.s. amplitude. Contours of the r.m.s. values of w are plotted for other instances t and the r.m.s. amplitudes are measured. Hence, we obtained a measure of the growth of the whole wave group. The r.m.s. amplitude *vs.* time is plotted in Figure 7.3. Initially, with both symmetric and antisymmetric forcing, the wave group shows exponential growth. After the antisymmetric forcing is switched off, the r.m.s. amplitude drops a little and then rises approximately exponentially from

about $t = 15$ to $t = 35$. Eventually, the r.m.s amplitude settles to a value of about 0.1. Between $t = 15$ and $t = 35$, the growth rate is about 0.045. Figure 8.(a) of Henningson (1989) showed the growth of wave action along two rays defined by group-velocities in the wave area outside the spot, from which the growth rates can be estimated by measuring the slope of the growth curve. These are found to be about 0.12 for the inner ray and 0.08 for the outer ray. Since the wave action is proportional the square of the wave amplitude, the growth rates of the wave amplitude are 0.06 and 0.04 for the inner and outer rays, respectively. The present result of 0.045 for the growth rate agrees with Henningson (1989) in order of magnitude. The Reynolds number in Henningson (1989) was larger (1500) than that used in the present calculation (1000). This may partially explain the difference in the growth rates. If the position, x_p, of r.m.s. peak is followed downstream, we will find that x_p lies close to a straight line with a slope of about 0.17 in a position-time plot. The reference frame is travelling at speed $c_s = 0.6$, therefore $dx_p/dt \approx 0.77$.

In order to measure the spreading of the wave group with time, we take the 2 % contour of the r.m.s. w as the boundary of the wave group. We measure the streamwise positions of the front and the rear of the wave group $x_f(t)$ and $x_r(t)$, respectively, and the spanwise position of the side of the wave group $y_s(t)$. The results are shown in Figure 7.3. We can see that, between $t = 30$ and $t = 55$ [1], x_f and y_s change linearly with slopes of about 0.24 and 0.13, respectively. The rear position $x_r(t)$ does not behave as well, but varies between -3 and -2. If a straight line is draw to approximate $x_r(t)$, the slope of this line is about 0. Since the reference frame is travelling with streamwise

[1]Results for $t > 55$ is discussed in the next section

speed $c_s = 0.6$, therefore $dx_f/dt = 0.84$ and $dx_r/dt = 0.6$ in a fixed frame. dy_s/dt is still 0.13 since the reference frame does not travel spanwise. Figure 5 of Alavyoon *et al.* (1986) indicated that, at $Re = 1000$, dx_f/dt should be about 0.75 and dx_r/dt about 0.65 for a turbulent spot. The present strong wave group is apparently spreading at a larger rate. Two possible reasons account for the difference between the present calculation and the results of Alavyoon *et al.* (1986). Firstly, the present "spot" is not turbulent, but a group of strong laminar waves. Secondly, the positions x_f and x_r are measured at $t < 100$, during which the spot travels a distance of about 60 downstream, whereas in Alavyoon *et al.* (1986) the measurements were made at downstream distances of well above 100.

We can apply the filtering function given by (7.1) and (7.2) to the Fourier transform of the streamwise velocity u (not its root square) to suppress the wave fluctuations and obtain the mean streamwise velocity. Figure 7.3 (b) shows contours of the mean u-velocity (not the perturbation) in the centre-plane $z = 0$ at $t = 55$ with the r.m.s. value of w shown in 7.3 (a). The u-contours look like those of streamwise mean velocity in Figure 1 (b) of Henningson *et al.* (1991). The regions of increased u are clearly seen out side of the strong wave region. These regions of increased u are not close to the modelled forcing, which is located at (0,0) in the xy-plane, therefore the strong waves must be chiefly responsible for creating these regions. This, incidentally, shows that the laminar modifications to the mean flow outside the turbulent spot in plane Poiseuille flow are insensitive to the detailed turbulence inside the spot since the strong laminar waves in the present calculation also produce the same kind of modifications to the mean flow.

7.3 Breakdown of finite amplitude waves

In the last section we have seen that the wave crests appear to reach some neutrally stable state. No breakdown of the waves is observed. The following calculations may give some interesting insight to the relationship between wave breakdown and turbulent spot growth.

The computation described in the last section is started at $t = -30$ with $Re = 1000$, $c_s = 0.6$, $c_1 = 0.1$ and $c_2 = 0.05$. Having created the initial waves, the antisymmetric forcing is switched off at $t = 0$ to allow the waves to develop freely in the flow field modified by the presence of the symmetric forcing. Finite amplitude waves initially grow and then reach some neutrally stable state without breakdown. This computation is continued to $t = 55$ (Figure 7.2). We now also switch off the symmetric forcing at $t = 55$ and observe what follows. The flow is now completely free of any assumed inhomogeneity. The large amplitude waves created between $t = 0$ and $t = 55$ as a result of the destabilization of the flow field are allowed to develop. Almost immediately, these waves begin to break down to smaller scale structures – little islands in the contour plots (Figure 7.7)[2]. The breakdown starts near the origin $(x, y) = (0, 0)$ and extends gradually into surrounding regions.

In order to show that the breakdown is due to the removal of the forcing at $t = 55$, we run another case. With $Re = 1000$, $c_s = 0.6$, $c_1 = 0.1$ and $c_2 = 0.05$ just like in

[2]Use of the word "turbulence", is avoided here since the resolution of the present computation is too low to represent most of turbulent scales.

the last section, the flow is started at $t = -30$. At $t = 0$, both symmetric forcing and antisymmetric forcing are switched off. The resulting wave packet grows in a similar fashion to that in the last section. At $t = 40$, the wave packet starts to break down to smaller scale structures.

It seems from the two runs above that wave breakdown occurs only after the assumed forcing is switched off. The presence of the symmetric forcing appears to stablize the finite amplitude waves, *i.e* to prevent or at least to delay the breakdown of the finite amplitude waves. More detailed analysis is needed to understand the breakdown process. However, some qualitative arguments may give a few clue as to what caused the breakdown. We notice that the breakdown occurs along the wave crests, much like the secondary instability analyzed by Orszag and Patera (1983). We will therefore convert the present three-dimensional problem into a quasi-two-dimensional one and then use the secondary instability theory of Orszag *et al.* (1983) to outline a possible explanation for the breakdown.

Supposing we focus on a local region in the xy-plane over one wavelength, we can consider the local properties of the waves. The mean flow is three-dimensional, having both streamwise and spanwise mean velocities and the waves are very oblique. Henningson *et al.* (1989) showed that such a flow can be treated as a two-dimensional flow with mean velocity,

$$U(z) + V(z)\tan\phi, \tag{7.3}$$

where $U(z)$ and $V(z)$ are the local streamwise and spanwise mean velocities, respec-

tively. ϕ is the wave oblique angle. The stability of linear waves can be analyzed by inserting (7.3) into the Orr-Sommerfeld equation as the velocity of the basic flow. An unperturbated plane Poiseuille flow is driven by the constant pressure gradient, $-2/Re$, whereas the flow (7.3) is driven by both the pressure gradient, $-2/Re$ and the modelled Reynolds stress. We re-normalize the problem so that the maximum value of the mean velocity (7.3) is one and the Reynolds number is re-defined accordingly. This growth of the small amplitude waves suggests that the quasi-two-dimensional flow (7.3) is linearly unstable to two-dimensional disturbances. The fact that the amplitudes of these waves eventually settle to some finite value indicates the existence of a stable neutral solution. As analyzed by Orszag *et al.* (1983), two-dimensional finite amplitude waves are susceptible to three-dimensional secondary disturbances along the wave crests. Whether a primary wave of wavenumber α is unstable to secondary disturbances depends on the Reynolds number and the amplitude of the primary wave. Figure 7 in Orszag *et al.* (1983) showed the growth rate contours of the secondary instability for plane Poiseuille flow. This figure cannot be used to study the secondary instability of the primary waves in the present problem since the flow (7.3) is not a plane Poiseuille flow. However, Orszag *et al.* (1983) pointed out that the secondary instability in different flows had many common characters —the universality of the secondary instability. Therefore, for a qualitative discussion, we will assume that the secondary instability contours in the Reynolds number-amplitude plane for the present problem are similar in shape to those for plane Poiseuille flow. Figure 7.8 shows a schematic drawing of the secondary instability boundary in the $Re - A$ plane, A being the amplitude of the primary wave normalized with the maximum value of the mean velocity (7.3).

Before the removal of the modelled Reynolds stress, the primary waves do not break down. The "state" of the flow, (Re_1, A_1), is outside the region of secondary instability, indicated by the dot in Figure 7.8. We now observe, from the numerical calculations, what happens to the mean flow and the primary waves after the modelled Reynolds stress forcing is switched off. The streamwise and spanwise mean velocity profiles are examined and no significant differences are found before and after the on-set of the breakdown except some changes in amplitudes. The streamwise mean velocity $U(z)$ is found to increase near the channel centre and decrease near the walls — a consequence of the removal of the "Reynolds stress". The spanwise velocity $V(z)$ decreases over the whole channel depth. Because of the breakdown, measuring (numerically) the amplitude of each wave crest is difficult. However, the waves which have not yet broken down do not show any appreciable change in amplitudes before and after the forcing is switched off and so we will assume that the primary wave amplitude is constant with respect to time. Since the change in amplitude of the mean flow is slow, we assume the mean flow is quasi-steady. At each instance the mean flow is different and so the secondary instability boundary sketched in Figure 7.8 will, in general, change with time, but its shape will remain similar, therefore we will use only one boundary in Figure 7.8. In any case, this should not affect the qualitative analysis given below.

The amplitude of the quasi-two-dimensional mean flow given by (7.3) can either increase or decrease depending on the relative rate of change of $U(z)$ and $V(z)$. An increase in the amplitude of the mean flow represents an increase in the Reynolds number and a decrease in the relative amplitude, A, of the primary wave since constant amplitude primary wave must be re-normalized with a larger amplitude of the mean

flow and hence the relative amplitude decreases. A decrease in the amplitude of the mean flow has the opposite effect. Both cases could result in the migration of the flow "state", (Re, A), across the secondary instability boundary shown in Figure 7.8. The latter case (indicated by the arrow marked 2 in Figure 7.8) is more likely to be what actually occurs. Orszag *et al.* (1983) showed that the energy is transferred from the mean flow to the secondary waves with the primary wave acting as a "catalyst". The energy transfer from the primary wave to secondary waves is very small. In the present problem, the reduction to the amplitude of the mean flow could imply the loss of energy to the secondary waves as well as to dissipation.

The scenario given in this section is not a proof, but offers a simplified sketch of a possible mechanism by which the wave breakdown occurs after the removal of the modelled Reynolds stress forcing. The point to be stressed is that the changes in the mean flow, the relative amplitude of the primary wave and the secondary instability boundary are such that the "state" of the flow moves inside the region of secondary instability. More analysis is needed before this is fully understood. A plausible way to tackle this problem would be to use the analysis of Orszag *et al.* (1983), with a two-dimensional mean flow driven by not only a constant pressure gradient, $-2/Re$, but also some kind of body force, $F(z)$, that would produce mean velocity profiles similar to those in the wave breakdown region. For example, $F(z) = 12az^2/Re$, together with $-2/Re$, wound produce a mean flow $U(z) = 1 - a - z^2 + az^4$. After the body force is removed, we could follow the changes in the mean flow, the primary wave and the secondary waves to see if the scenario discussed above is true. However, this is outside of the scope of the present thesis and is left to future studies.

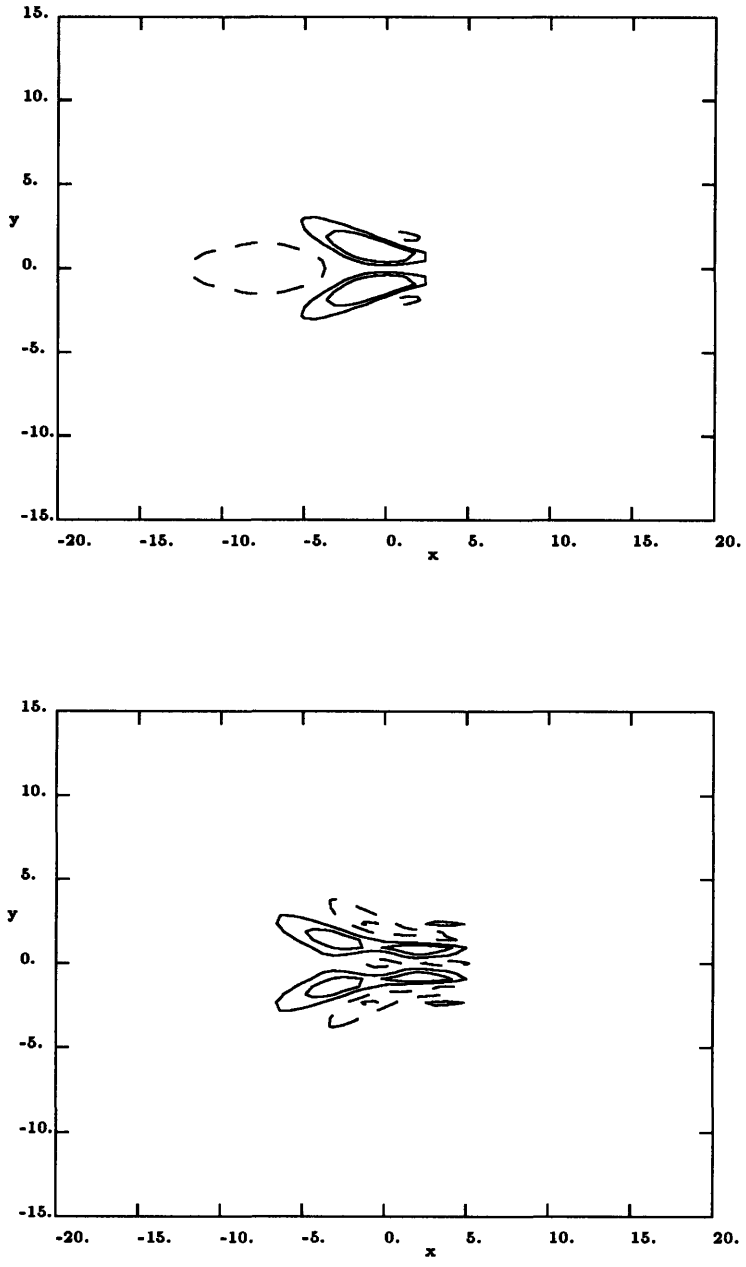

Figure 7.1: Contours of w in unmodified flow field. $Re = 1000$, $c_1 = 0$. Contours are $w = -0.02$, -0.01, 0.01 and 0.02. (a) $t = 10$, (b) $t = 20$.

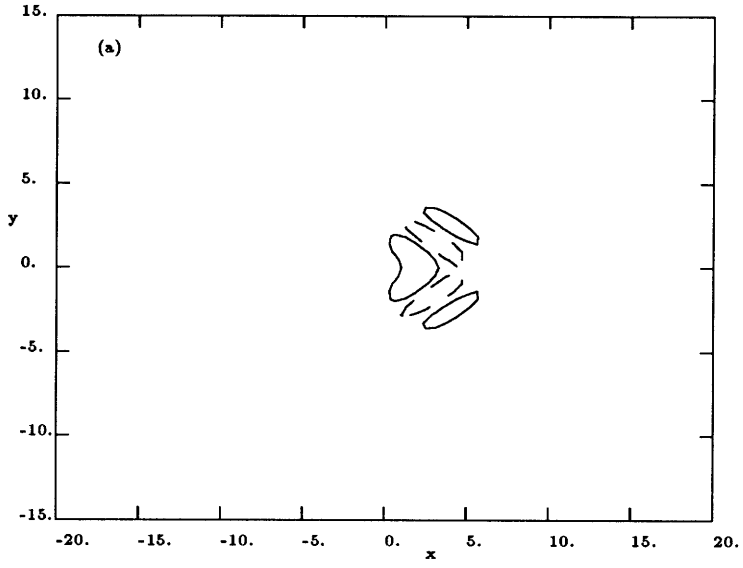

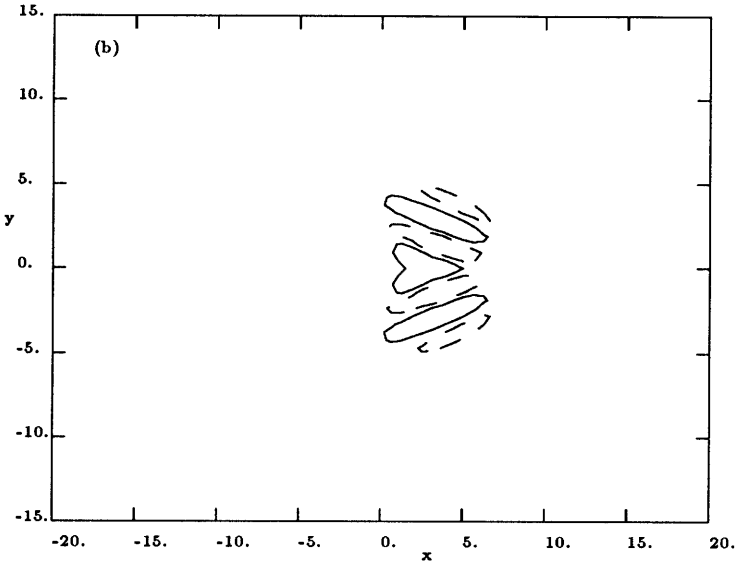

see next page for caption

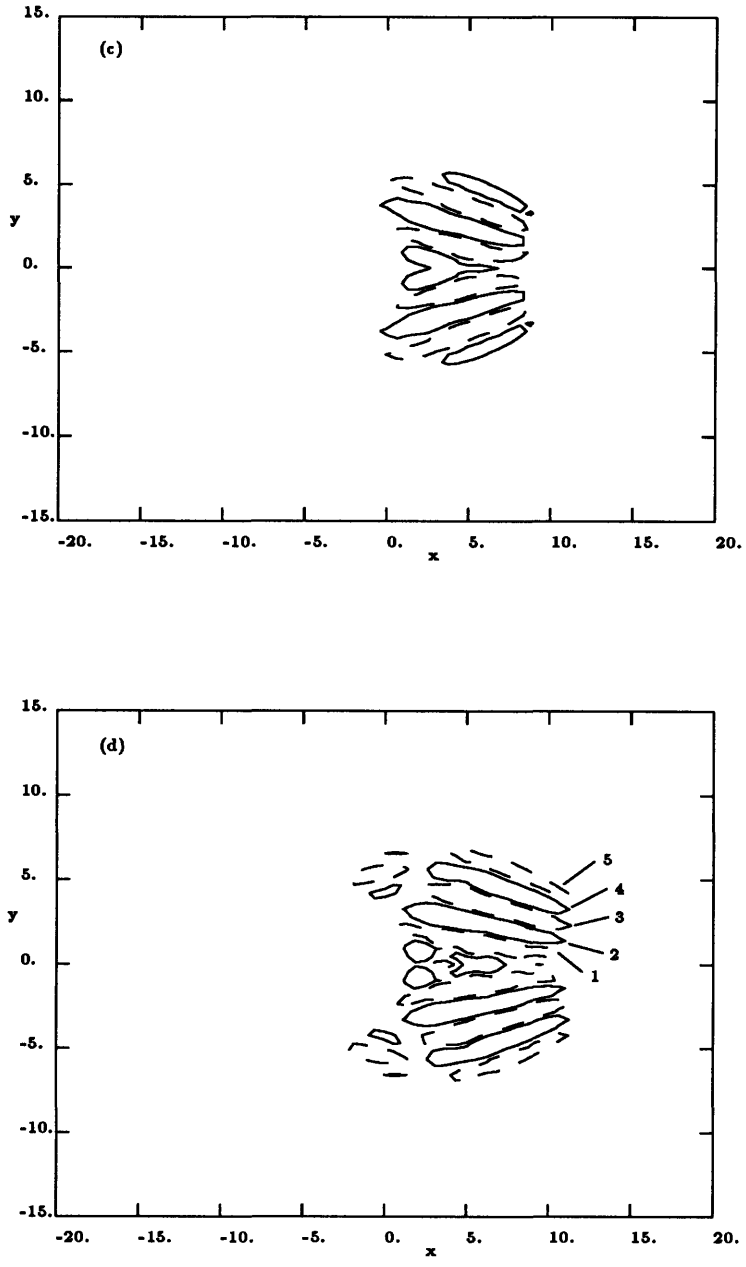

Figure 7.2: Contours of w. $Re = 1000$, $c_1 = 0.1$, $c_s = 0.6$. Contours plotted are $w = -0.02$ and $w = 0.02$. (a) $t = 0$, (b) $t = 10$, (c) $t = 20$ and $t = 30$.

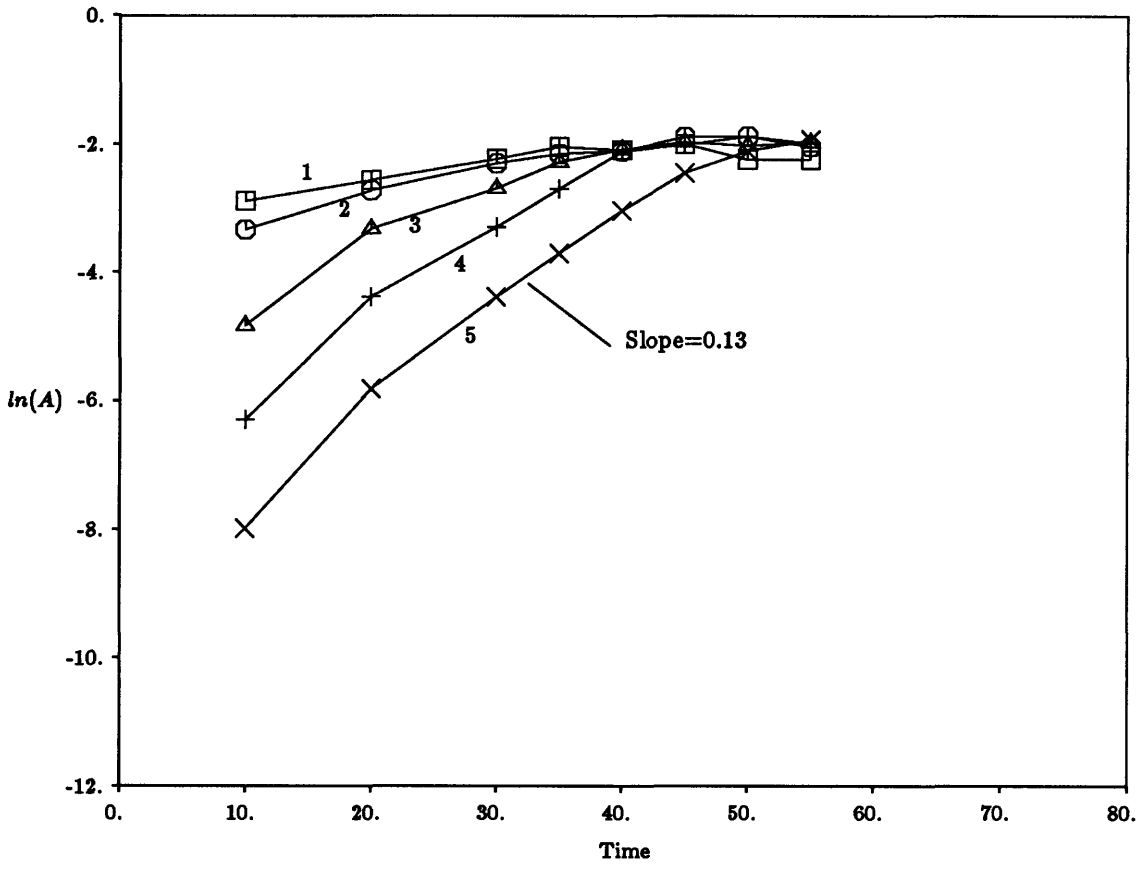

Figure 7.3: Amplitudes of wave crests as functions of time. Numbers 1 to 5 indicate different waves crests shown in the figure of the previous page

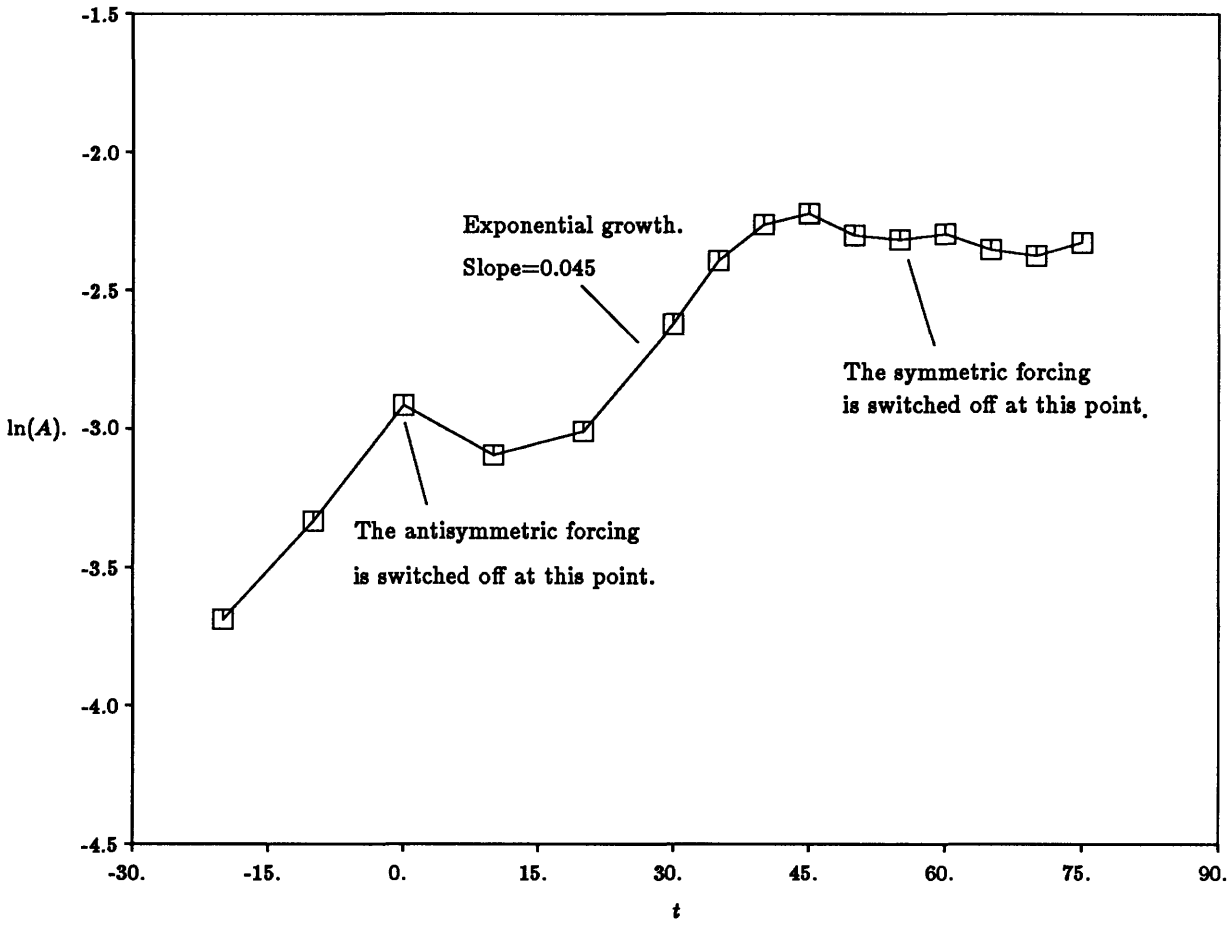

Figure 7.4: The r.m.s. amplitude of w as a function of time

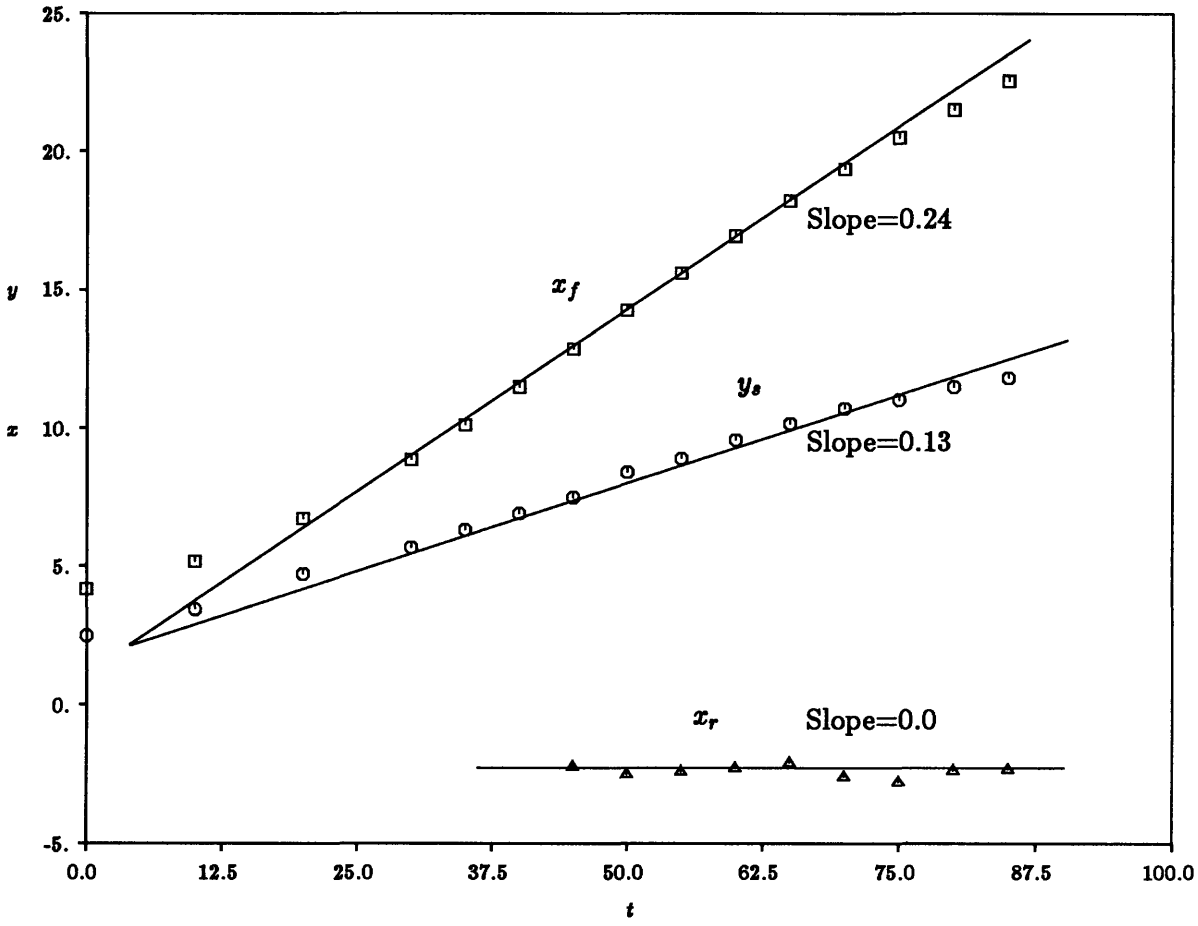

Figure 7.5: Spreading of the strong wave group. □: front, ○: side and △: rear

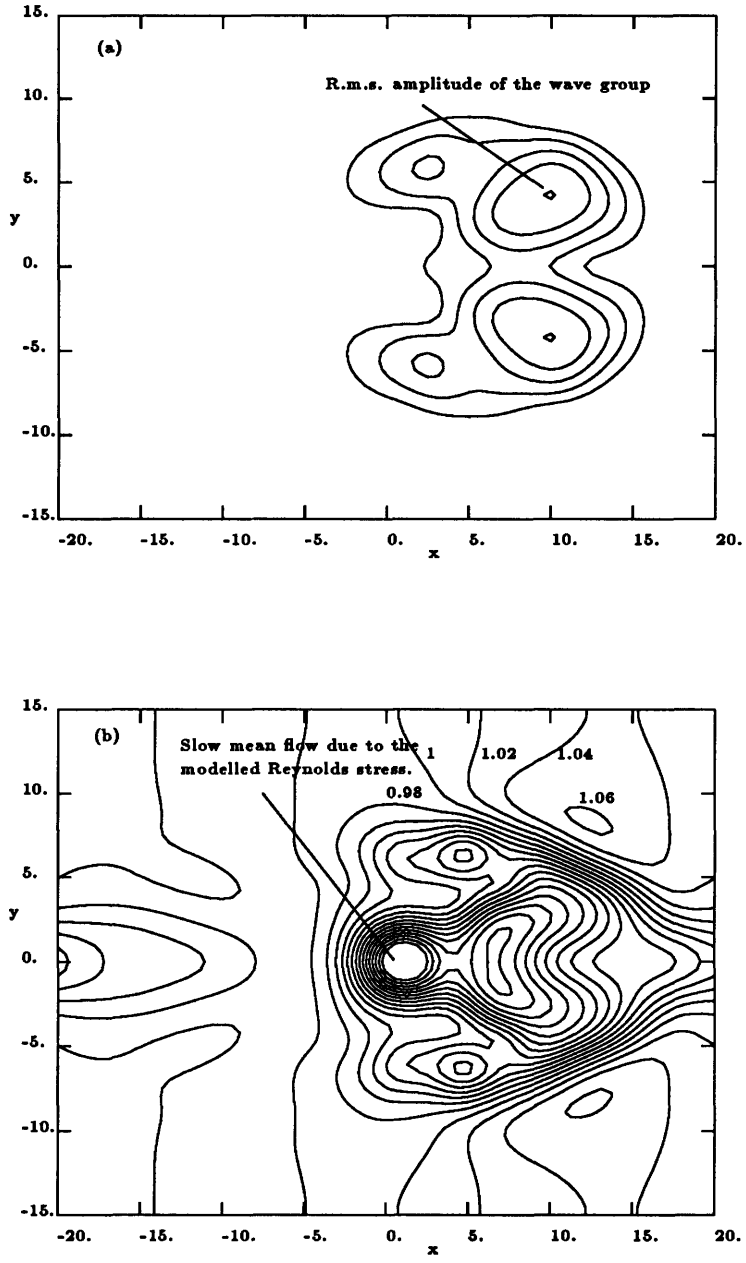

Figure 7.6: $z = 0$, $t = 55$. (a) R.m.s. value of w. Lowest contour value=0.02, highest=0.10, incr=0.02. (b) Streamwise mean velocity. Lowest contour=0.7, highest 1.06, incr=0.02

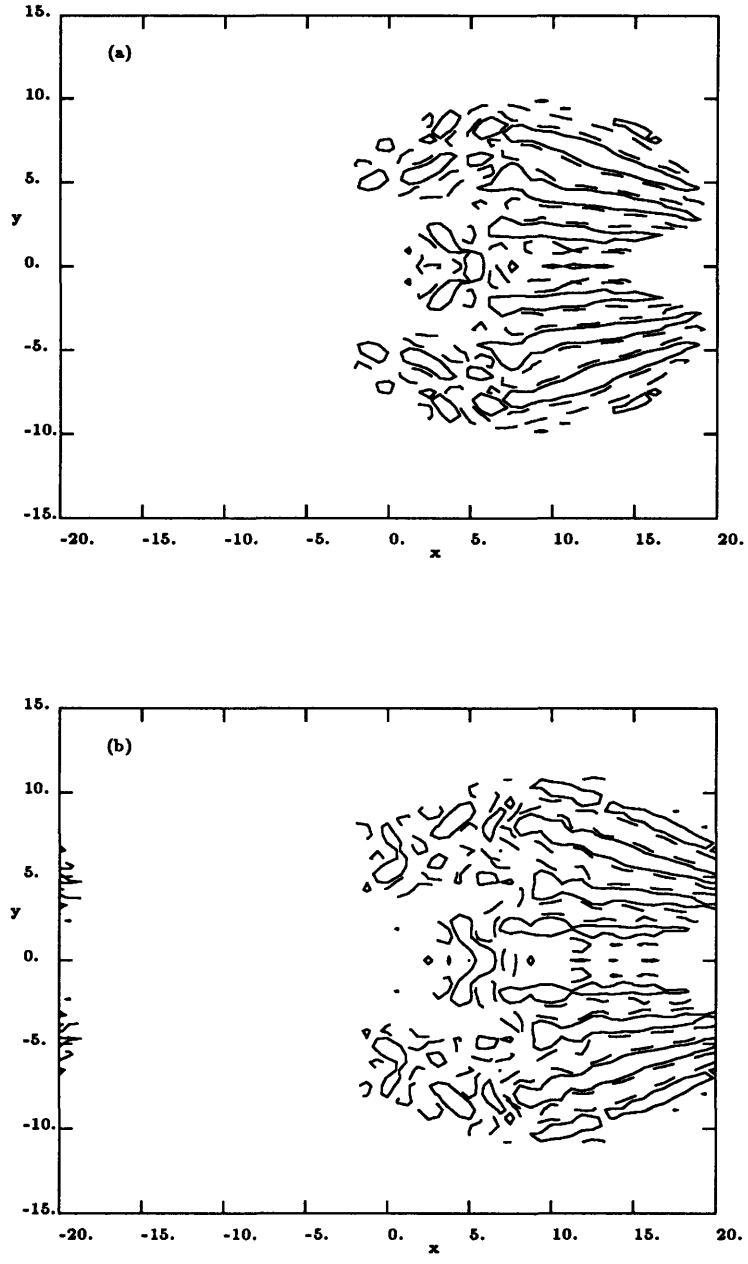

Figure 7.7: Contour plots of normal velocity, w. The symmetric forcing is turned off at $t = 55$ and wave breakdown begins. (a) $t = 70$, (b) $t = 80$.

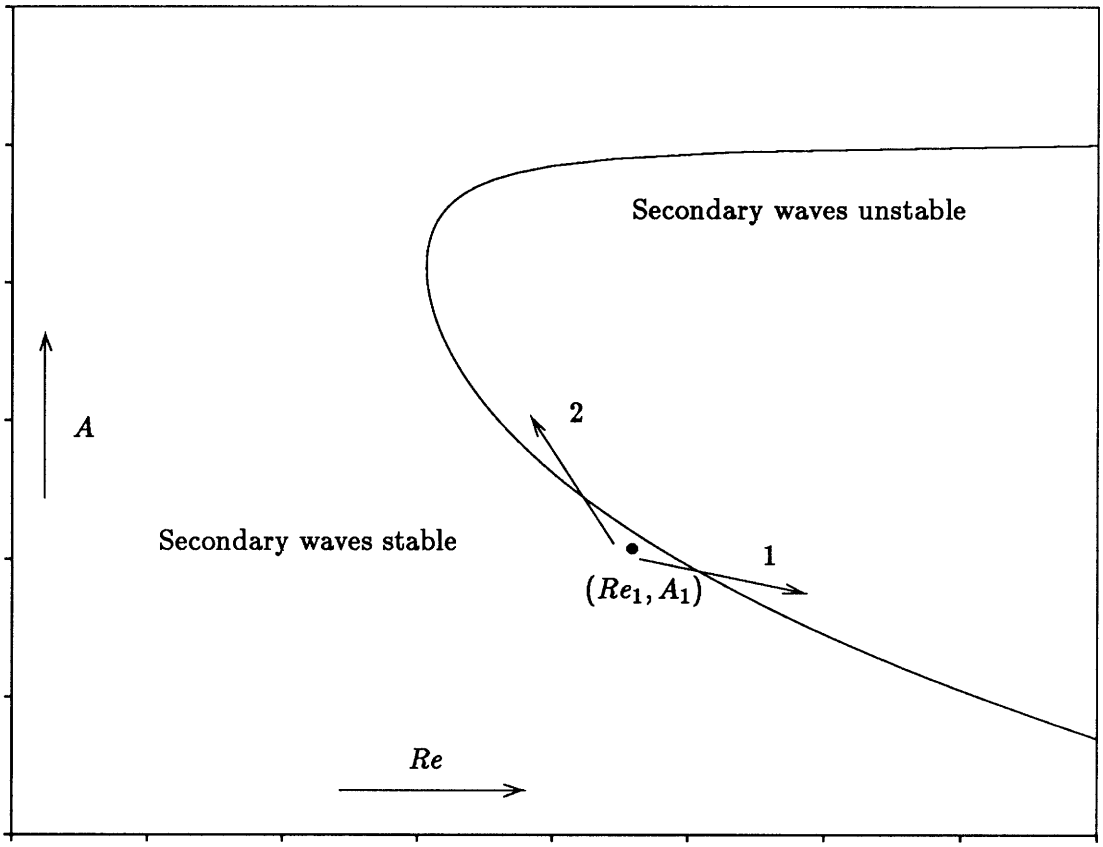

Figure 7.8: Migration of the flow "state", (Re, A), into the unstable region from the original stable "state", (Re_1, A_1). The solid curve is the secondary instability boundary. In the direction marked 1, Re increases accompanied by a decrease in A. In direction 2, Re decreases and A increases

.

Chapter 8

Conclusions and Further Discussions

The mechanisms of the growth of a turbulent spot in a plane Poiseuille flow at a Reynolds number of 1000 have been considered by modelling the spot as a concentrated region of Reynolds stress. Efforts have been made to analyze how the mean flow in a channel is destabilized and what perturbation modes contribute most to the modified velocity field. The results indicate that the turbulent spot acts as a patch of inhomogeneity forcing large scale modifications and hence destabilizing to the surrounding laminar flow.

8.1 Linear free waves in plane Poiseuille flow

At Reynolds numbers much lower than the linear critical Reynolds number of 5772, all linear perturbations eventually decay with time. At $Re = 1000$, it has been found that the perturbations to the normal velocity, w, develop into a decaying wave packet after the initial perturbation, while the perturbations to the streamwise velocity, u, intensifies for a relatively long time before they finally decay, indicating that near resonance between the normal velocity and the normal vorticty may be present (see Henningson,

1990). Along the line of symmetry ($y = 0$) the streamwise perturbation lengthens considerably, which is consistent with the algebraic instability theory of Landahl (1980).

"Pure" waves of infinite extent with a single absolute wavenumber and oblique angle are also examined. The following facts characterize their behaviour at subcritical Reynolds numbers:

- For 2-dimensional waves at Reynolds numbers just below the critical value of 5772, there exist a wave at a particular wavenumber that is least damped. Following some 2-dimensional initial disturbance consisting of a range of wavenumbers, this preferred wave decays slowest and will eventually dominate the perturbation flow field. As the Reynolds number is lowered to below about $Re = 4745$, this preferred wave is lost and the long waves with wavenumbers close to 0 are less stable.
- For 3-dimensional oblique waves at Reynolds number just below the critical value, the preferred wave is the same as that in the 2-dimensional case. However, as the Reynolds number is lowered to below about 4810. Another wave of 90 degree oblique ange and absolute wavenumber of about 1.2 takes over as the least stable wave.

This means that, at $Re = 1000$, the preferred wave has streamwise wavenumber, $\alpha = 0$, and spanwise wavenumber, $\beta \approx 1.2$.

For an initial disturbence in the form of a cross-stream ($\alpha = 0$) wave at a Reynolds

number Re, the spanwise velocity v and normal velocity w will decay right away, while the streamwise perturbation velocity, u, will grow for a duration of about $0.113Re$ non-dimensional time unit before decaying, *i.e* even at Reynolds numbers as low as 1000, the growth will persist for a duration of about 100 non-dimensional time unit, a consequence of the algebraic instability (Landahl, 1980).

8.2 Mean flow modifications

When the modelled turbulent spot is introduced into a plane Poiseuille flow, the mean velocity field is modified. The perturbation flow field consists mainly of the first few eigenmodes of the normal vorticity equation. These modes are damped ones which would normally decay with time in a flow field free of inhomogeneities. However, the turbulent spot acts as a region of inhomogeneity and forces these large scale normal vorticity modes to grow, leading to the destabilization of the mean flow field.

In agreement with the numerical simulation and analysis of Henningson (1989), the modified flow field outside the modelled turbulent spot is characterized highly inflexional spanwise profiles. These regions can be considered as consisting of the eigenmodes of the normal vorticity equation. The flow field modifications near the centre-plane of the channel is mainly attributted to the fast $s1$ mode whose maximum amplitude is at the centre. The the other slower modes contribute the the flow field modifications near the walls. Among them, the $s2$, $s3$ and $s3$ modes are important because they are relatively lightly damped in the viscous channel flow. When an inhomogeneity travelling with

speed c_s, such as the modelled turbulent spot, is present in the flow field, it forces different eigenmodes to grow. The dominant mode has phase speed, $\mathrm{Re}(c) = c_s$, *i.e* if the forcing travels with the phase speed of Mode s1, the perturbation to the mean flow is mainly due to Mode s1 as a result of near-resonance, and the same applies to other modes. This is demonstrated by making the modelled turbulent spot travel at different, prescribed speeds. The faster the forcing travels, the stronger the perturbation at the channel centre-plane and the weaker the perturbation away from the centre-plane.

8.3 Growth of oblique waves riding on the large scale modifications to the mean flow

When the large scale mean flow is modified by the presence of an turbulent spot, some parts of the flow field is destabilized and small perturbations will grow there. When an antisymmetric disturbance is introduced for a short time, smaller scale, growing oblique waves start to develop in the destabilized regions. These waves always appear to ride on the slower moving regions of the large scale disturbance. When the spot is made to travel very fast, say at speed $c_s \approx 1$, the amplitudes of the slower modes will reduce, and so will the wave growth. This may be an explanation as to why the turbulent spot fronts travel at a speed less than 0.8.

The wavelength and oblique angles agree well with existing experiments and numerical simulations. When the forcing travels at speed, $c_s = 0.6$, waves in the destabilized regions have wavenumber, k, ranging from 1.5 to 2.1 and oblique angles ranging from

55 to 72 degrees. Henningson (1989) showed waves have $k = 1.88$ at oblique angle of about 68 degrees in the most unstable region.

Increasing the Reynolds number from, $Re = 1000$, to, $Re = 2000$, only slightly changes that large scale perturbations. The amplitudes of the waves on each side of the forcing increase with Reynolds number.

In the case of small scale finite amplitude waves riding on the large scale perturbation to the mean flow with the forcing travelling at speed, $c_s = 0.6$, the wave group amplitude grows approximately exponentially, and then settle to a value of about 10 percent of the unperturbed maximum free stream velocity. This is a consequence of the modelling of the turbulent spot. Recall that the spot is modelled as a non-spreading region of increased Reynolds stress, which distorts the surrounding laminar flow and causes instability to set in. Hence, the regions under the influence of the modelled spot is limited to the neighbourhood of the modelled spot. If, somehow, the spreading of the spot were incorporated into the model, the destabilized regions would be continuously extended into the surrounding flow, causing the a succession of newly generated waves crests to appear.

It has been found that, with the modelled spot in the flow field, the waves riding on the large scale perturbations to the mean flow do not break down. As soon as the modelled spot is removed from the flow field, the breakdown of waves into smaller scales starts. A possible explanation of the breakdown is that the changes in the mean flow

and primary wave moved the "state" of the flow into the region of secondary instability.

8.4 Advantages and disadvantages of using the modelled spot

Modelling the spot as a region of increased Reynolds stress has the advantage of saving computer time. A full Navier-Stokes simulation would require very fine computational grids and, given the large size of a turbulent spot, large number of spectral modes would have to be used in order to resolve the small scale turbulence within the turbulent spot. In their numerical simulation of the turbulent spot, Henningson *et al.* (1987) used $256 \times 256 \times 33$ spectral modes. In the present work, our aim is to analyze the laminar wave field outside the turbulent spot and, with the model discussed in this thesis, relatively few spectral modes are used ($64 \times 64 \times 33$). Computational results of wave field and mean flow modifications showed good agreement with existing numerical simulations (see Henningson *et al.* (1987)), especially at the early stages of the development of the wave packets.

Furthermore, the modelled spot can be made to travel at prescribed speeds to distort the mean flow to various degrees. This enables us to find that the slower modes are most likely to be responsible for the destabilization of the flow field outside the turbulent spot and hence speculate the reasons why the spot front and rear travel at certain speeds at fixed Reynolds numbers.

The very fact that relatively few spectral modes are used in the computations has also disadvantages. Given a fixed number of spectral modes, the fineness of the grids is inversely proportional to the size of computation "box" (*i.e* the length and width of the computational domain). There two scales involved in the computations: (i) the large scale modifications to the mean flow, (ii) the small scale wave field. To resolve the wave field, we need a small computational domain, but will poorly represent the large scale mean flow modifications since the large scale flow may not have negligible amplitudes at the edges of the box. This can cause instabilities which initiates from the edges of the box and propagate into the inner regions of the box. Conversely, if a large box is used, the mean flow modifications are well represented, but the small scale waves can not be resolved. In the present work with $64 \times 64 \times 33$ spectral modes and a computational box of $40 \times 30 \times 2$, the computational can be continued to about $70 - 80$ nondimensional time units after the symmetric forcing is swiched on without significant stability and resolution problems. Increasing the number of modes is the obvious solution in the expense of comutational time.

Appendix A

Approximations to the integrals

In chapter 5, we made the following approximations for large t,

$$I_1 = \int_0^t q_j(\tau) e^{i\alpha(c_j - c_s)\tau} d\tau \approx q_j(t) \int_0^t e^{i\alpha(c_j - c_s)\tau} d\tau, \tag{A.1}$$

$$I_2 = \int_0^t r_j(\tau) e^{i\alpha(c_j - c_s)\tau} d\tau \approx r_j(t) \int_0^t e^{i\alpha(c_j - c_s)\tau} d\tau, \tag{A.2}$$

where $q_j(t)$ and $r_j(t)$ are, respectively,

$$q_j(t) = \int_{-1}^{1} \Phi_j(z)(-i\alpha\hat{p}_2 - \hat{w}U'(z))dz, \tag{A.3}$$

$$r_j(t) = \int_{-1}^{1} \Phi_j(z)(-i\beta\hat{p}_2)dz. \tag{A.4}$$

We will show that the approximation made in Equation (A.2) has an error whose magnitude at large t decays faster than or equal to $O(te^{-at})$, where a is a positive constant. The proof for (A.1) can be done similarly. In order to do so, we need to find the expression for $r_j(t)$ by solving the relevant equations analytically. The relevant equations are,

$$\frac{\partial}{\partial t}(D^2 - k^2)\hat{w} + i\alpha[U(D^2 - k^2) - \frac{d^2U}{dz^2}]\hat{w} - \frac{1}{Re}(D^2 - k^2)^2\hat{w} = i\alpha\frac{\partial^2\widehat{u'w'}}{\partial z^2}, \tag{A.5}$$

$$D^2\hat{p} - k^2\hat{p} = -2i\alpha\hat{w}\frac{dU}{dz} - i\alpha\frac{\partial\widehat{u'w'}}{\partial z}, \tag{A.6}$$

where α and β are, respectively, the streamwise and spanwise wavenumbers, $k^2 = \alpha^2 + \beta^2$, $D = \partial/\partial z$, $\hat{w}$ is the Fourier transform of w, and $\hat{p}$ is the Fourier transform of p.

The boundary conditions at the walls are,

$$\hat{w}(\alpha, \beta, \pm 1, t) = \frac{\partial \hat{w}}{\partial z}(\alpha, \beta, \pm 1, t) = 0, \tag{A.7}$$

$$\frac{\partial \hat{p}}{\partial z}(\alpha, \beta, \pm 1, t) = \frac{1}{Re}\frac{\partial^2 \hat{w}(\alpha, \beta, \pm 1, t)}{\partial z^2}. \tag{A.8}$$

We express $\hat{w}$ as the sum of the eigenfunctions, $\{\phi_m(z)\}$, of the Orr-Sommerfeld equation,

$$\hat{w} = \sum_{j=0}^{\infty} H_m \phi_m. \tag{A.9}$$

By substituting (A.9) into (A.5) and making use of the orthogonality relation for the Orr-Sommerfeld equation [1], we obtain the solution for $H_m(t)$ subject to the condition that there are no perturbations at time, $t = 0$,

$$H_m = \frac{E_m}{(c'_m - c_s)}(1 - e^{-i\alpha(c'_m - c_s)t}), \tag{A.10}$$

where $E_m = \int_{-1}^{1} \phi_m^{\dagger}(z)\partial^2(\widehat{u'w'})/\partial z^2$. and c'_m is the eigenvalue corresponding to the eigenfunction ϕ_m.

[1] If ϕ_m is the eigenfunction of the Orr-Sommerfeld equation, then $\int_{-1}^{1} \phi_m^{\dagger}(z)(D^2 - k^2)\phi_n(z)dz = \delta_{mn}$, where $\phi_n^{\dagger}$ the is eigenfunction of the differential equation adjoint to the Orr-Sommerfeld equation, corresponding to ϕ_n. See Drazin & Reid (1982).

Since $r_j(t)$ in Equation (A.2) is related to the time-dependent part of the solution for the pressure (see Chapter 5), we will find the solution for p_2 only, *i.e*,

$$D^2\hat{p}_2 - k^2\hat{p}_2 = -2i\alpha\hat{w}\frac{dU}{dz}. \tag{A.11}$$

We let $P_m(z)$ be the solution to the following equation,

$$D^2\hat{P}_m - k^2\hat{P}_m = -2i\alpha E_m\phi_m\frac{dU}{dz}, \tag{A.12}$$

subject to boundary conditions,

$$\frac{\partial P_m}{\partial z}(\alpha,\beta,\pm1,t) = \frac{1}{Re}E_m\phi_m''(\pm1). \tag{A.13}$$

It is easy to see, from (A.8), (A.9) and (A.10), that,

$$\hat{p}_2(\alpha,\beta,z,t) = \sum_{m=1}^{\infty}\frac{P_m(z)}{c_m^l - c_s}(1 - e^{-i\alpha(c_m^l - c_s)t}). \tag{A.14}$$

From Equation (A.4), we obtain

$$r_j(t) = \sum_{m=1}^{\infty}\frac{S_{jm}}{c_m^l - c_s}(1 - e^{-i\alpha(c_m^l - c_s)t}), \tag{A.15}$$

where $S_{jm} = \int_{-1}^{1} -i\beta P_m(z)\Phi_j(z)dz$, Φ_j being the eigenfunction of the normal vorticity equation.

Substituting Equation (A.15) into Equation (A.2), we get,

$$I_2 = \int_0^t r_j(\tau)e^{i\alpha(c_j - c_s)\tau}d\tau. = \sum_{m=0}^{\infty}S_{jm}\int_0^t\frac{(1 - e^{-i\alpha(c_m^l - c_s)\tau})}{c_m^l - c_s}e^{i\alpha(c_j - c_s)\tau}d\tau. \tag{A.16}$$

Upon integration and factorizing some terms, we get,

$$I_2 = \frac{e^{i\alpha(c_j - c_s)t} - 1}{i\alpha(c_j - c_s)} \times \sum_{m=0}^{\infty}S_{jm}[\frac{1 - e^{-i\alpha(c_m^l - c_s)t}}{c_m^l - c_s} + \frac{e^{-i\alpha(c_m^l - c_s)t}}{c_m^l - c_s}](1 - \epsilon_{jm}), \tag{A.17}$$

where

$$\epsilon_{jm} = \frac{c_j - c_s}{c_j - c'_m} \times \frac{e^{-i\alpha(c'_m - c_s)t} - e^{-i\alpha(c_j - c_s)t}}{1 - e^{-i\alpha(c_j - c_s)t}}. \tag{A.18}$$

By comparing Equation (A.17) with Equation (A.15), we can show that

$$I_2 = r_j(t) \int_0^t e^{i\alpha(c_j - c_s)\tau} d\tau \times (1 + \frac{1}{r_j(t)} \sum_{m=1}^{\infty} S_{jm} \frac{e^{-i\alpha(c'_m - c_s)t} - \epsilon_{jm}}{c'_m - c_s}) \tag{A.19}$$

The first term in the summation tends to zero exponentially for large t, since $\mathrm{Im}(c'_m)$ is negative at $Re = 1000$. For the second term to vanish, we need to show that $\epsilon_{jm} \to 0$ for large t. At $Re = 1000$, both c_j and c'_m have negative imaginary parts. Therefore, from Equation (A.18), we see that $\epsilon_{jm} \to 0$ for large t if $c_j \neq c'_m$. When $c_j = c'_m$, the expression for ϵ_{jm} becomes,

$$\epsilon_{jm} = (c_j - c_s) \frac{i\alpha t e^{-i\alpha(c_j - c_s)t}}{1 - e^{-i\alpha(c_j - c_s)t}} \tag{A.20}$$

Gustavsson (1981) analyzed the resonant growth of three-dimensional disturbances in plane Poiseuille flow. He found that $c_j = c_m$ occurs only at discrete points in the $k - \alpha Re$ plane. We are mainly interested in the first three even modes of the normal vorticity equation, *i.e* $s1$, $s2$ and $s3$ as explained in Chapter 5. Gustavsson (1981) found that, at $Re = 1000$, only the $s2$ mode can resonate with the $A2$ mode of the Orr-Sommerfeld equation, and that resonance occurs at $\alpha = 0.34576$ and $k = 1.0153$ with $c_j = c_m = 0.80942 - i0.19268$, and also at $\alpha = 0.14507$ and $k = 5.7942$ with $c_j = c_m = 0.69256 - i0.57474$. In these two cases, perturbations will grow for, respectively, 15.01 and 11.99 nondimensional time units before decaying. Therefore, if t is much larger than 15.01, ϵ_{jm} as given by Equation (A.20) is small.

Hence, the approximation made in Equation (A.2) has an error whose amplitude decays faster than or equal to $O(te^{-at})$ at large t, where a is a positive constant.

References

Alavyoon, F., Henningson, D.S & Alfredsson, H. (1986). Turbulent spots in plane Poiseuille flow - flow visualization. *Phys. Fluids* **29**, 1328

Breuer, K.S. & Haritonidis, J.H. (1990). The evolution of a localized disturbance in a boundary layer. Part I *J. Fluid Mech.* in press.

Breuer, K.S. & Landahl, M.T. (1990). The evolution of a localized disturbance in a boundary layer. Part II *J. Fluid Mech.* in press.

Bullister, E.T. & Orszag, S.A. (1987). Numerical simulation of turbulent spot in channel and boundary layer flows. *J. Sci. comp.* **2**, No. 3, 263

Carlson, D.R., Widnall, S.E. & Peeters, M.F. (1982). A flow-visualization study of turbulent spots in plane Poiseuille flow. *J. Fluid Mech.* **121**, 487

Davey, A. & Reid, W.H. (1977). On the stability of stratified viscous plane Couette flow. Part I. Constant buoyancy frequency. *J. Fluid Mech.* **80**, 509

Eckelmann, H. (1974). The Structure of the viscous sublayer and the adjacent wall region in a turbulent channel flow. *J. Fluid Mech.* **65**, 439

Ellingsen, T. & Palm, E. (1975). Stability of linear flow. *Phys. Fluids* **18**, 487

Emmons, H.W. The laminar-turbulent transition in a boundary layer - Part I. *J. Aero. Sci.* **18**, 490

Fjørtoft, R. (1950). Application of integral theorems in deriving criteria of stability for laminar flows and for the baroclinic circular vortex. *Geofys. Publ., Oslo* **17**, No. 6, 1

Gaster, M. (1974). On the effects of boundary-layer growth on flow stability. *J. Fluid Mech.* **66**, 465

Gaster, M. (1975). A theoretical model of a wave packet in the boundary layer on a flat plate. *Proc. Roy. Soc.* A **347**, 271

Gaster, M. & Grant, I. (1975). An experimental investigation of the formation and development of a wave packet in a laminar boundary layer. *Proc. Roy. Soc.* A **347**, 253

Gustavsson, L.H. (1979). Initial-value problem for boundary layer flows. *Phys. Fluids* **22**, 1602

Gustavsson, L.H. & Hultgren, L.S. (1980). A resonance mechanism in plane Couette flow. *J. Fluid Mech.* **98**, 149

Gustavsson, L.H. (1981). Resonant growth of three-dimensional disturbances in plane Poiseuille flow. *J. Fluid Mech.* **112**, 253

Haritonidis, J.H. (1988). A model for near-wall turbulence. *Phys. Fluids. A*1 (2), 302

Hartman, P. (1982). Ordinary differential equations. Birkhäuser, 1982

Heisenberg, W. (1924). Über Stabilität und Turbulenz von Flussigkeitsströmen. *Ann. Phys., Lpz.* (4) **74**, 577

Henningson, D.S. (1988). The inviscid initial value problem for a piecewise linear mean flow. *Stud. Appl. Math.*, **78**, 31

Henningson, D.S. & Alfredsson, H. (1987). The wave structure of turbulent spots in plane Poiseuille flow. *J. Fluid Mech.* **178**, 405

Henningson, D.S., Johansson, A.V. & Lundbladh, A. (1990). On the evolution of localized disturbances in laminar shear flows. In *Procedings of the Third IUTAM Symposium on Laminar – Turbulent Transition*, Toulouse.

Henningson, D.S, Spalart, P.R & Kim, J. (1987). Numerical simulations of turbulent spot in plane Poiseuille and boundary-layer flow. *Phys. Fluids* **30**, 2914

Henningson, D.S. (1989). Wave growth and spreading of a turbulent spot in plane Poiseuille flow. *Phys. Fluids A* **1**, 1876

Henningson, D.S & Kim, J. (1990). On turbulent spots in plane Poiseuille flow. Accepted by *J. Fluid Mech.*

Henningson, D.S. (1991). An eigenfunction expansion of localized disturbances. In

Advances in Turbulence 3, Eds. A.V. Johansson and P.H. Alfredsson, Springer.

Herbert, T. (1977). Finite amplitude stability of plane Poiseuille flows. In *Laminar – Turbulent Transition*: *Proc. AGARD Conf. No.* 224, Lyngby, Denmark.

Herbert, T. (1983). Secondary instability of plane channel flow to subharmonic three-dimensional disturbances. *Phys. Fluids* **26**, 871

Landahl, M.T. (1972). Wave mechanics of breakdown. *J. Fluid Mech.* **56**, 775

Landahl, M.T. (1975). Wave breakdown and turbulence. *SIAM J. Appl. Math.* **28**, 735

Landahl, M.T. (1980). A note on an algebraic instability of inviscid parallel shear flows. *J. Fluid Mech.* **98**, 243

Landahl, M.T. & Mollo-Christensen, E. (1986). Turbulence and random processes in fluid mechanics. *Cambridge University Press.*

Landau, L.D. (1944). On the problem of turbulence. *C.R Acad. Sci. U.R.S.S.* **44**, 387

Li, F. & Widnall, S.E. (1989). Wave patterns in plane Poiseuille flow created by concentrated disturbances. *J. Fluids Mech.*, **208**, 639

Meksyn, D. & Stuart, J.T. (1951). Stability of viscous motion between parallel planes for finite disturbances. *Proc. Roy. Soc.* A **208**, 517

Nishioka, M., Iida, S. & Ichikawa, Y. (1975). An experimental investigation of the

stability of plane Poiseuille flow. *J. Fluid Mech.* **72**, 731

Orr, W. M'F. (1907). The stability or instability of the motions of a perfect liquid and of a viscous liquid. *Proc. Roy. Irish Acad.* A **27**, 9

Orszag, S.A. (1971). Accurate solution of Orr-Sommerfeld stability equation. *J. Fluid Mech.* **50**, 689

Orszag, S.A. & Kells, L.C. (1978). Transition to turbulence in plane Poiseuille and plane Couette flow. *J. Fluid Mech.* **96**, 159

Orszag, S.A. & Patera, A.T. (1980). Subcritical transition to turbulence in plane channel flows *Phys. Rev. Lett.* **47**, 989

Orszag, S.A. & Patera, A.T. (1981). Subcritical transition to turbulence in planar shear flows. In *Transiton and Turbulence* (ed. R.E. Meyer), p 127. Academic

Orszag, S.A. & Patera, A.T. (1983). Secondary instabilities of wall bounded shear flows. *J. Fluid Mech.* **128**, 347

Rayleigh, Lord (1880). On the stability or instability of certain fluid motions. *Proc. London Math. Soc.* **11**, 57

Reynolds, O. (1883). An experimental investigation of the circumstances which determine whether the motion of water shall be direct or sinuous, and of the Law of resistance in parallel channel. *Phil. Trans. Roy. Soc.* **174**, 935

Rozhdestvenski, B.L. & Simakin, I.N. (1984). Secondary flows in a plane channel: their relationship and comparison with turbulent flows. *J. Fluid Mech.* **147**, 261

Schlichting, H. (1933). Zur Entstehung der Turbulenz bei der Plattenströmung. *Nachr. Ges. Wiss. Göttingen, Math.-phy. Kl.*, 181

Schubauer, G.B. & Skramsted, H.K., (1947). Laminar boundary layer oscillations and transition on a flat plate. *J. Res. Nat. Bur. Stand.* **38**, 251

Sommerfeld, A (1908). Ein Beitrag zur Hydrodynamischen Erklaerung der turbulenten Fluessigkeisbewegungen *Proceedings 4th International Congress of Mathematics*, Rome, vol. III, 116

Squire, H.B. (1933). On the stability of three-dimensional disturbances of viscous flow between parallel walls. *Proc. Roy. Soc.* A **142**, 621

Stuart, J.T. (1960) On the non-linear mechanics of wave disturbances in stable and unstable parallel flows. Part 1. The basic behaviour in plane Poiseuille flow. *J. Fluid Mech.*, **9**, 353

Tollmien, W. (1929). Über die Entstehung der Turbulenz. *Nachr. Ges. Wiss. Göttingen, Math.-phy. Kl.*, 21

Tollmien, W. (1935). Ein allgemeines Kriterium der Instabilität laminarer Geschwindigkeitsverteilungen. *Nachr. Ges. Wiss. Göttingen, Math.-phy. Kl.* **1**, 79

Widnall, S.E. (1984). Growth of turbulent spot in plane Poiseuille flow. In *Turbulence*

and Chaotic Phenomena in Fluids (ed. T. Tatsumi) p.93, Elsevier Science Publ.

Wygnanski, I., Sokolov, M., & Friedman, D. (1976). On a turbulent 'spot' in a laminar boundary layer. *J. Fluid Mech.*, **78**, 785

Wygnanski, I., Haritonidis, J.H., & Kaplan, R.E. (1977). On a Tollmien-Schlichting wave packet produced by a turbulent spot. *J. Fluid Mech.*, **92**, 505